Development of a fault detection and location protection scheme based on the application of smart meters.

Craig Mukasa (751778)

Supervisors: Prof. John Van Coller and Prof. Chandima Gomes

A dissertation submitted to the Faculty of Engineering and the Built Environment, University of Witwatersrand, Johannesburg, in fulfilment of the requirements for the degree of Master of Science in Engineering.

Johannesburg, October 2021

Declaration

I declare that this dissertation is my own unaided work. It is being submitted to the degree of Master of Science in Engineering to the University of the Witwatersrand, Johannesburg. It has not been submitted before for any degree or examination to any other University.

....

(Signature of Candidate)

…2nd…. day of …October… year …2021….

Abstract

Global weariness of rolling blackouts and increasing concerns for the climate has spurred the demand for reliable renewable energy. The result is the microgrid which is changing the landscape of electricity supply. Local power generation, storage and consumption has increased electricity reliability to the consumer. However, various protection issues associated with the dynamic behaviour of the microgrid arise. The objective of the proposed research is to formulate a fault location algorithm based on voltage measurements from smart meters in an AC microgrid. Fault detection and location are complex tasks because of the varying network operating conditions. The proposed approach seeks to reduce that complexity by formulating a voltage-based location algorithm. This approach makes use of the global adoption of smart meters by increasing their functionality to include fault location. The benefit of using smart meters is that they are an existing network unit that can provide dispersed voltage measurements in the network. Dynamic Time Warping (DTW) is used to provide a comparison between pre-fault and faulted voltage measurements to detect the presence of a fault and the subsequent location. The novel application of this algorithm in this field allows for a robust, low data-intensive and simple solution to fault location. The study is approached by performing a manual design of a microgrid. A comparison is performed on the impact of different modelling techniques on the accuracy of the fault location algorithm. A review of the different protection strategies in the literature is presented and a case for the proposed approach is made. The influencing dynamic behaviour of the microgrid as well as the available protection devices are also discussed. The proposed algorithm proved accurate in the detection, classification and location of various fault types with differing fault resistances. The comparison method of the (DTW) algorithm allowed for accuracy to be maintained regardless of changes in the operating conditions of the network. However, the algorithm proved more suitable for an unbalanced network as opposed to a balanced network due to the increased available measurements from the different phases. It was noted that although the impedance modelling technique applied will affect any voltage-based protection solution, the algorithm developed in this study is robust enough to maintain accuracy. Furthermore, it was found that high-resistance faults were not the most determining factor in the accuracy of the algorithm, but it was the quality of the input data as well as the amount of data. Too little and low accuracy voltage measurements led to the algorithm showing high inaccuracies for the fault location estimation. Recommendations are then made for the measurement accuracy required of the smart meters as well as the minimum number in a given network.

To my late father, thank you for teaching me to be as flexible as water whilst insisting I follow you and do engineering. You are dearly missed.

Acknowledgements

I would like to extend my deepest gratitude to my supervisors Professor J. Van Coller and Professor C. Gomes for their academic support and mentorship during the period of my studies. They have always been freely available to assist me with the most complex of tasks to the most mundane of ideas. A special thanks to Mr Mverecha, a long-time family friend, for his immense support in this endeavour. I would like to thank my parents, my mother and my late father, whose love and care are the reasons I can do so much. To my siblings, thank you for your companionship and support in all that I do. To my friends, thank you for your friendship and for inspiring me to be aspirational. Lastly, many thanks to the Lord above for providing me with the strength to run and not grow weary.

Contents

Chapter 1: Introduction

1.1 Background

The concept of electrical power systems has traditionally been characterised by a linear scheme with a central generating unit, a transmission network and distributed consumption. Initially this was not the case, as the first power plants supplied electricity only to customers in close proximity [1] due to limited supply voltage since DC grids were used. The ability to transfer electricity over longer distances came about with technological advancements such as AC grids and the economies of scale in increased electricity generation. Greater connectivity, supply security and lower costs were achieved with the interconnection of high voltage generation plants and massive transmission and distribution networks. The further advancement of technology and with the motivation of increasing energy efficiency, enhancing electricity security and utilising renewable energy generation, has led to the introduction of microgrids and a global demand of distributed generators (DGs) [2]. A microgrid can be defined as a small low/medium voltage power system consisting of distributed generation units and loads. It can operate independently, islanded-mode, or grid-connected with connection to the grid occurring through a point of common coupling.

The occurrence of faults in a distribution network is due to various reasons such as sudden operational changes, equipment failure, environmental events (eg. storms) and cyber-attacks [3]. Power flow in a traditional power network is unidirectional, flowing from the generation unit through the transmission network to the end consumer. Increasingly there has been an introduction of bi-directional power-flow. This is especially true in microgrids where the network has the capability to operate in islanded mode. Accordingly, it brings about the possibility of fault current direction being forward or backward. This greatly increases the complexity in fault detection as relay settings are no longer static [3]. Additionally, the presence of DGs alters the behaviour of the microgrid causing alterations in the fault current magnitude and duration [4]. These changes in conjunction with the fault location in the microgrid requires protection reorganization. Due to this increased complexity, LV distribution networks have not been receiving much research attention, with few exceptions [5], as most research was focused on MV distribution networks. Historically, LV distribution networks were monitored only at the substation using relays, RTUs and SCADA. Technological advancements have brought distribution automation and advanced communication systems such that additional monitoring within the distribution networks is now possible. With the increased complexity of faults, advanced techniques provide solutions for fast fault location.

1.1.1 Distributed Generation (DG)

In literature, various definitions and descriptions are provided. These definitions vary according to power ratings, purpose, location, technology and even regional government regulations [2]. In this report, DG is defined as an electric power source directly connected to the distribution network or on the customer side of the meter [2] . Costs associated with DGs continue to decrease whilst hardware reliability increases due to rapid technological advancements. This has resulted in the worldwide proliferation of different DG technologies, such as solar PV and wind turbines, in power systems. The type of DG technology adopted is normally location dependent to maximise power generation using local environmental conditions, such as solar solutions in areas with high levels of solar irradiance. The benefits of employing DGs in power systems are numerous hence the global drive for its development and usage. The benefits of DGs are discussed by Van Thong et al. [6] and include:

- Power quality – Network voltage profile and stability can be improved by the connection of DGs. Therefore, the system can withstand higher loading events hence increasing the power quality.
- Efficiency – With the use of local sources, the losses associated with large transmission and distribution systems are reduced thereby increasing the power supply efficiency.
- Clean energy – The environmental impact of energy generation has become a global concern considering global warming. DGs based on renewable sources, such as photovoltaic and wind turbines, contribute to the reduction of greenhouse gases.
- Implementation period – The installation and payback period of DGs is lower than conventional power plants.

However, the introduction of DGs in a power system presents certain drawbacks, as discussed by Van Thong et al. [6] and include:

- Power quality – DGs are connected to the network through power converters which can inject harmonics into the network.
- Voltage levels – While there are advantages to the network such as enhancing the voltage profile, the introduction of DGs can lead to voltage fluctuations, voltage dips and voltage unbalances. This is because of the lack of coordination between the installed DG and the power utility.
- Line Loading – Depending on the size, location, and number of DGs, installation may result in increasing the load on the network feeders thereby leading to exhausting the hosting capability.
- Fault current – Fault current not only comes from the main grid in a unidirectional way, but also from the DGs making fault detection more complex and thus the conventional hierarchical protection method might fail. Additionally, fault current levels change with a connected DG in a network. This complexity requires an active protection system that can adjust protection relay settings accordingly.

1.1.2 Microgrid Protection

Safe operation and protection of the electrical power system are to be always ensured. It is important that the protection system is sufficiently selective to maximize availability of power supply. In a conventional network, power flow is unidirectional. This is not the case in a microgrid, with the integration of DGs, as the fault response is drastically different from a conventional network. In a microgrid with a high penetration of Inverter Interfaced DGs (IIDGs) these differences are further complicated. The fault current from IIDGs is limited and does not contribute significantly to the network fault current. Therefore, conventional over-current (OC) relay settings may fail to detect faults; hence the conventional protection schemes become susceptible to failure [4]. As a microgrid can operate in grid-connected or islanded mode, coordination of protection relays is further complicated. This is a result of the absence of a strong voltage source when in islanded operation mode. The unique challenges presented by microgrid protection are as follows [3], [7], [8]:

- Bi-directional fault current flow.
- Large variation of fault current.
- High Impedance Faults (HIF).
- Multiple operation modes: grid-connected and islanded (grid isolated).
- Diverse network configurations: radial, looped and meshed.
- Shorter electrical distances due to smaller scale systems, in comparison to large transmission systems.
- Low inertia in microgrids implies fault impact will occur faster and more intensely, thus requiring rapid and robust detection/control.
- False tripping.

The variety of operating statuses of a microgrid affect the performance of traditional protection schemes. The limitations of these schemes are as follows [8]:

- Fixed/predefined tripping conditions that cannot correctly perform under varying operating conditions and network topologies.
- A reduced fault current increases the tripping time in traditional OC relaying

To address the major issue of varying operational conditions, a robust protection strategy is required.

1.2 Problem statement

- The methods practised at present for fault location with limited fault currents in LV systems do not produce accurate outcomes.
- The above deficiency in fault location of the present methods is more dominant in power systems with IIDGs.
- The methods newly proposed for fault location require excessively large training data which makes the methods not practically applicable.
- Many methods practised at present for fault detection cannot provide multiple information such as detection, classification, and location of faults.

1.3 Research Question

The research question in this study is:

- How effective is a method of detecting, classifying, and locating faults in a LV microgrid if it is based on voltage measurements from smart meters, especially with high penetration of IIDGs?

The proposed method is to be based on voltage measurements as this is an electrical quantity whose change can be indicative of the presence of a fault. Therefore, the modelling of the feeder cable becomes important. Manufacturer catalogues do not necessarily contain zero-sequence impedance as the positive sequence impedance is more important for LV network design. However, for fault analysis the zero-sequence impedance is of equal importance therefore a determination of its value is required. Subsequently, to investigate the robustness of the proposed method the following sub-questions arise:

- Can the accuracy of meters at present, as specified in SANS 62053-22:2018, be extended to readings outside the nominal voltage range and will this accuracy be adequate?
- What effect does an accurately modelled LV feeder have on the performance of a fault locating scheme as opposed to the present methods of modelling LV feeders?

1.4 Research Objectives

The research objectives are:

- To develop an algorithm that can detect, classify, and locate faults in a LV microgrid with high penetration of IIDGs by using voltage measurements from smart meters.
- To find the level of accuracy of a smart meter required to provide readings outside the nominal voltage range that is adequate for the algorithm.
- To find the effects of the accuracy of the modelled feeder on the performance of the algorithm.

The research objective is to formulate an algorithm that can detect faults with limited fault currents in LV microgrids with a high penetration of IIDGs. The proposed method is to be able to adapt to network operating conditions to maintain performance accuracy.

1.5 Motivation

The industry trend is seeing a widespread adoption of local power generation with PV etc. (see Section 2.1.1). The consequence is a change in the nature of the fault current which compromises the existing protection methods. It is proposed to utilize another industry trend, smart meters (see Section 2.5), to formulate an appropriate protection method. Smart meters provide a dispersed sensor network thereby allowing for innovative protection methods to be formulated.

Chapter 2: Literature Review

2.1 Distributed Networks, Distributed Generation and Microgrids

The following section provides a review of DGs, their technology and impact on the distribution network. A definition of microgrids and its associated infrastructure is also given. This includes planning, system components and management.

2.1.1 Overview of Distribution Networks and Distributed Generation

The conventional function of a distribution network is to transmit energy from the generation source to the consumer [9]. Hence the radial configuration was used in network design with unidirectional power flow and little redundancy. With increasing demand of clean renewable energy and the liberalization of the energy market [1, 2], advancements in technology have enabled the incorporation of DGs into the distribution networks. The definition of DG is previously discussed in Section 1.1.1. The wide variety of DG types include diesel generators to newer technologies such as PV and wind turbines however of pertinence in this study is PV.

2.1.2 Microgrids

A microgrid is defined as a cluster of small DGs, loads and storage systems which can act independent of the grid [10]. Microgrids can be categorized based on the nature of electrical supply as [11]:

- AC microgrids.
- DC microgrids.
- Hybrid microgrids.
- Networked microgrids.

As traditional power systems are based on AC power, at the advent of microgrids, AC microgrids were considered first. In this dissertation, the AC microgrid is the one considered.

The Point of Common Coupling (PCC), a three-phase AC bus, serves as the interface between the microgrid and the utility grid, as shown in Figure 2.1.

A microgrid can either be operated in a grid-connected operating mode or an islanded operating mode [12]. In grid-connected mode, the microgrid maintains its link to the grid through the PCC whereas in islanded operating mode, the microgrid electrically isolates itself from the grid. In this system, the power required from the utility grid is reduced by the DG sources connected to supply the local loads.

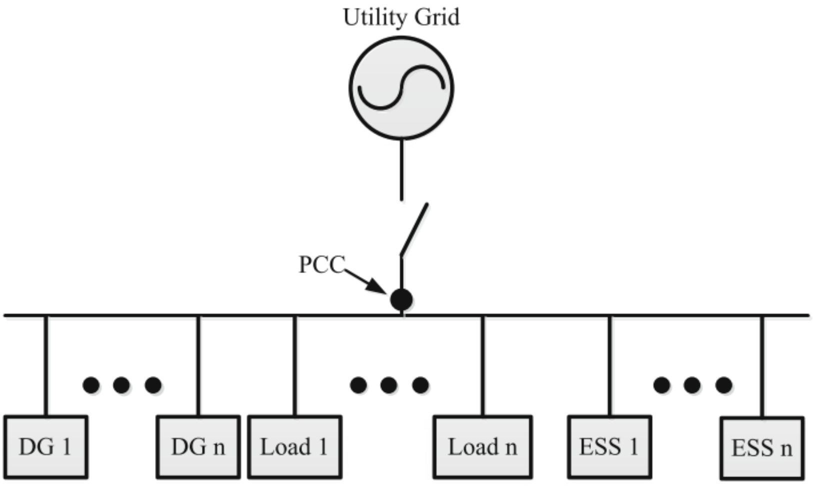

Figure 2.1: Microgrid with DGs [12].

2.1.2.1 Microgrid Architecture

As mentioned previously, the traditional power system has a radial layout where power flows unidirectionally from the point of generation to the point of consumption. The LV busbars, feed a number of LV feeders and consumers are connected along the feeders or the spurs [13]. In a microgrid with DGs, power flow becomes bidirectional between the consumers and the utility grid as shown in Figure 2.2. This raises the possibility of the network being radial or looped depending on the operation of the system components.

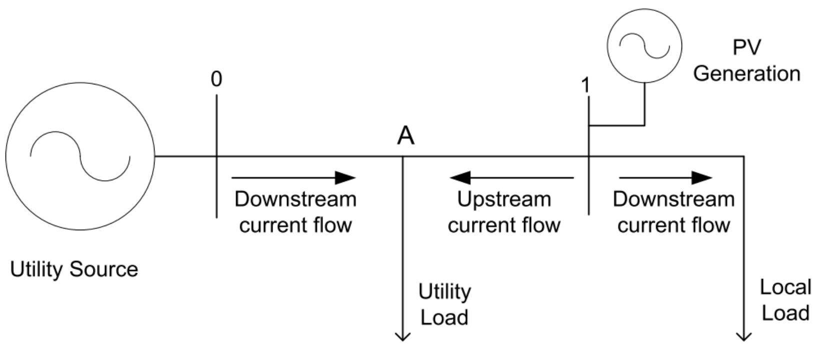

Figure 2.2: Power flow in a microgrid with DG [14].

LV networks are potentially unbalanced as they contain single-phase consumers and may also have three-phase consumers [13]. This results in possible single-phase feeder branches as well as three-phase feeder branches depending on the consumer type. Depending on the design, an LV network may contain overhead, underground or trunked cables and in some cases a combination [13], [15]. The feeder lines may also be composed of four conductors (three phases and the neutral) or three conductors (three phases without the neutral) [16]. This composition is determined by the earthing type of the system.

2.1.2.2 Modes of Operation

With the benefit of independent operation, a microgrid has multiple modes of operation depending on the situation as discussed by [11], [17], [18]:

1) Grid-connected Mode: This mode would be the normal operating mode of a microgrid with its interconnection to the utility grid. DGs augment the power flow from the utility grid to the local consumers. In certain countries, legislation has been put in place to allow excess power from DGs to be sold to the utility grid. This is done to encourage the adaption and production of clean energy.
2) Islanded Mode: In islanded mode, the microgrid disconnects from the utility grid. Therefore, the DGs become the sole source of power for the local loads. Scenarios leading to islanding are listed below.
   a) Planned Islanding: This process involves a notice of islanding from the utility, a balancing of load and generation at the PCC, adjustment of local controllers and protection devices, island creation and consequently a transition to steady-state island operation.
   b) Unplanned Islanding: This process involves the detection of a sudden need for islanding, adjustment of local controllers and protection devices island creation and consequently a transition to steady-state island operation.

The trigger for an unplanned islanding event is an internal or external fault [19]. In the event of an internal fault, the microgrid must disconnect itself from the main grid so fault current is not injected from the grid. In the event of an external fault, the microgrid should be able to detect the fault and disconnect itself so that the external fault does not disrupt the microgrid.

2.1.2.3 Earthing

An integral part of understanding the microgrid's operation is to understand the earthing scheme used in the design [13]. The various earthing schemes are defined in the national standard, SANS 10292, as follows [20], [21]:

- TT system (earthed neutral): At the supply source, the neutral is earthed and at the consumer all exposed conductive parts are connected to a separate earth electrode. This is the simplest and most common earthing system with the metallic water pipe network used to earth the consumer's installation. As time has progressed, migration to plastic water pipes has led to a switch to the TN system.
- TN system (exposed conductive parts connected to neutral): As with the TT system, the neutral is earthed at the supply source. The difference is that at the consumer, all exposed conductive parts are connected to the neutral conductor.
- TN-C system: In this system, the neutral conductor is also used as the earth conductor and is referred to as the Protective Earth and Neutral (PEN) conductor.
- TN-S system: At the supply source, both an earth conductor and the neutral conductor are connected to earth. The earth conductor is used to earth all exposed conductive parts at the consumer. This makes the system a five-wire system (three phase conductors, a neutral conductor and an earth conductor).
- TN-C-S system: At the supply source the neutral conductor is connected to earth. The consumer earth conductor is connected to the neutral conductor upstream of the consumer installation. It is a combination of the TN-C system and the TN-S system except that the TN-S system must be used downstream of the TN-C system.

The earthing system is important to know since it reveals the connectivity of the neutral conductor, the earth conductor, the cable sheath/armouring and the number of conductors used. In the event of a non-zero-sum current in the three phase conductors, the residual current flows in the protective conductor. As explained above, this is dependent on the earthing scheme used which provides the return path for the fault current. A network model needs to reflect this design choice to produce an accurate impedance model.

2.2 Microgrid Protection

The development of a protection system involves a number of factors including cost, material availability, protection philosophy and fault indicator availability [22]. The implementation of protection devices can be very costly and, in some cases, may be more expensive than equipment repair. It is important to implement a protection strategy with economic feasibility in mind. The cost directly impacts the availability of fault indicators as the most consistent relays/fault indicators tend to also be the most expensive. System faults do occur, but their infrequency must be considered when deciding to implement high-cost fault indicators. In most instances, an engineer must primarily cater for high impact, common and severe faults. There are multiple protection philosophies and the philosophy chosen in the design will guide the devices used, their placement and the subsequent system cost [23]. This is only tempered by material availability at the time of design implementation.

As mentioned in the introduction, the expectation of consumers on the utility to provide reliable electricity is high. Therefore, the protection of power system devices becomes increasingly important as not only is the power system device itself costly, but its failure could economically and socially impact the local consumer. In protection design, a primary protection and back-up protection are designed [22]. The intention is to ensure that power system devices are adequately protected in the event of failure of the primary protection. This could be a result of circuit breaker failure, fuse failure and pick-up failure [24]. Back up protection only activates in the event of primary protection failure and the system must be designed to ensure adequate coordination and avoidance of unnecessary tripping.

The guiding protection philosophy of protection of power system devices also applies in microgrids except it is more complicated due to the different characteristics. Microgrids are impacted by the introduction of DGs, independent operation and general flexibility. The unfamiliarity with these varying network conditions means a lot of research is being done on how to adequately cater for these differences as compared to conventional static networks.

2.2.1 Impact of DGs

With further additions of DGs, there are benefits and detriments as discussed earlier in the introduction. The leading benefits are consumers reducing their utility costs and the utility transmitting electricity with lower losses [25] through the distribution network as the demand is lower. DGs impact:

- Voltage Levels.
- Network fault current levels.
- Feeder Losses.
- Network congestion.
- Harmonics.
- Power factor.

2.2.1.1 Voltage Levels
The introduction of DGs along the feeder impacts the voltage levels along the feeder. This is a result of the local loads requiring less power than the local generating capacity. The excess power is then fed back to the grid but with a long feeder with multiple DGs, the voltage rise may become above acceptable values. National standard, SANS 1019 [26], specifies that the voltage supplied must be within 10% of the nominal voltage. In instances where the distribution system is a conventional radial network, the maximum voltage is found at the supply end of the feeder therefore regulation is done by the transformer at the substation. In the presence of dispersed power generators, voltage regulation must then also become dispersed along the feeder to mitigate overvoltages which now occur further down the feeder.

The feeder voltage profile is greatly influenced by both the presence and location of the DG. The feeder voltage profile rises with the installation of DG and is lower without installed DG.

In the absence of DGs and under normal operating condition, the voltage at the consumer's terminal is lower than at the supply end of the feeder. The impact of singular small-scale DG units on the feeder voltage is negligible but an aggregation of a number of units increases the total impact.

2.2.1.2 Network fault current levels
The presence of DGs in a network alters the nature of the fault current depending on the DG type. The fault contribution by DGs such as synchronous generators can increase the fault current by as much as ten times whereas the fault current from IIDGs is limited by the power electronic devices such that it is within twice the rated current of the inverter [25].

A reduction in fault current means that protective devices may be unable to detect the fault and fail to operate. This can further affect the coordination of the protection devices with unpredictable tripping or total failure to trip.

In the event of failure to trip of protection devices, fault current is fed back into the utility grid thus increasing the risk of failure of power system equipment. Further studies [27] indicate that unintentional islanding of the microgrid during an undetected fault will result in fault current circulating constantly within the microgrid.

2.2.2 Protection Devices

Over the years, protection devices for the conventional power system have developed such that they are extremely reliable in detecting faults. These devices protect electrical equipment from damage, prevent blackout, prevent environmental damage, and provide human safety, amongst others. The primary function of a protection system is to isolate the fault so its function must not be compromised during the fault [28]. The Circuit Breaker (CB) isolates the fault by disconnecting the fault from the rest of the network. The relay is the decision-making component of the power system. Based on the input received from the transducer, it decides whether a fault is present in the network. If a fault is present, the relay triggers the CB to trip - thereby isolating the fault.

2.2.2.1 Relays
The function of a protection relay is to logically initiate the opening and closing operations of a CB. Relays respond to a specified electrical quantity input hence it is not feasible to protect against all faults which may originate from different electrical quantities. Therefore, there

exists different relay types for responding to different electrical quantities such as over-voltage relays, overcurrent relays, frequency relays and reverse power relays [28]. Depending on the protection philosophy used, multiple relays are found in a network. Relays can be classified according to several different factors such as their function, input, operating principles, or performance characteristics. According to [29] relays can be classified according to their respective technologies:

- Electromechanical
- Static
- Numerical

The capability of each relay is determined by the limitations of the technology used. The most used relays are electromechanical and static relays which continue to provide reliable service after many years in use but numerical relays are the modern relays [29].

2.2.3 Protection issues

As discussed previously, transitioning from the conventional grid to a microgrid introduces challenges to the protection of the network. The basic requirements of a smart microgrid are the capabilities of plug-and-play operation and self-healing [30]. The presence of plug-and-play DGs changes the feeder fault current flow from unidirectional to bi-directional and alters the level of the fault current. The fault current level can be further altered depending on the microgrid operating mode, network topology and changing generation status of the DGs. These varying characteristics can be summarised as follows [11]:

- Bidirectional flow of fault current.
- Uncertain fault current and current flow direction.
- Large variation in fault current.
- Multiple operating modes namely grid-connected and islanded.
- Multiple network topologies: radial, looped and meshed.

The multiple and varying operational conditions in a microgrid mean that conventional static protection schemes are inadequate to provide protection. Relay types and coordination are seen to fail in systems with a high penetration of DGs [11], [24], [30]–[32]. A study performed [24] on the effectiveness of directional and differential relays in dealing with the bidirectional current flow showed how the variations of the operational conditions affected the conventional directional protection performance. The failings in conventional protection schemes can be summarised as follows [19], [33], [34]:

- Fixed tripping characteristics which cannot perform correctly under varying operational conditions.
- Reduced fault currents resulting in incorrect tripping of conventional relays and in certain instances failure to pick-up.
- Performance of conventional directional relays decreasing significantly for symmetrical faults at feeder spurs.
- Degree of performance varying according to fault type, with better performance shown for certain faults and a worse performance with other faults.

These varying network conditions thereby give rise to the following protection issues.

2.2.3.1 Loss of Sensitivity and Selectivity

The bidirectional flow of current, as shown in Figure 2.3, compromises relay operation as existing protection devices such as fuses, reclosers and non-directional overcurrent relays do not feature directional properties [22].

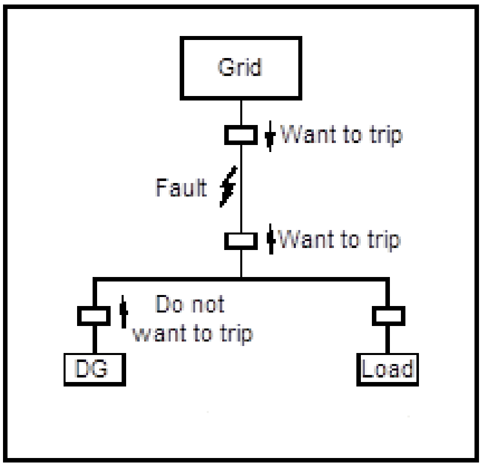

Figure 2.3: Bidirectional fault current

A reverse flow of current of high enough magnitude can trip a relay which would indicate a downstream fault when there is no downstream fault, thereby compromising the selectivity of the protection scheme. Furthermore, uncertain fault current magnitude can result in inadequate pickup current settings thereby hampering the sensitivity of the protection scheme.

2.2.3.2 False/Sympathetic Tripping

This occurs when fault current supplied by a DG feeds into an adjacent feeder. The relay in the adjacent feeder may trip and disconnect its loads unnecessarily [35]. This is shown in Figure 2.4. This problem can also be referred to as a selectivity issue.

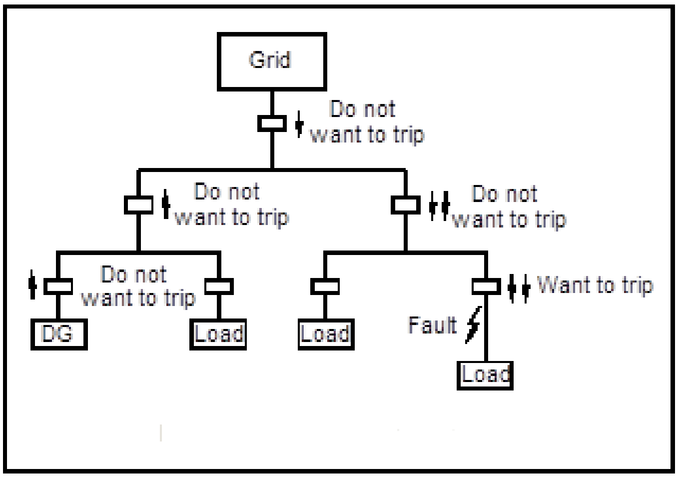

Figure 2.4: Possibility of false/sympathetic tripping

The relay closest to the fault, upstream, is the one designed to trip first. However, the alteration in fault current due to the presence of DGs results in sympathetic tripping of other relays in the network that are further from the fault point.

2.2.3.3 Protection Blinding

With the addition of DG into a network, the fault current is additionally supplied by the DG. Therefore, a fault current can fail to be picked up by the relay resulting in an underreach [36]. Alternatively, the fault current contribution can result in the relay overreaching.

2.2.3.4 Grid-connected and Islanded modes

As aforementioned, the typical operating mode of a microgrid is grid-connected with a connection to the utility grid and the alternative operating mode is islanded. In the grid-connected mode, the utility grid contributes to the fault current hence conventional protection devices operate as expected [21], whereas a transition to islanded mode alters the level of fault current in the microgrid with IIDGs producing low fault current. A potential solution to this is to introduce a flywheel to inject the high fault current in an islanded microgrid [18] but this raises costs and introduces safety concerns. A further concern is the earthing of the LV microgrid with multiple operating modes. The step and touch potentials are directly proportional to the magnitude of the fault current discharged by the earthing network. Consequently, the fault current distribution between neutral and earth is dependent on the earthing system and the operating mode of the microgrid [21]. As mentioned earlier, the earthing systems are broadly categorized as TT, TN, TN-C, TN-S and TN-C-S. The earthing system chosen must provide a safe path to earth for fault current and ensure the safety of individuals in proximity of the fault, and both must be ensured in both operating modes of microgrids. A study by [21] concluded that the TT or TN-C-S earthing systems were the most suitable for microgrids as DGs could be operated safely without earthing their neutral points in both operating modes.

2.2.3.5 Protection relay coordination

Protection relays are used to ensure the safe operation of the system and are required to have the following characteristics [28]:

- Reliability
- Sensitivity
- Selectivity
- Speed
- Stability

These are achieved by the creation of an efficient and coordinated protection system where faults are detected and isolated in the minimum possible time with as little of the network affected as possible [24]. This is possible in a conventional radial network with unidirectional power flow as fault current flow allows for straightforward coordination of relays. However, this is not the case with microgrids as the topology and characteristics are different, as mentioned previously, with varying current direction and magnitudes. The reliability of the network decreases with the subsequent miscoordination of protection devices such as fuse-fuse, recloser-fuse, breaker-breaker and relay-relay [24]. Even reliable methods such as conventional overcurrent (OC) protection are susceptible to false tripping, protection blinding and asynchronous operation [37]. Varying network characteristics require a proper coordination strategy that meets grid code compliance [30] and ensures safe operation.

2.2.4 Existing Protection Schemes

There are various conventional protection schemes that have been developed for radial distribution networks that cannot be applied to microgrids without modifications. Some of these methods are described below.

2.2.4.1 Time Overcurrent Protection

One of the earliest methods of protection developed was time overcurrent (OC) protection and remains one of the most widely used methods in distribution microgrids. The principle of operation is the relay operates when it detects a current above the set threshold. The pick-up current threshold is adjustable and the time in which it trips is also adjustable [38].

Time overcurrent protection schemes are generally not applicable to microgrids which have varying fault current levels, limited fault currents, multiple operating modes and bidirectional current flow [11].

2.2.4.2 Distance Protection

Distance protection operates by monitoring both the network voltage and current [38]. When the calculated ratio is less than a pre-set ratio, which is the fixed impedance of the network, the relay operates. Variations of this fundamental principle have been developed to improve accuracy and consistency.

2.2.4.3 Differential Protection

Differential protection has historically been proven reliable and popular. The fundamental operating principle of differential protection is that if no fault is present the sum of currents flowing into a protection zone equals the sum of currents flowing out of that protection zone. The protection scheme can accurately detect and isolate faults without disturbing the rest of the distribution network [39]. It remains popular for microgrids as the relays can function well regardless of varying microgrid characteristics.

2.2.5 Emerging Protection Schemes for Microgrids

The technological advances that have been made, along with higher computer processing power, variety in communication networks and technical developments, have led to more advanced protection schemes being possible. These new schemes have the potential of increasing interconnectivity and robustness of protection of the microgrid. The following details some of the new methods.

2.2.5.1 Adaptive Protection

The varying operating modes of microgrids makes formulating an adequate protection scheme challenging. A subsequent solution to this was adaptive protection. The most common adaptive technique is adjusting relay settings according to the microgrid operating mode, grid-connected or islanded [39]. This is a process that would normally be done by a protection engineer [11] but is automated so that relay settings are adjusted in response to a changing operating mode [40]–[42]. The principle of adapting to network conditions has led to a lot of research into various adaptive protection techniques.

Adaptive protection is made up of the adaptive protection device and the adaptive protection scheme controller. The general system structure is shown in Figure 2.5 below [43].

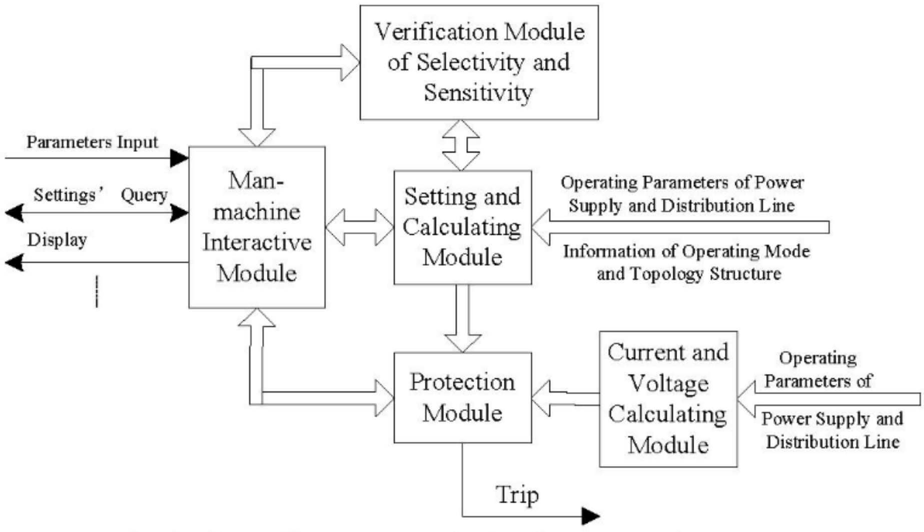

Figure 2.5: General system structure of an adaptive protection system for a power supply and distribution system [43].

The man-machine interactive module is the user interface. From this module, network parameters are set such as line length, unit impedance and other parameters. The relay settings are also displayed on this module. A separate verification module performs independent calculations to ensure the selectivity and sensitivity settings will trip the protection devices when a fault occurs. The varying nature of the network is catered for by the setting and calculating module. This module confirms the operating mode, topology structure, fault type and load of the network [43]. From here if any changes are detected, the relay settings are updated accordingly. The protection module is the decision-making component of the system, judging from the input parameters whether the tripping condition is satisfied or not.

With the general system structure, an adaptive protection system can be built with differing protection schemes and input parameters [44], [45].

2.2.5.2 Artificial intelligence techniques

With advances in computing power making complicated algorithms easily deployable in the field, an alternative solution to conventional protection is the use of Artificial Intelligence (AI). This is a knowledge-based method for fault detection with feeder parameters, cable length, grid topology and measurements required as input data. The data is then analysed with a trained AI technique to detect faults accurately, of which some techniques are described as:

- Artificial Neural Network (ANN) - ANN is a popular and reliable tool used in classification due to its accuracy in recognising complex patterns. This technique was adapted to power systems by researchers who further developed techniques that were optimized to the operating limitations in power systems. In the literature, various approaches are used [46] requiring one-end and two-end measurements to find fault distances. This approach with cascaded correlations concluded that both measurement approaches performed equally well, a smaller number of epochs were required and that a comparatively lower number of hidden layers were required relative to multilayer perceptron (MLP). A method to detect high impedance faults for non-linear arcing was suggested in [47] which used lower order voltage and current harmonics. Research done in [48]–[51] detailed other techniques to build a fault detection neural network. The advantage of ANN is that it is simple to implement and accurate. However, they require a large amount of quality data to train the algorithm. Therefore, if there are any limitations on the amount or quality of the data the performance of the algorithm will be affected. Furthermore, the convergence of the training process is slow and the ANN algorithm is required to be re-trained whenever there is a change in the network [52].

- Support Vector Machine (SVM) - SVMs are another popular and reliable tool used in classification and regression methods. The number of support vectors for a SVM is dependent on the algorithm used as opposed to ANN where the number of hidden layers is determined by trial and error [52]. Also, a SVM needs much fewer training data which makes it a more appealing tool than ANN. A method proposed by [53] used the faulted phase voltage and current fundamental components to calculate the fault location. Alternative methods in [54], [55] combined Radial Basis Function (RBF) neural network and SVM to identify the fault using the three-phase voltage. SVM proved to have a better operation as it had higher classifier rates even with less training vectors. For even large-size problems, SVMs have an advantage of operating faster and with less heuristics. However, the limitation lies in the selection of hyper parameters and kernel function to give the best performance.
- Fuzzy Logic - In fuzzy set theory, it is possibility that is discussed instead of probability where possibility is defined between one (completely possible) and zero (totally impossible) [52]. Whereas, given adequate statistical information a probability measure can be defined. In [56], the features of the fault waveform were extracted using higher order statistics. The classification of the fault was then done using fuzzy logic. Whereas in [57], the line currents of the three phases in a balanced network were used to develop a fault identification technique. This method was then further developed in [58] in order to also operate for an unbalanced network. The fuzzy logic handles uncertainties and produces rules based on the relationship between input and output. However, the disadvantage is in determining the global minimum and it requires an enhanced feature extraction and definition.

2.2.5.3 Genetic Algorithm

The Genetic Algorithm (GA) is an intelligent search and classification algorithm that can be used in fault location. It uses an iterative selection, crossover and mutation process until an end condition is reached. An approach taken in [59] used GA in a faulted section estimation as an optimization problem. Hebb's rule was used to identify the objective function and then the faulted section was identified using a Continuous Genetic Algorithm (CGA). With the objective function the time required for the CGA is reduced thereby using less storage and less time than binary GA. Another method [60] identifies the fault location using the terminal line parameters. Alternatively in [61], a combination of GA and wavelet transformation is used to s fault a three-phase network. This method performs feature extraction using discrete wavelet transformation on the three-phase current to produce inputs for the GA.

The GA can reduce the dimension size of the possible solution thereby increasing computation speed. However, as the GA process is random, results are inconsistent thereby making it not ideal for fault location.

2.2.5.4 Matching (Comparison) approach

The matching approach compares real time measured data with simulated data from a database for fault location, with voltage sag or current commonly measured. This is performed conscious of operating conditions to make the right comparison decision.

In [62], a database was created by simulating faults in different sections of a line and upon the occurrence of fault, the subsequent voltage sag was compared for its equivalent in the database. Hence the faulted section could be identified. However, the accuracy is limited to the section and requires on-site inspection for fault location. This method was improved on in [63] using voltage sag non-linear representation to formulate quadratic equations containing voltage-phase-and-distance and current-phase-and-distance. This was then used to calculate the fault location which proved more accurate for low-resistance faults. An alternative method [64] conducts multiple measurements on a line and uses a ranking procedure for identification of the faulted section. Fault distance can be accurately calculated by averaging the fault distance from each measurement node.

The matching approach is not data intensive as it only measures voltage sags at measurement nodes. However, the accuracy of the method is dependent on the database of simulated data for the matching process.

2.2.6 Dynamic Time Warping (DTW)

Dynamic time warping (DTW) is used to perform a similarity matching of two datasets by computing the minimum distance between vector points. DTW minimizes the distance between vectors of two datasets by aligning their structures [65]. This method of similarity matching calculates the deviation between two datasets and easily allows for the detection of an abnormality between two frames, indicative of a distortion. A deviation is classified as an abnormal spectral distance between a test data frame and an accepted reference data frame.

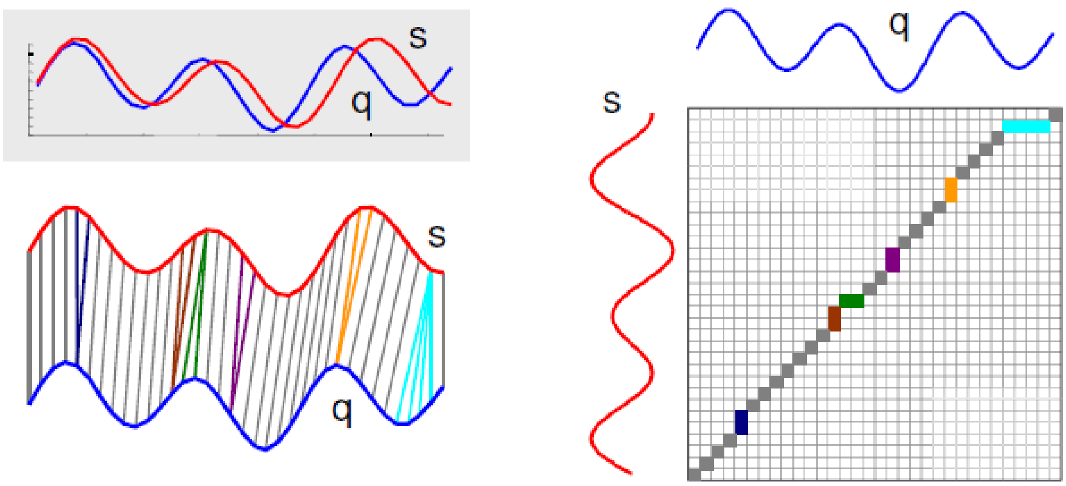

Figure 2.6: Illustration of DTW [65]

Figure 2.6 serves as a visualization of the implementation of DTW. Line curves q and s are similar in shape but are distorted in time with a lag between both curves. By performing a time-warping of the curves with retrieving the minimum distance between vector points as the operational goal, alignment of the curves is possible to give a measure of similarity. The points of large deviation in the diagram represent a distortion between the two curves. The advantage of employing this technique is its robustness and accuracy. In the performing DTW, the discrete data points or nodes of the data sets are traversed whilst seeking for the minimum transition cost:

$$d_T[(i_k, j_k) \mid (i_{k-1}, j_{k-1})] \overrightarrow{def} \; transition\ cost \tag{2.1}$$

Where $\overrightarrow{def}$ denotes the definition.

This is known as a type T cost which is the cost associated with a forward-going transition into any node from its predecessor in a path. A type N cost is the cost associated with traversing a node itself:

$$d_N(i, j) \overrightarrow{def} \; cost\ associated\ with\ node\ (i, j) \tag{2.2}$$

A type B cost is a combination of both the type T and type N costs. This is most frequently done by the addition of the transition and node costs at given node:

$$d_B[(i_k, j_k) \mid (i_{k-1}, j_{k-1})] \overrightarrow{def} \; d_T[(i_k, j_k) \mid (i_{k-1}, j_{k-1})] + \; d_N(i_k, j_k) \tag{1.3}$$

This relationship is reduced to denote a cost as being implicitly a type B cost for convenience as most often distance quantities are defined as type B:

$$d[(i_k, j_k) \mid (i_{k-1}, j_{k-1})] \overrightarrow{def} \; d_B[(i_k, j_k) \mid (i_{k-1}, j_{k-1})] \tag{2.4}$$

Hence the distance associated with a complete path is the sum of the costs of the transitions and/or nodes on the path, which is expressed as:

$$D = \sum_{k=1}^{K} d[(i_k, j_k) \mid (i_{k-1}, j_{k-1})] \tag{2.5}$$

In formulating an algorithm for the solution for the least cost or shortest path, the Bellman Optimality principle is used:

$$(s, t) \xrightarrow{(w,x)} (u, v) = (s, t) \underset{*}{\rightarrow} (w, x) \oplus (w, x) \underset{*}{\rightarrow} (u, v) \tag{2.6}$$

where $\oplus$ denotes the concatenation of the path segments.

This states that the path from (s, t) to (u, v) given the need to go through (w, x) is equal to the path from (s, t) to (w, x) plus (w, x) to (u, v). Therefore, the globally optimal path arriving at (i_k, j_k) is found by considering the best path segments arriving from predecessor nodes and choosing the path with minimum distance:

$$D_{min}(i_k, j_k) = \min_{(i_{k-1}, j_{k-1})} \{D_{min}(i_{k-1}, j_{k-1}) \; + \; d_B[(i_k, j_k) \mid (i_{k-1}, j_{k-1})]\} \tag{2.7}$$

To perform DTW, there are constraints to which the warping path must be adhered to:

1. Boundary Condition: P_1 = (1, 1) and P_L = (N, M).
2. Monotonicity Condition: n_1<n_2<n_3 .... < n_l and m_1<m_2<m_3 .... < m_l

3. Step-size Condition: P_l-P_{l-1} = {(1, 0) ;(0, 1) ;(1, 1)} for l = [1; L-1]

There are three types of global path constraints:

- Sakue-Chiba Band width: whereby the warping path is constrained to a defined region.
- Itakura Parallelogram: whereby the warping path is constrained to the region.
- Optimal Warping Path: whereby the warping path is not necessarily constrained to a region.

To develop a fast and efficient algorithm, the optimal warping path approach was taken. Optimal warping develops the most efficient path of moving through the data structure. In developing the algorithm, the conditions that were considered were the start, stop, boundary and iterating conditions.

Local path constraint:

$$D_{min}(i_k, j_k) = \min_{(i_{k-p}, j_{k-p})} \{D_{min}\left(i_{k-p}, j_{k-p}\right) + d\left[(i_k, j_k) \mid \left(i_{k-p}, j_{k-p}\right)\right]\} \quad (2.8)$$

where D_{min} is the minimum distance to the point $\left(i_{k-p}, j_{k-p}\right)$and d is the minimum distance from $\left(i_{k-p}, j_{k-p}\right)$ to (i_k, j_k).

There are various distance measuring techniques available such as the Euclidean distance, Manhattan distance, Cosine distance and Canberra distance [66]. However, a study by [67] showed that the Euclidean distance provided the most accurate results and hence is the preferred method in this research. The Euclidean distance is the minimum straight- line distance between two points in Euclidean space.

The cost associated with each iteration in the path is calculated by computing the Euclidean distance between the features extracted from the data of the template and test frames.

$$\text{Local distance} = dist\left((x, y), (a, b)\right) = \sqrt{(x-a)^2 + (y-b)^2} \quad (2.9)$$

The Euclidean distance is useful in that it always gives the real distance between points regardless of the vector point of the coordinate.

2.3 Faults

Faults can be defined as electrical disturbances that occur in a power system which require protection responses to maintain electrical infrastructure integrity. The normal flow of current is disrupted and the potential of damage to equipment can arise. This can occur because of various events such as insulation failure, broken conductor, environmental conditions (lightning or severe wind), human contact and even a tree branch touching a live conductor. There are also different fault types which can be classified in various ways such as level of the fault resistance and whether the fault is balanced or unbalanced. In this study faults are classified according to whether they are balanced or unbalanced and further expanded into the fault impedance level. The faults can vary from Low Impedance Faults (LIF) to Medium Impedance Faults (MIF) and to High Impedance Faults (HIF). Impedance of the fault determines the fault current level which is a very important distinction to make when designing a protection system. HIF show a very low fault current, close to load current, and are therefore much more difficult to detect. Whereas the LIF show a very high fault current and are easier to detect.

2.3.1 Balanced Faults

A balanced fault is a three-phase symmetrical fault in which all three phases are equally affected. The two types are a three-phase-to-ground (LLLG) fault and a three-phase fault not involving ground (LLL). This fault type is the most severe that can occur in a power system but is the most infrequent fault [20]. However, less severe fault types can cascade into this fault type. A three-phase fault occurs when all three phase conductors come into contact with each other as shown in Figure 2.7 below. A three-phase-to-ground fault occurs when the three phase conductors and the ground conductor come into contact with each other as shown in Figure 2.8 below.

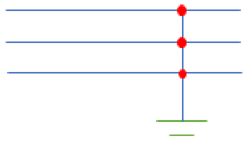

Figure 2.7: LLLG Fault

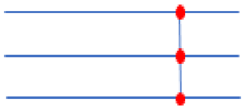

Figure 2.8: LLL Fault

2.3.2 Unbalanced Faults

The most common fault types are unbalanced faults. These are unsymmetrical faults whereby the phases are unequally affected. The three types are phase-to-ground (LG) faults, phase-to-phase (LL) faults and phase-to-phase-to-ground (LLG) faults. LG faults occur when the phase conductor comes into contact with the earth conductor. LL faults occur when two phase conductors come into contact with each other. LLG faults occur when two phase conductors and the earth conductor all come into contact with each other. The majority that occur are LG faults [20]; however these can escalate into more severe fault types if not attended to. These fault types are shown in the Figures 2.9 - 2.11 below.

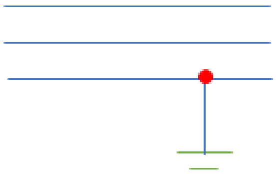

Figure 2.9: LG Fault

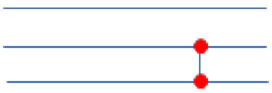

Figure 2.10: LL Fault

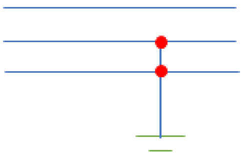

Figure 2.11: LLG Fault

2.3.3 Inverter behaviour under faults

The inverter behaviour for each fault type is considered because the ability of an inverter to handle fault current varies according to the manufacturer. Inverter behaviour under fault conditions can be considered as one of two scenarios: (1) where the fault is external to the DG/Inverter and (2) where the fault is internal to the DG/inverter.

In the case of (1), IEEE 1547-2018 [68] details the standardized operation of an inverter to external fault conditions. The requirements in this standard are for a Distributed Energy Resource (DER) unit which is interpreted as the combination of the generating unit and the interconnection equipment, which includes the inverter, converter and controller. The standard details the mandatory trip operation of DERs for abnormal voltage and frequency conditions, which is an update on previous standards which did not have trip specifications. The standard specifies the ride-through capability required of the DER. Ride-through is defined in the standard as the ability to withstand voltage or frequency disturbance inside defined limits and to continue operating as specified [68]. Of pertinence to this research is the voltage ride-through capability of DERs. Table 2.1 details the system response requirements to abnormal voltages, over-voltage (OV) and under-voltage (UV).

Table 2.1 IEEE Std. 1547-2018 Voltage trip requirements for Category 1[83]

Shall trip – Category I				
Shall trip function	Default settings		Ranges of allowable settings	
	Voltage (p.u. of nominal voltage)	Clearing time (s)	Voltage (p.u. of nominal voltage)	Clearing time (s)
OV2	1.20	0.16	Fixed at 1.20	Fixed at 0.16
OV1	1.10	2.0	1.10-1.20	1.0-13.0
UV1	0.70	2.0	0.0-0.88	2.0-13.0
UV2	0.45	0.16	0.0-0.50	0.16-2.0

The trip action is the cease to energize state [68] and is defined as the state where the DER shall not deliver active power during steady-state or transient conditions.

The standard provides abnormal performance categories which are based on the reliability needs of the power system network:

1. Category 1 – Based on minimal bulk power system reliability needs and is reasonably attainable by all DER technologies commonly available and in use.
2. Category II – Covers all bulk power system reliability needs and coordinates with existing reliability standards developed to avoid generator tripping during system disturbances.
3. Category III – Provides the highest disturbance ride-through capabilities intended to address integration issues in networks that have very high levels of DER penetration.

These are further elaborated upon in [68] but in this work, Category 1 requirements will be assumed.

In the case of (2), with an inverter internal fault there is no standard specification for the response of the DG/inverter. Therefore, the fault currents produced are not of standard values. The fault current is non-zero, varies by hardware design and is restricted using fault current-limiters [69]. Furthermore, the fault response of an inverter is dependent on the control strategy used in the design with strategies ranging from PQ controlled IIDGs to V/f controlled IIDGs [70]. The fault response is further affected by the chosen reference frame; Synchronous Reference Frame (SynRF) and Natural Reference Frame (NatRF) [71]. The studies show that there is a distinct change in the terminal voltage of the inverters during a fault whilst the inverter current does not increase significantly [72].

2.4 Voltage based protection

Many different protection methods were discussed in the preceding sections from impedance-based methods to knowledge-based methods. The main concern in fault detection and location is the varying fault current depending on the microgrid operating conditions and DG type [11] with inverters limiting current injection. Consequently, an alternative technique to detect faults would be to monitor terminal/nodal voltage. In fault analysis of microgrids [73] the results indicate the behaviour of voltage magnitude as a distinctive electrical quality that can be used in fault detection. It was shown that varying fault types can be detected and classified due to their unique impact on quantities such as phase angle, sequence components and harmonics among others. The following are a concise review of the voltage-based protection schemes proposed in literature.

- Voltage sag detection method based on the Park Transformation - studies done by [74]–[76] involved fault detection based on the Park transformation. A DC voltage signal is produced from an AC signal that has undergone the dq transformation. Subsequently, harmonics and high frequency transients can be filtered without altering the magnitude or phase of the system frequency component. Analysis needs to be done in the frequency domain as filtering a sinusoidal wave can introduce attenuation and a phase delay. Post-filtering, the voltage magnitude is calculated with an error being calculated after comparison with the reference voltage.
- Voltage sag detection method based on a 90-degree phase shift - studies done by [77], [78] involved a scheme whereby the addition of two squared waveforms with a 90° phase shift results in an equal value. The phase voltages are passed through a filter with a cut off frequency that results in a 90° phase addition to the waveform. This is then squared and added to the square of the original waveform. The resultant is a constant term that is compared with a reference voltage and the error used to detect the presence of a voltage dip or fault.
- High Impedance Fault (HIF) detection based on even voltage harmonics - a study by [79] presented a method of detecting high impedance faults by utilizing the even harmonics in the voltage measurements performed by smart meters. As smart meters are not designed to measure harmonics, the author proposed an added functionality to the metering capability to measure harmonics. It was then concluded that with no even harmonic generating load in the network, the even harmonic content detected by smart meters becomes non-zero during a HIF. Harmonics are normally injected into the network by non-linear loads and power electronic devices which are mostly odd harmonics. The proposed method was implemented in hardware and tested under HIF conditions, load/capacitor switching, voltage sags and feeder energization. The method detected HIF accurately even under varying operating conditions and was compared with existing methods; mathematical morphology-based HIF detection, wavelet-based HIF detection and harmonic based HIF detection. The author conceded that the proposed method's performance is limited by the measuring accuracy of the smart meter. However, the writer did not show the effect that DGs would have on the method

nor the minimum number of smart meters required in the network for the method to maintain accuracy.

- Superimposed Voltage-based protection - this method detects faults based on the voltage change at the terminals of the IIDGs [72]. In the presence of a fault there is an induced change in the voltage at the inverter terminals indicative of a fault. This method simplifies adjusting the protection threshold as compared to other voltage-based methods. However, it requires more processing time and is susceptible to capacitor switching which could lead to incorrect tripping.
- Fault detection based on RMS phase measurements and positive sequence components - in [5], comparison was made between using rms phase measurements or voltage positive sequence component measurements for fault detection and location. The study developed the scheme for a distributed network under the assumption that phase rms voltage measurements were available at each node and that the measurements were accurate. The fault locating process was separated into three steps; faulted branch identification, faulted sector localization and fault distance estimation, all of which were based on measurement of the rms voltage. The faulted branch was identified using the indicative voltage drop within a feeder of the presence of a fault. The faulted sector location was performed using the principle that along a faulted branch, the voltage will decrease linearly up to the fault sector after which it will stabilize. A graphical approach was used, with the slope of the voltage profile being utilized. The fault distance was estimated using the plot of the voltage profile and feeder length. This algorithm was tested using different load and DG scenarios as well as varying fault impedances. The results were then compared with the results from using the positive sequence component of the voltage as an alternative input to the algorithm. It was concluded in the study that phase rms voltage measurements have a higher detection rate of single-phase to ground faults than using voltage symmetrical components in the algorithm, fault distance estimation error increases as the fault resistance increases, a varying load and DG increases the susceptibility of the algorithm to misidentification and that the use of different conductor types in the network increased the fault distance estimation error.
- HIF localization based on novel application of smart meters - a study done by [80] examined two approaches for fault detection, namely one based on the rms current measurements at the beginning of the feeder and an alternative method based on the highest voltage drop along the faulted line. The detection method was combined with a fault location method based on the voltage rms measurements taken at the feeder nodes using installed smart meters. The current measurements were performed under the theoretical basis that at the occurrence of a fault there is a sudden increase in current. This is true for low fault resistances whereas for high fault resistances (>50 Ω) the fault current is similar in magnitude to the operating current which negates the ability of using rms current measurements for fault detection. The alternative fault detection method analysed was the voltage drop along the feeder using dispersed voltage sensors. EN50160 considers a voltage drop of 10% and greater of be an anomaly however the study concluded that based on this threshold, a voltage drop stemming from a fault can only be detected with certainty for low fault resistances (<1 Ω). Therefore, the study, having not concluded on an efficient fault detection method, assumed it having been successful and proceeded with fault location. Fault location was performed using nodal

voltage measurements and separated into three stages: faulted feeder identification, faulted sector localization and fault distance estimation. The study considered two categories of faults based on their location: at the beginning of the feeder and at the middle or towards the end of a branch. The study concluded that for the first case, results were more accurate for feeders that contained less loads or DGs. Therefore, for feeders with these elements, a greater number of voltage sensors are required to build an accurate voltage profile. It was also concluded that the accuracy of the method decreases as fault resistance increases. However, the study did not include the influence that measurement errors of the voltage sensor will have on the method.

2.5 Smart Metering

Metering is an important part of the distribution network as it measures the power consumption of the consumer for revenue collection. Metering technology has developed rapidly from mechanical meters that required personnel to take readings to interconnected smart meters. Smart meters measure power consumption and report back to the utility server. The advanced communication network allows for bi-directional communication whereby the consumer can even purchase electricity from the smart meters.

The proliferation of smart meters is increasing as they provide the consumer greater visibility of their power consumption and the prepaid element increases the cashflows of the utility [81]. Their increased usage allows the opportunity to utilize smart meters in protection strategies. smart meters can be considered as dispersed remote sensors in the network, thereby increasing their functionality beyond the conventional revenue metering. Such an approach will enable protection strategies to be implemented with minimal additional cost. The benefits of using smart meters in protection strategies can be summarized as follows:

- Greater observability on the network – multiple observation points allow for greater knowledge of the operating conditions of the network.
- Event detection – with classification of operating conditions of the network, useful event detection as well as fault location become possible.

With smart meters as a dispersed sensor network, the data available allows for innovative protection strategies to be formulated such as those outlined in Section 2.2.5. as well as the proposed method in this research, (described in Section 2.2.6 of this dissertation). For the smart meter to be useful in this application, the minimal functional specifications of the meters are that they are able to accurately measure voltages that have a large amplitude variation. The large variation is caused by the possible presence of faults and/or added DG. SANS 62053-22 [82], details the particular requirements for the electricity metering equipment (AC) for static meters. The percentage error limits for the smart meter are shown in Table 2.2.

The accuracy class 0.2 S and 0.5 S specifies the maximum error of ±0.2% and ±0.5% over the full load range of the meter. The standard also further details the limits of variation in percentage error permissible because of external influence quantities. These are detailed in Table 2.3.

Table 2.2: Percentage error limits (single-phase meters and polyphase meters with balanced loads) [102].

Value of current	**Power factor**	**Percentage error limits for meters of class**	
		0.2 S	**0.5 S**
0,01 I_n< I < 0,05 I_n	1	±0,4	±1,0
0,05 I_n< I < I_{max}	1	±0,2	±0,5
0,02 I_n< I < 0,1 I_n	0,5 inductive 0,8 capacitve	±0,5 ±0,5	±1,0 ±1,0
0,1 I_n< I < I_{max}	0,5 inductive 0,8 capacitve	±0,3 ±0,3	±0,6 ±0,6
When specifically requested by the user: from 0,1 I_n< I < I_{max}	0,25 inductive 0,5 capacitve	±0,5 ±0,5	±1,0 ±1,0

Table 2.3: Limits of variation in percentage error [102].

Voltage variation	**Value of current**	**Power factor**	**Limits of variation in percentage error for meters of class**	
			0.2 S	**0.5 S**
0,9 U_n< U < 1.1 U_n	0,05 I_n< I < I_{max} 0,1 I_n< I < I_{max}	1 0,5 Inductive	0,1 0,2	0,2 0,4
1,1 U_n< U < 1.15 U_n	0,05 I_n< I < I_{max} 0,1 I_n< I < I_{max}	1 0,5 Inductive	0,3 0,6	0,6 1,2
0,8 U_n< U < 0,9 U_n	0,05 I_n< I < I_{max} 0,1 I_n< I < I_{max}	1 0,5 Inductive	0,3 0,6	0,6 1,2

For voltages below 80% of the nominal voltage, the error of the meter may vary between +10% and -100%.

The voltage variation due to a fault can vary greatly; therefore, the variation in meter measuring accuracy will affect the fault detection and location algorithm. The impact of measuring accuracy on the performance of the fault location algorithm is investigated in this research. As shown in Figure 2.12, an installed smart meter measures the current and the phase-to-neutral voltage. From these values, the active and reactive powers can be computed.

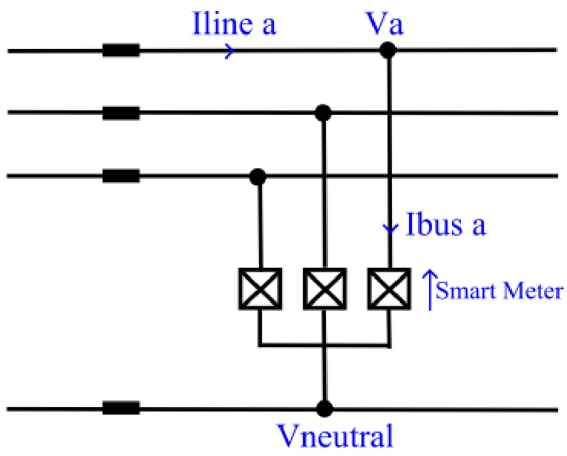

Figure 2.12: Smart Meter Measurement method [83]

Chapter 3: Methodology

3.1 Introduction

The methodology that will be followed is designed to formulate an accurate fault location algorithm.

It starts with a design of a suitable microgrid that can be used for testing the algorithm. The requirements of the cable model and the smart meter will be explored. The algorithm will be developed.

A high-level overview of the research methodology is shown below in Figure 3.1.

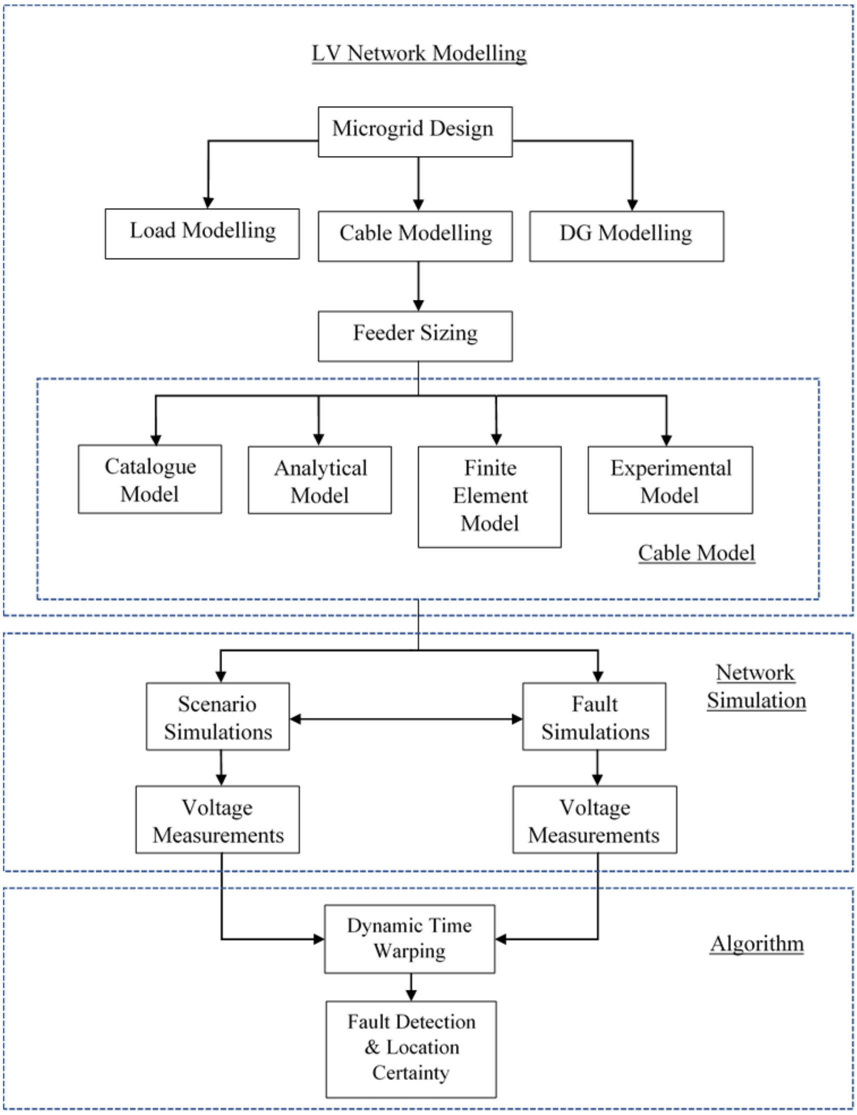

Figure 3.1: High level Overview of proposed research procedure.

The research methodology is further detailed below.

3.2 LV Network Modelling

3.2.1 Objective

In formulating fault location algorithms, most of the research done previously used existing microgrid models or models based on IEEE test feeders (Section 3.2.2.2). This allows for ease of data access hence enabling further research to be performed. However, access to existing microgrid data is severely limited due to concerns over infrastructure security and consumer privacy [84]. Furthermore, published IEEE test feeders and other representative networks vary widely in both scale and complexity.

The objective for the manual design of the microgrid is that it allows for greater attention to be paid to certain network characteristics. The proposed algorithm utilizes voltage measurement; therefore, the importance of accurate cable modelling becomes important. This method is possible due to the decreased network complexity when dealing with secondary distribution networks solely, as shown in Figure 3.2.

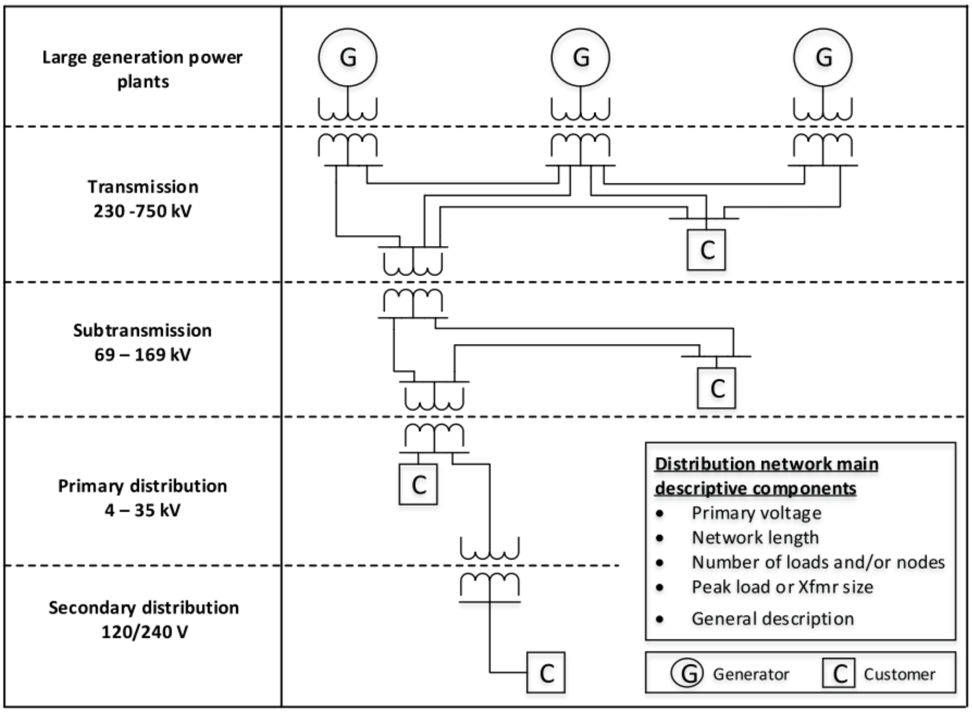

Figure 3.2: Power infrastructure grouped by voltage level [97]

3.2.2 Microgrid Design

3.2.2.1 Objective

The objective of the microgrid design is to establish the scope of the study by identifying research targets and permissible assumptions. Due to the reduced complexity of secondary distribution networks, manual design of a microgrid allows for the research objectives to be emphasised.

A microgrid consists of a point of local generation, local distribution and local consumption. This can be further extended with local storage and grid-connection capability. This section will discuss which parameters will be designed and which will be assumed.

3.2.2.2 LV Network Modelling

Test feeders that are representative of the characteristics of networks are used in this research for simulations. However, these vary widely in configuration, scale, and design. Distribution networks are considered critical infrastructure, hence detailed designs of real networks are often publicly unavailable [84]. Publicly available test feeders based on real networks are available from the Institute of Electrical and Electronics Engineers (IEEE) and the International Council on Large Electric Systems (CIGRE) but these are limited in number. Simulations of LV networks require an accurate model of the supply, load, and connectivity of the feeders. Therefore, different methods can be used to formulate a test feeder as illustrated in Figure 3.3 below.

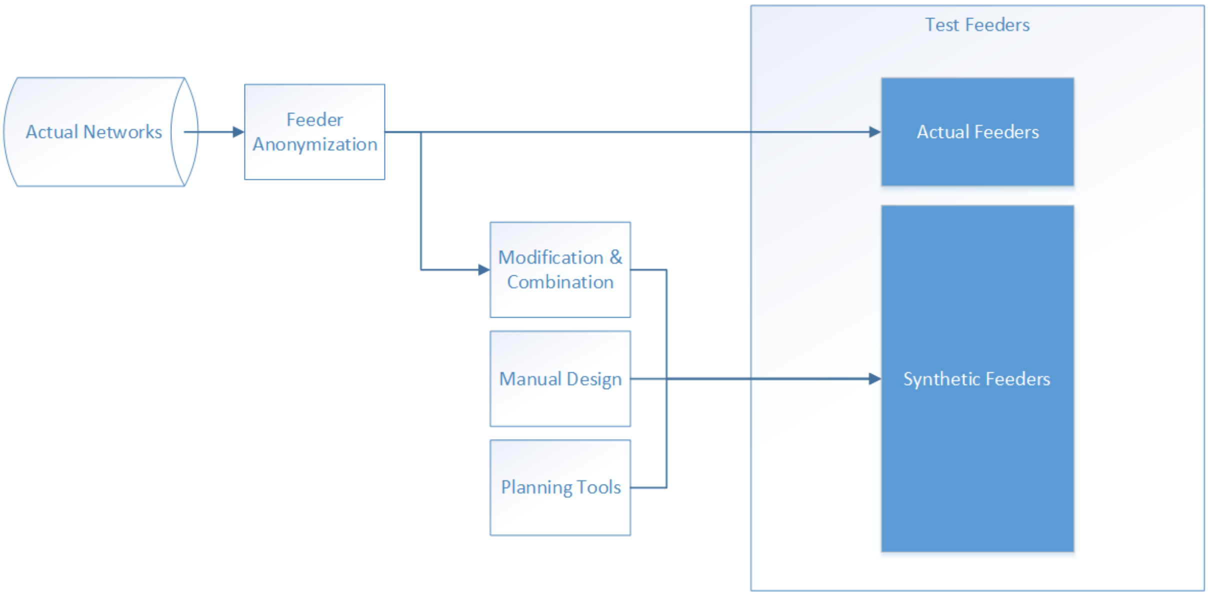

Figure 3.3: Test feeders building procedures

The simplest method is the use of an actual network's data to build the simulation test feeder. This is possible through the anonymization of user data to protect the consumer. This method can be further expounded upon by modification and combination of several anonymized networks to develop a synthetic test feeder that suits the research needs. Another method is the manual design of a feeder network. This can be very complicated and arduous hence it is most suitable for small networks of limited complexity. Depending on approach and data used, it may be important that experiments be conducted to validate results obtained. The final option is the use of planning tools from distribution planners that build test networks through technical and economic criteria [84]. Any of these procedures, and more, may be used to obtain the test feeder if the criterion of representativeness is achieved. The manual design approach is used in this research and is further detailed in the proceeding sections.

In many areas in South Africa, networks employ a radial topology. This is a topology where a main supply feeds successive voltage levels until the supply reaches the end consumer. This is illustrated in Figure 3.2. As most research on electrical networks has historically been conducted on HV and MV networks, publicly available LV test feeders are limited in number.

Examples include IEEE 342-Node Low Voltage Networked Test System (LVNTS) and CIGRE Benchmark Model for Low Voltage Distribution Feeders. Selection of a test feeder requires consideration of suitability and complexity. In this research the CIGRE Benchmark LV model is selected due to its reduced complexity and convertibility to suit research outcomes. The test network is shown in Figure 3.4 below. The simple radial network design allows for loads and DGs to be added or removed as well as allowing for additional feeders in a modified design.

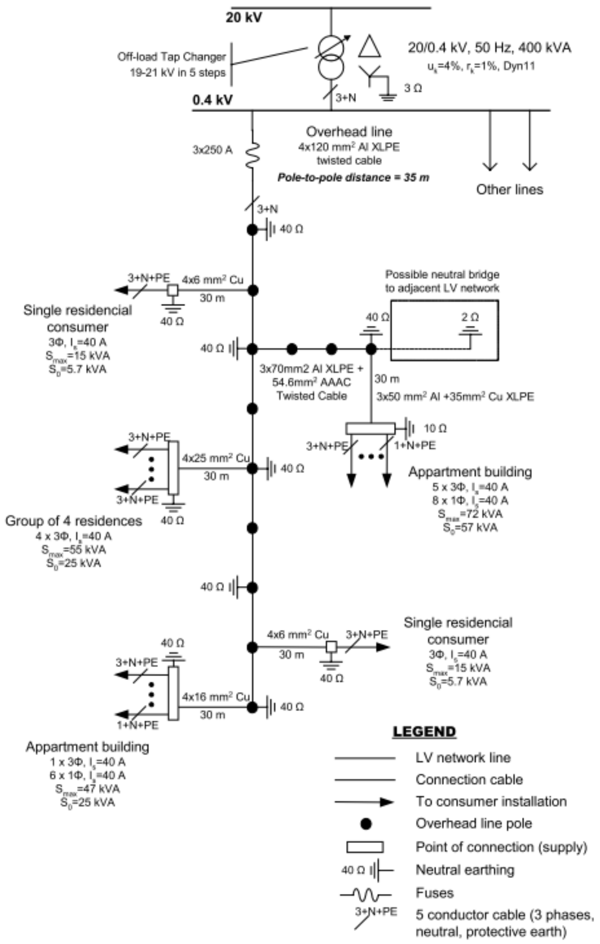

Figure 3.4: CIGRE Benchmark LV Model in "non-microgrid" form [13]

The model provided in [13] provides comprehensive network data and is suitable for both steady-state and transient simulation. However, as it is based on a European network it contains configurations that are not relevant for a South African network such as earthing, conductor type and transformer sizing. The earthing scheme is designed to be configurable between the TN and the TT type depending on the connection of the protective earth (PE) conductor of the consumer installation to the network neutral. In South Africa, the TN-C-S type is used, and the network model can be modified to account for this by specifying the cable type and the earthing scheme in the simulation software.

A microgrid form of the CIGRE Benchmark LV Model that includes various DG types is also available and is shown in Figure 3.5. The representative DG sources include photovoltaics, batteries, wind turbines, microturbines and fuel cells. However, no technical specifications beyond installation locations and sizes are included.

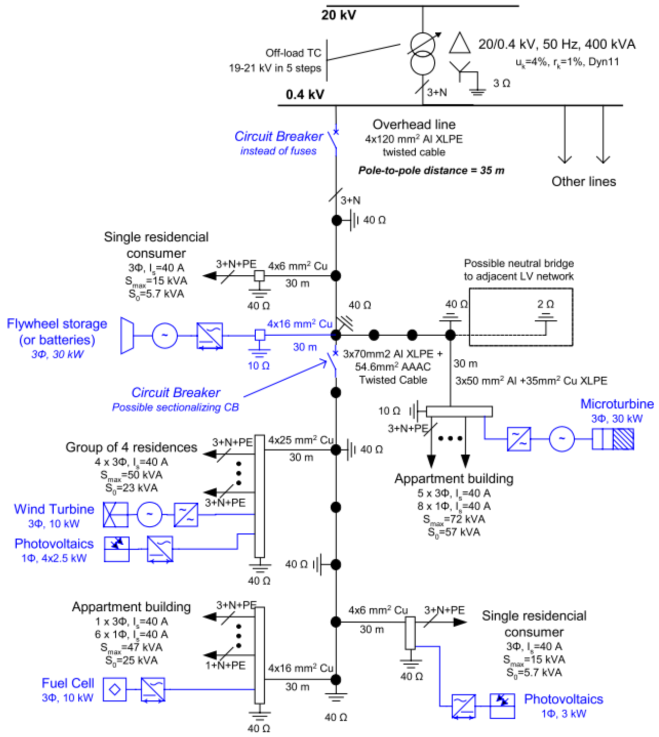

Figure 3.5: CIGRE Benchmark LV microgrid network [13]

Modifications can be made to this design to suit research objectives as in this research, PV is the DG of interest. Furthermore, the CIGRE Benchmark LV Model provides for the addition of more feeders for the development of a more complex network configuration.

3.2.2.3 Feeder Sizing

In AC installations the range of low voltage is up to 1000 V and for DC up to 1500 V. Designers must first determine the type of current and then the voltage level. A guiding factor in all these decisions, and subsequent ones, is compliance with national regulations.

To determine the power demand, a review of all items needing to be supplied with electricity should be done. The total current/power demand can be calculated using steady state demand, starting conditions, simultaneous operation demand and non-simultaneous operation demand. Another early consideration to make is the system earthing. System earthing is a protective measure used against electric shocks and is a determining factor in distribution topology. Figure 3.6 shows typical topologies for LV systems.

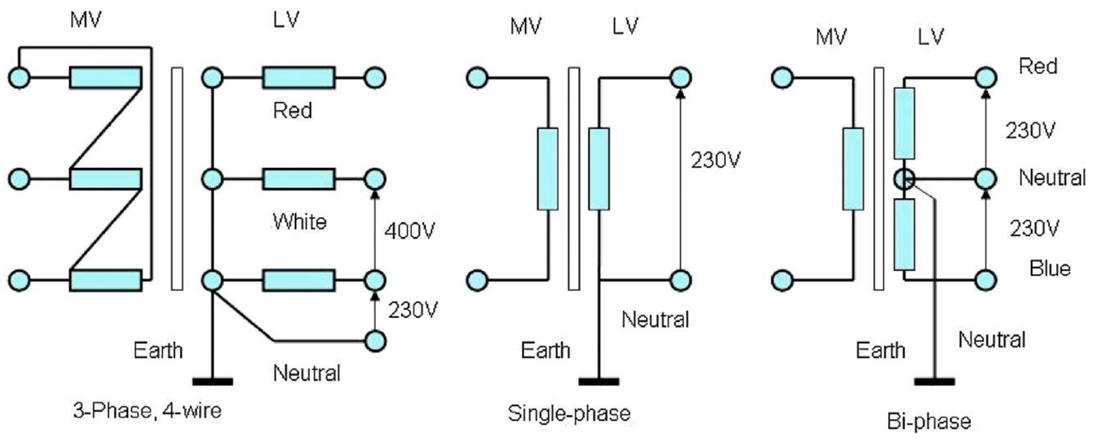

Figure 3.6: LV distribution topologies [85]

An important step in the design process is the selection and sizing of cross-sectional-areas of conductors. This can be approached in various methods but are generally categorised as either deterministic or probabilistic.

3.2.2.3.1 Deterministic

The sizing of conductors by calculating voltage drops using deterministic methods is perhaps the most common approach used in various studies and in industry. These rely on estimated averages and calculate according to worst-case scenarios. Furthermore, there are a number of design considerations that are required such as [20]:

- Maximum operating temperature - Current carrying capacities of cables are determined such that the maximum insulation temperature is not exceeded for prolonged periods.
- Correction factors - To account for service installation conditions, correction factors are used to correct calculated values.
- Ambient temperature - The current carrying capacities of cables in the air are based on an average air temperature equal to 30°C. However, for cables in the ground are based on an average air temperature equal to 20°C. Therefore, the appropriate correction factors must be applied accordingly.
- Soil thermal resistivity - The current carrying capacity of cables are based on ground resistivity equal to 2.5 K.m/W. It is documented that there is a relationship between soil nature and soil resistivity therefore the correction factor, related to the soil nature at the installation site, must be applied.
- Grouping of cables - When multiple cables are installed in the same group, a group reduction factor is introduced.
- Harmonic current - For a three-phase, four/five core cable, the current carrying capacity assumes that only three conductors are fully loaded. However, when harmonic currents are circulating, the neutral current can be significant - even greater than the phase currents. This is because the 3rd harmonic currents of the three phases do not cancel each other and sum up in the neutral conductor. This then affects the current carrying capacity of the cable and a correction factor is used.
- Voltage drop - As a result of the impedance of circuit conductors not being negligible, when carrying load current there is a voltage drop between the source and load terminals. Correct load operation is dependent on load terminal voltage values being close to its rated value. Therefore, circuit conductors must be sized to ensure load

terminal voltage is maintained within limits required for correct operation. This voltage drop limits refer to normal steady-state conditions and do not apply to motor starting and simultaneous switching of multiple loads. Limit values vary from country to country.

- Short-circuit current - Knowledge of the short circuit current at strategic points of an installation is necessary to rate switchgear (breaking capacity), cables (thermal withstand rating) and protective devices (selective trip settings).

The general aim is to determine the smallest allowable cross-sectional area for the conductors. The flow-chart in Figure 3.7 shows the steps taken to accomplish this.

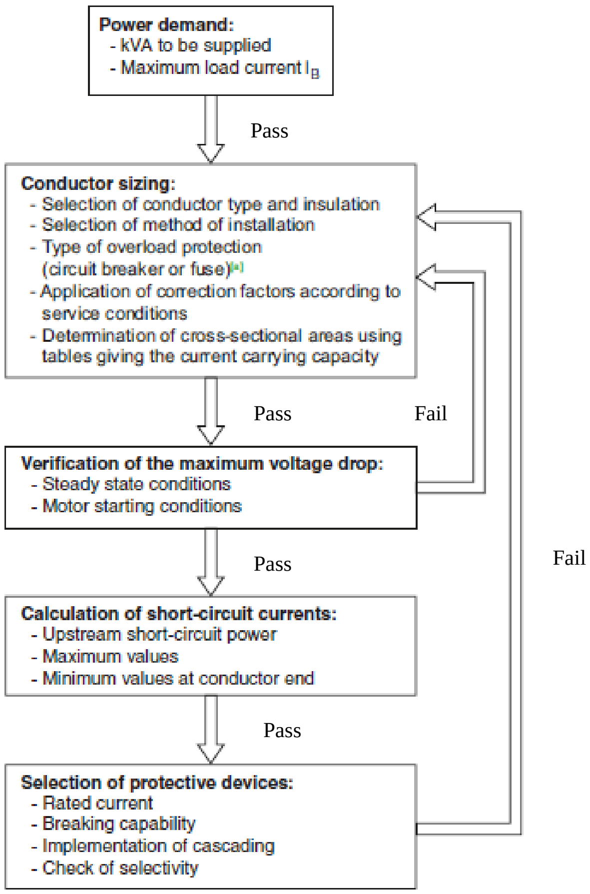

Figure 3.7: Flow-chart for conductor sizing [20].

Alternative methods include the Newton Raphson iterative method and the backward-forward sweep technique [86].

3.2.2.3.2 Probabilistic

Following a critique of LV distribution network design by Herman [87] the Herman-Beta method was formulated. This is a probabilistic method of calculating the voltage drop along a feeder using a beta distribution as a descriptor of the domestic load behaviour. Thereby predicting the voltage drop at the instant of maximum demand. This method is the recommended approach in SANS 507-1 [88] and, is further expanded on in Section 3.2.2.6.1.

Other methods include the Monte Carlo Simulation method and the method of Cumulants, but these are not considered in this research.

3.2.2.4 Cable Modelling

Models of the feeders are required to accurately model LV networks. This involves detailed analysis of network connectivity, feeder length, feeder type, conductor impedance as well as consideration of the grounding type to calculate the cable impedances. There are a number of modelling assumptions and their associated impacts [89] as follows:

- Network database of cables types, cable routes and cable connectivity – For HV and MV networks there is high confidence in the accuracy of network data whereas for LV networks there is uncertainty. This is evident in cases where service cables in LV networks are approximated as straight-line routes.
- Phase allocations for single-phase customers – Records of phase allocations for single-phase customers may be incorrectly entered or even missing. This results in the current balance between phases being incorrectly modelled.
- Neutral conductors, concentric neutral or sheath are grounded at each node – If ground connections are incorrectly modelled, inaccuracies in voltage calculations can be introduced.
- Neglect of shunt admittance – The shunt admittance for overhead cables is assumed to be negligible due to the minimal impact capacitance has on calculations for short lines.
- Simplified Carson's equations are valid for underground and overhead cable impedances. For the fundamental mains frequency, it was seen that impedance matrices obtained using the full Carson's equations and the simplified equations showed negligible differences.
- Impedances defined by positive and zero sequence impedance values – This approach results in any asymmetry, due to the cable, not being modelled as the coupling between sequence modes is neglected and cable balancing is approximated.
- Zero sequence impedance is estimated to be a multiple of the positive sequence impedance – A study found that with greater unbalanced currents, the zero-sequence impedance greatly affected the proportion of voltage range and unbalance constraint violations.

The above points summarise the assumptions that could affect the simulation. It is highlighted that in unbalanced systems, current flows in the neutral conductor; therefore, modelling of the neutral current return path will affect the accuracy of the network voltage simulations. On the basis that the neutral is grounded, the cable impedance matrix is commonly simplified to a 3×3 matrix. However, this is dependent on the grounding type used in the network. The grounding types are discussed in detail Section 2.1.2.3. The modelling of a multi-core cable is shown in Figure 3.8 with the associated self- and mutual impedances.

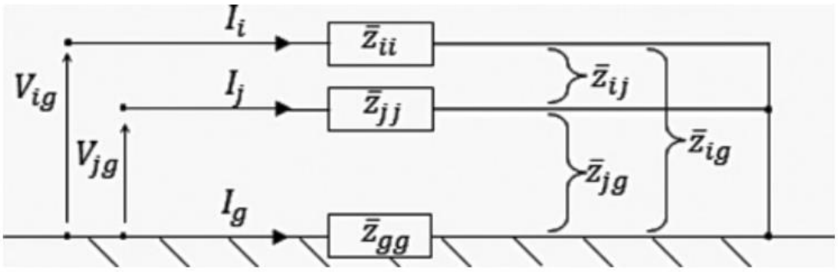

Figure 3.8: Conductor impedance model [90]

This equivalent circuit is short-circuited at one end to exclude the load and represent the voltage drops due to the cable impedances only. In a LV network, the cables include the three phase conductors, a neutral conductor and a conductive sheath as shown in Figure 3.9. A full impedance model comprises the series impedances, shunt admittances as well as the lumped impedances of the sheath connections to ground [89].

Figure 3.9: Aberdare LV Cable cross-section [91]

In a distribution feeder, careful consideration of conductor sizes, transposition and spacing between conductors is required to give an accurate model [92]. To develop a technique that could determine the self- and mutual impedances, Carson assumed the earth as an infinite, flat surface, uniform solid with a constant resistivity. Carson then made use of conductor images such that every conductor above ground had a mirror image conductor below ground. By this method, the ground currents could be modelled as images of the conductors in the cable and by making use of the fields between the conductors and their images, the impedance could be solved. Carson's equations are detailed extensively in [92] however by simplification, the modified Carson's equations are given in SI units as:

$$\widehat{z_{ii}} = r_i + \frac{u_0\omega}{8} + j\omega\frac{u_0}{2\pi}\cdot\ln\left(\frac{658.9}{D_{ii}\sqrt{\frac{f}{\rho}}}\right) \tag{3.1}$$

$$\widehat{z_{ij}} = \frac{u_0\omega}{8} + j\omega\frac{u_0}{2\pi}\cdot\ln\left(\frac{658.9}{D_{ij}\sqrt{\frac{f}{\rho}}}\right) \tag{3.2}$$

Therefore, the self- and mutual impedances of overhead and underground lines can be calculated and used to formulate the impedance matrix which, in the case of a 4-core cable with neutral, is a 4×4 matrix.

$$[\hat{Z}] = \begin{bmatrix} Z_{aa'} & Z_{ab} & Z_{ac} & Z_{an} \\ Z_{ba} & Z_{bb'} & Z_{bc} & Z_{bn} \\ Z_{ca} & Z_{cb} & Z_{cc'} & Z_{cn} \\ Z_{na} & Z_{nb} & Z_{nc} & Z_{nn'} \end{bmatrix} \tag{3.3}$$

In [92] the development of impedance models and the necessary approximations are discussed in detail.

3.2.2.4.1 Phase Impedance

Whether to include the ground path in the impedance matrix is dependent on the earthing method used. For a TN-C-S network, the neutral conductor is grounded via an earthing electrode or bonding to earthed metal hence the ground path is included in the impedance matrix. This concept is used to reduce matrix $\hat{Z}$ from a 4×4 matrix to a 3×3 matrix using Kron's reduction and assuming that the earth and neutral conductors are connected to each other at each end of the line (short-circuited) [92]. Applying this to matrix $\hat{Z}$ gives a 3×3 phase impedance matrix z_{abc} and the neutral current I_n with the notations from Equations (1) and (2):

$$z_{abc} = \widehat{z_{ij}} - \widehat{z_{in}}\widehat{z_{nn}}^{-1}\widehat{z_{nj}} \tag{3.4}$$

$$I_n = -\widehat{z_{nn}}^{-1}\widehat{z_{nj}}I_{abc} \tag{3.5}$$

Where $\widehat{z_{ij}}$ is the sub-matrix that contains the self- and mutual impedances of matrix $\hat{Z}$, $\widehat{z_{in}}$ is the sub-matrix that contains the mutual impedances between the phase conductors and the neutral conductor and $\widehat{z_{nn}}$ is the self-impedance of the neutral. However, Kron's reduction must be handled with care in instances where the neutral is ungrounded as this will lead to erroneous values.

3.2.2.4.2 Sequence Impedance

An alternative approach is to use the sequence impedance values to characterise the cable. These can be obtained from the manufacturers datasheet which often provides the positive sequence impedance value but not the zero-sequence impedance value. The given values define the conductor alone and not the earth return. Mutual coupling is assumed to be zero as this information is not normally available and as no earth current is normally defined, it is often assumed that the circuits are isolated from ground [89]. The negative sequence impedance is of the same value as the positive sequence impedance, hence the sequence impedance matrix, z_{012}, can be formed using these as well as the zero-sequence impedance.

From the matrix, z_{012}, the phase impedance matrix, z_{abc}, can be formed through transformation. However, if z_{012} represents a cable with an earth path, as there is no further information to expand z_{abc} to a 4×4 matrix, it is implied that there is no potential difference between neutral and ground.

$$z_{abc} = \begin{bmatrix} z_{aa} & z_{ab} & z_{ac} \\ z_{ba} & z_{bb} & z_{bc} \\ z_{ca} & z_{cb} & z_{cc} \end{bmatrix} = \begin{bmatrix} z_s & z_m & z_m \\ z_m & z_s & z_m \\ z_m & z_m & z_s \end{bmatrix} \tag{3.6}$$

where z_s is the self-impedance of the phase conductor and z_m is the mutual impedance of the phase conductors.

An alternative method of calculating the sequence impedance is to transform the phase impedances as outlined in [92]. For this, the following assumptions are made:

- The self-impedances of each conductor are equal: $z_{aa} = z_{bb} = z_{cc} = z_s$.
- The mutual impedances between the conductors are equal: $z_{ab} = z_{ba} = z_{ac} = z_{ca} = z_{bc} = z_{cb} = z_m$.
- The mutual impedance between the phase conductors and neutral conductor are equal: $z_{an} = z_{bn} = z_{cn}$.

$$z_{012} = {A_s}^{-1} \cdot z_{abc} \cdot A_s \tag{3.7}$$

$$A_s = \begin{bmatrix} 1 & 1 & 1 \\ 1 & {a_s}^2 & a_s \\ 1 & a_s & {a_s}^2 \end{bmatrix} \tag{3.8}$$

With $a_s = e^{j2\pi/3}$ this results in the following sequence impedance matrix:

$$z_{012} = \begin{bmatrix} z_{00} & z_{01} & z_{02} \\ z_{10} & z_{11} & z_{12} \\ z_{20} & z_{21} & z_{22} \end{bmatrix} = \begin{bmatrix} z_{00} & 0 & 0 \\ 0 & z_{11} & 0 \\ 0 & 0 & z_{22} \end{bmatrix} \tag{3.9}$$

$$z_{11} = z_{22} = z_s - z_m \tag{3.10}$$

$$z_{00} = z_s + 2\, z_m \tag{3.11}$$

3.2.2.4.3 Analytical corrections for AC resistance according to SANS 60287

The methods for calculating the AC resistance and the current ratings of cables are detailed in SANS 60287 [93]. Although primarily catering for circular conductors, the standard provides compensation factors for sector shapes. The total AC resistance is defined as:

$$r_{i,total} = r_{i,DC}(1 + \gamma_s + \gamma_p)(1 + \lambda_1) \tag{3.12}$$

where:

$$skin\ effect, \gamma_s = \frac{x_s^4}{192 + 0.8 x_s^4} \tag{3.13}$$

$$proximity\ effect, \gamma_p = \frac{x_p^4}{192 + 0.8 x_p^4} \left(\frac{d_c}{s}\right)^s \times 2.9 \tag{3.14}$$

$$x_s^2 = \frac{8\pi f}{R'} 10^{-7} k_s \tag{3.15}$$

$$x_p^2 = \frac{8\pi f}{R'} 10^{-7} k_p \tag{3.16}$$

$$r_{i,total} - total\ AC\ resistance$$

$$r_{i,DC} - DC\ resistance$$

$$f - supply\ frequency\ in\ hertz$$

$$d_c - the\ diameter\ of\ the\ conductor\ (mm)$$

$$s - the\ distance\ between\ conductor\ axes\ (mm)$$

$$k_s, k_p - compensation\ factors$$

The parameter, λ_1, accounts for resistive losses arising from the induced eddy currents in the sheath. Work done by [90] found that the corrections make minor differences at 50 Hz and with smaller cables. However, for conductors with large dimensions a more notable difference was found with the sheath losses making the largest contributions.

3.2.2.5 Network design

As previously mentioned, the CIGRE Benchmark LV Model is used as the basis for initial design of the microgrid. The following will detail the modifications made to meet research objectives and to contextualize the grid to South Africa.

Consumers can be divided into separate classes based on their annual consumption, gross income and measure of standard of living. SANS 507-1 [88] provides guidelines for this classification by providing typical design load parameters for domestic consumers in broad categories. The urban multi-storey/estate consumer has the highest standard of living and gross income range. This consumer class would presumably be able to afford the required smart meter installations and this approach provides a basis for the work. The relevant load parameter for this consumption class is the After Diversity Maximum Demand (ADMD) for a 15-year projection. The ADMD is 5.3 kVA.

With the assumption that the residential area fed by the substation has only urban multi-storey/estate consumers, the total power to be fed from the substation to four feeders can be calculated. For a 250 m long feeder where each node is separated by 25 m, the number of nodes is calculated as 10. An assumption is made that there are four feeders each containing nodes. From each node, one consumer is fed as illustrated in Figure 3.10.

This means there are a total of 10 consumers per feeder resulting in a total of 40 consumers.

The total load for each feeder is calculated as:

$Load_{feeder} = 10 \times 5.3\ kVA = 53\ kVA$

Therefore, the total load from the four feeders is:

$Load_{total} = 53\ kVA\ \times 4 = 212\ kVA$

The nominal voltage is 230 V, consequently the load current through each feeder is calculated using the minimum permissible voltage of 218.5 V:

$I_{feeder\ load} = \frac{S}{\sqrt{3}\times V} = 140$ A

To satisfy the minimum cable thermal rating, a 95 mm² cable is selected. This cable has a resistance per unit length of 0,427 mV/A/m. The voltage drop using this cable is calculated as follows:

$\Delta V = (\mathrm{R} \times l) \times I_{feeder\ load} = 14.95$ V

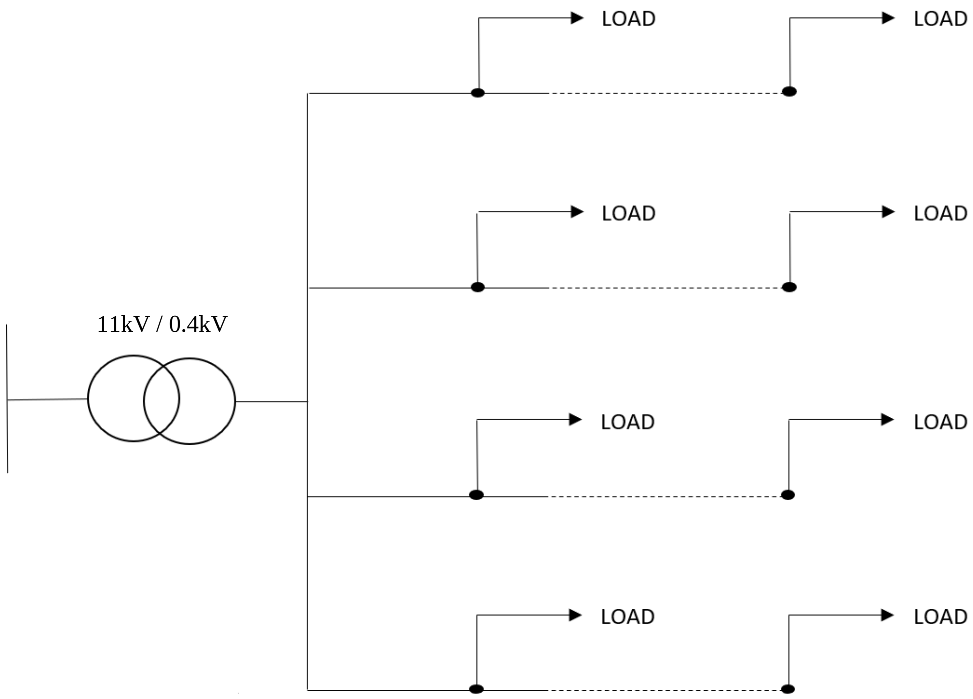

Figure 3.10: SLD of proposed microgrid

This voltage-drop as a percentage of the voltage at the bus bar of 230 V, is 4.50%, which is below the maximum permissible voltage drop of 5%. Therefore, the 95 mm² is adequate for this application.

3.2.2.6 Load Modelling

The greatest source of uncertainty in LV network design is in load modelling [88] as characterising, modelling, and analysis of a network depends on the load. The load is the power demand presented to the network by the consumer. Depending on the consumer habits, the power demand is constantly changing. To simplify and describe the varying load, certain terms have been formulated [92]:

- Demand – The load averaged over a specific period.
- Maximum demand – The largest demand value that occurs over a specific period.
- Average demand – The average of the demands over a specified period.
- Diversified demand – The sum of demands of a group of loads over a specific period.
- Maximum diversified demand – Maximum of the sum of the demands imposed by a group of loads over a specific period.
- Diversity factor (DF) – The ratio of the maximum noncoincident demand to the maximum diversified demand.
- Load diversity – The difference between the maximum noncoincident demand to the maximum diversified demand.
- After Diversity Maximum Demand (ADMD) – The simultaneous maximum demand of a group of loads divided by the number of loads.
- Load Factor (LF) – The ratio of the average demand to the maximum demand.
- Utilization factor – The ratio of the maximum demand to the rated capacity.

Having described the load with the assistance of the above terms, a load can be modelled as balanced or unbalanced, three-phase, two-phase or single phase as the following:

- Constant PQ.
- Constant current.
- Constant impedance.
- Any combination of the above.

Furthermore, deterministic or probabilistic design methods can be utilized depending on the intended outcome.

3.2.2.6.1 Herman-Beta Method

SANS 507-1/NRS 034-1 provides guidelines on the methodology of network voltage drop calculation through probabilistic load modelling. A probabilistic design method is recommended in South Africa as the best way to handle load uncertainty [88]. Research into South African domestic electrical loads validated the assumption that these can be modelled as constant current sinks which would result in their values being referred to in Amperes as opposed to kilowatts or kilovolt-amperes.

A deterministic design approach performs network design based on the worst-case scenario to ensure system operability. However, the standard recommends a probabilistic design approach for a more accurate network description. The loads can be described using a statistical expression known as a Beta Probability Density Function (PDF). The recommended approach is to use the Herman-Beta (HB) algorithm which is a probabilistic voltage drop calculation method that transforms beta distributed currents to beta distributed voltages. This is done using the load ADMD, the limiting circuit breaker rating and the beta distribution curve parameters, α and β. It is applicable for three-phase, bi-phase and single phase systems under the following assumptions [94]:

- For a group of loads, the maximum voltage drop is coincident with the maximum demand.
- The largest loads generally contain a large resistive component resulting in load power factor close to unity therefore the loads are considered as currents at unity power factor.
- The Beta PDF can be used to statistically describe the load at any given interval.
- The LV feeder impedance is considered to be purely resistive at a specific temperature.

The general procedure for the application of the HB method is outlined in [94] as follows:

- Network topology set up including load beta distribution.
- Calculate the maximum and minimum possible consumer voltages.
- Consequently, calculate the statistical moments of the consumer voltage, $E(V_c)$ and $E(V_c^2)$.
- Calculate the probabilistic parameters, α_v and β_v, of the consumer voltage.
- The consumer voltage at the end of the feeder is the quantile value calculated according to the chosen risk.

This is an accurate probabilistic approach for different network topologies and load types. Table 3.1 shows the recommended HB parameters and ADMD values for the differing consumer class from [88]. These can be used as a guideline for load and feeder modelling using the HB method. However, the standard cautions that the values indicated are typical for inland South Africa. For coastal areas, where the climate is different during winter, the ADMD values can be 12% higher or lower. The Geo-based Land Forecast Guideline compiled by Eskom states that geo-based load aggregation is more accurate than using diversity however that method takes long to populate the data [95]. The Guideline for Human Settlement Planning [96] as well as [88] provide a framework for defining households according to electrical consumption class.

Table 3.1: SANS 507-1/NRS 034-1 Herman-Beta parameters for various consumer classes for a 15 year forecast [88]

Consumer Class	Living Standard Measure	α	β	c [A]	ADMD [kVA]
Rural settlement	LSM 1	0.35	2.88	20	0.50
Rural village	LSM 1&2	0.48	2.13	20	0.84
Informal settlement	LSM 3&4	0.91	8.80	60	1.30
Township area	LSM 5&6	1.22	5.86	60	2.37
Urban residential I	LSM 7	1.25	3.55	60	3.59
Urban residential II	LSM 7&8	1.42	4.10	80	4.72
Urban township complex	LSM 8	1.42	4.13	80	4.70
Urban multi-storey estate	LSM 8	1.37	3.39	80	5.30

As shown in Table 3.1, the higher the consumer class the greater their electrical consumption and as such, in this research the load is modelled for the Urban multi-storey estate consumer class.

3.2.2.6.2 Load Profile

The load demand profile depicts the electricity usage of a consumer over a specific period, this gives an indication of consumer behavioural patterns. The load profile shape depends on the nature of the consumer. Standard load profiles are available that are based on the aggregation of numerous consumers to eliminate individual load stochastic variation [89]. However, the application of a statistical distribution can generate individual consumer demand. Figure 3.11 shows the typical load profile for a residential consumer obtained from [97], which is the focus of the research.

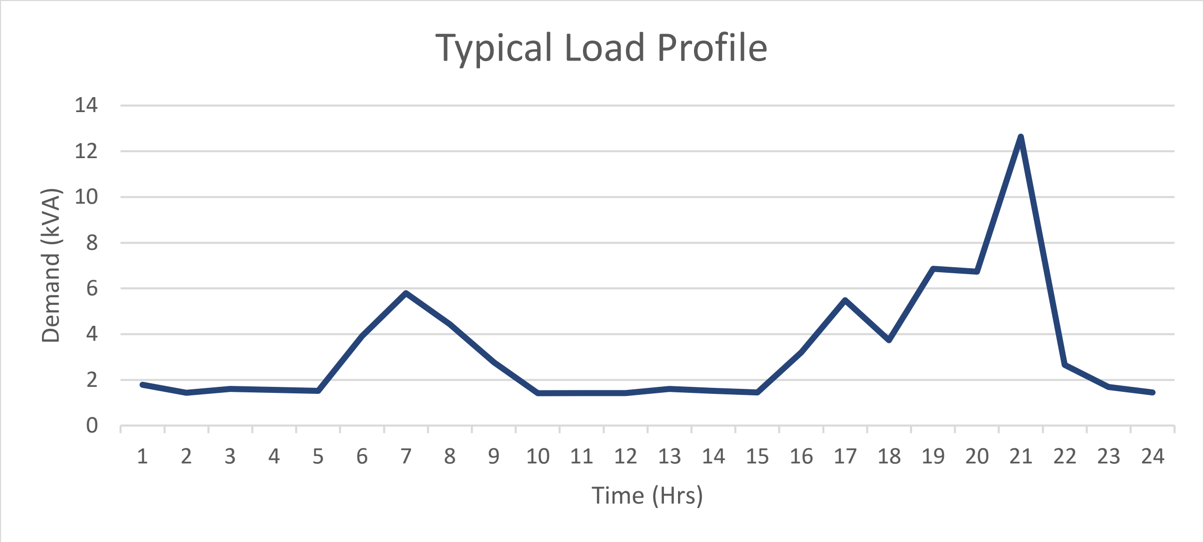

Figure 3.11: Typical Residential Load Demand Profile

The consumer load profile can be generated from a few methods which include direct measurement and appliance modelling.

Direct measurement is a process whereby measuring instruments are used to record the load demand of a consumer. This is perhaps the most accurate way of obtaining load data however special consideration must be taken to ensure accuracy. The sampling period of measurements must be well considered as a larger period will increase the margin of error and lead to under-representation of the demand profile. Furthermore, the accuracy class of the measuring instrument will affect the uncertainty of the measured data. Performing direct measurements for load modelling is an exhaustive method as the data needs to be recorded for an extended period for database construction. To liberalise research, datasets have been made publicly available such as the South African NRS Domestic Load Research Project [98], the Portuguese SINAIS research project [99] and the IEEE public datasets [97]. These have the benefits of including various residential consumer class and sampling periods.

Appliance modelling is a bottom-up method to build the demand profile. The contribution of individual appliances is modelled and aggregated to produce consumer demand profile. This method allows for the adjustment of the ADMD because of the addition or removal of individual appliances without much inconvenience. However, [96] warns that this method tends to under-estimate the demand for high consumer classes.

3.2.2.7 Load Design

The load is modelled in DIgSILENT using the built-in load model. The single-phase model was used with the phase used the same as that of the PV-DG. Multiple scenarios are simulated to obtain useful data.

Initially the CIGRE Benchmark LV Model is simulated according to the specifications in [13]. The consumers are specified as three-phase loads with associated ADMDs. The network model is balanced and is therefore simulated as such.

The network model is then modified as detailed in Section 3.2.2.5, to cater for an unbalanced scenario. The load is modelled according to the demand profile of [97] of which Figure 3.11

depicts an example of the daily profile. This is done for both when the network is operating in grid-connected mode and in islanded mode.

3.2.2.8 Distributed Generation Modelling

As discussed in Section 2.1.1, for relevance PV is the modelled DG. The production of PV is subject to the persisting weather conditions at the installation site. Furthermore, the time of day and positioning of the PV panels influences the power produced. Figure 3.12 shows the typical PV generation as well as the household electricity demand for a specific period. As can be seen, the power produced occurs during daylight hours with the presence of irradiance from the sun.

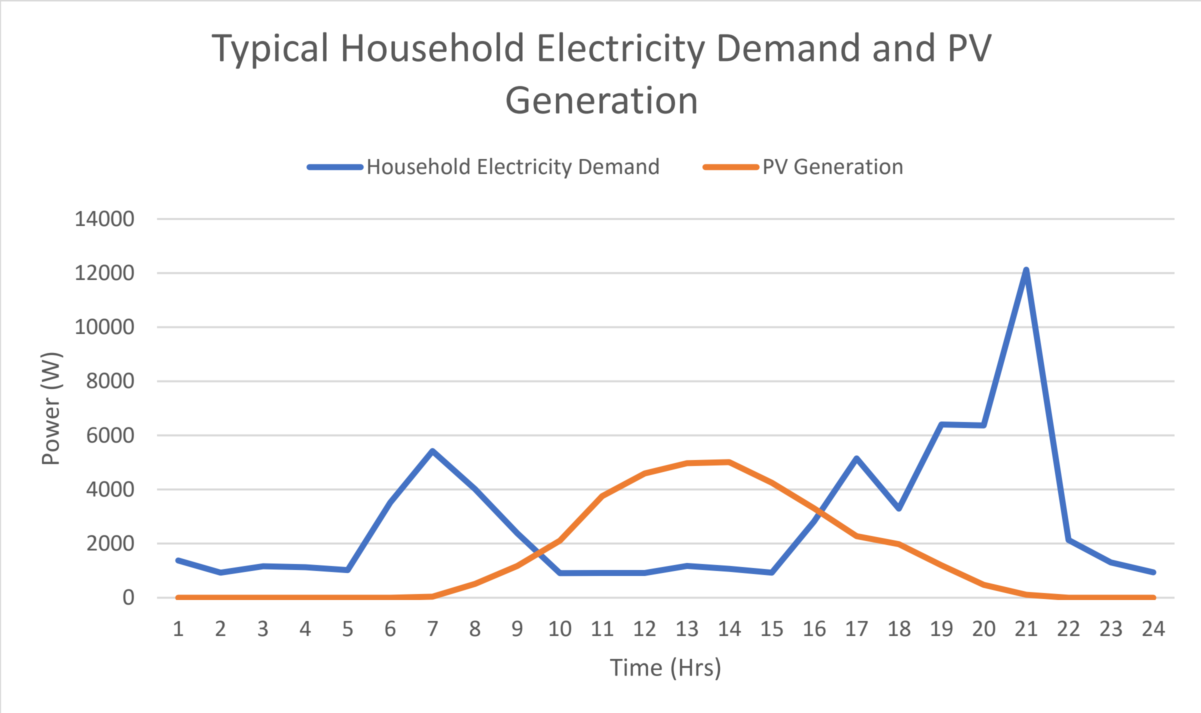

Figure 3.12: Typical Household Electricity Demand and PV Generation

The PV system typically compromises of:

- PV panels.
- DC/AC converter.
- Control system.
- Batteries (optional)

The regulations for the interconnection and interoperability of PV systems with distribution systems are detailed in IEEE 1547 [68]. Consideration is given to the power factor, voltage control, frequency control, Q control and power production control modes. As previously discussed in Section 2.3.3, the focus of this research will be on Category I performance parameters. The PV system can be modelled using various methods which include mathematical modelling, direct measurement, and geographic location irradiance.

The mathematical modelling of a PV system can be done using multiple approaches. In [85], it was recognised that the daily profile output from the PV is dependent on the season and time of day. Therefore, the output during any interval could be expressed as a probability density function. This statistical approach made use of the Beta PDF. The PV system in [100] was modelled as a single diode model with a parallel and series resistance. The advantages of the approach taken is that it is only dependent on parameters available in the manufacturer's datasheet and that the descriptive equation means that the equivalent circuit can be easily simulated.

The production profile can also be modelled according to the actual field data. This is accomplished by directly measuring the output of an operating PV system. This is the better method for obtaining production data but, as with load data collection, this is an exhaustive process which requires hardware setup and accurate measuring instruments. Moreover, the data collection must be completed over an extended period to build a database. The sampling period of measurements must be well considered as a larger period will increase the margin of error and lead to under-representation of the production profile. Furthermore, the accuracy class of the measuring instrument will affect the uncertainty of the measured data. Public PV production datasets are available such as the SINAIS research project [99] and the IEEE datasets [97].

Industry standard power system simulators such as DIgSILENT have built-in PV system models. These models are based on practical industry PV systems. The internal solar calculation performed by the models incorporates the Global Positioning System (GPS) coordinates of the installation site. Thus, for a site the practical solar irradiance is used to generate the PV production profile. The simulation model provides for specificity regarding the solar tracking and mounting.

3.2.2.9 DG Design
The PV system was modelled in DIgSILENT using the built-in solar PV system module type (PVD1). A single-phase PV module was used with the phase the same as the load. This was set to operate with a single inverter at unity power factor. The power production of the PV panels was obtained from the IEEE PV datasets [97] with an example of a daily profile shown in Figure 3.12.

3.2.3 Cable Modelling

3.2.3.1 Objective
The objective of modelling the cable is to determine the cable's impedance characteristics. Determining this can be achieved via the following methods:

1. Cable catalogue from manufacturer
2. Analytical method
3. Finite element model
4. Experimental method

Each possible method will be explored as each can give differing results. The result of which, will help answer the research question of the impact an accurately modelled cable network has on the fault location algorithm.

3.2.3.2 Manufacturer cable catalogue
Obtaining impedance values from the cable catalogue is the most common method used in cable design and modelling. Cable catalogues normally contain information about the different cable size, core dimensions, mass, current rating, short-circuit rating, voltage drop and impedance. The impedance value would be the ac resistance of the core. This information is sufficient for an engineer doing cable design for a network but is insufficient for a researcher

needing to model the cable. However, certain manufacturers provide more detailed information such as the DC resistance, reactance, capacitance, and zero-sequence resistance and reactance. These values are sufficient to fully characterise the cable. Figure 3.13 shows a sample of the cable cross-section and the dimensioning is detailed in Table 3.2.

Figure 3.13: Sample cross-section of $95mm^2$ cable and dimensions

Table 3.2: Parameters for 4-core $95mm^2$ cable from CBI electric

			Conductor size $95\ mm^2$
Physical Parameters	Sector area, mm^2		132.732
	Sector radius, mm (based on direct measurement)		13
	Copper strand diameter, mm (based on direct measurement)		3.5
	Armouring strand diameter, mm (based on direct measurement)		2
	Insulation thickness, mm (based on direct measurement)		1.5
	Number of strands		19
	Sheath thickness, mm (based on direct measurement)		3
	Insulation dieletric constant (Kersting)		2.3
	Conductor depth, mm		11.0
	Insulation depth, mm		14.5
Electrical Parameters	Current rating, A (in ground)		245
	DC resistance, Ω/km @20°C		0.193
	Positive sequence impedance, Ω/km @70°C		0.232 + j0.071
	Zero sequence impedance, Ω/km		3.265 + j0.062
	Capacitance, µF/km		1.709
	Short circuit ratings	Symmetrical, kA (1sec)	12.1
		Earth fault, kA (1sec)	8.6
	Volt drop mV/A/m (Three Phase)		0.42

The cable selected from CBI electric manufacturers provides the AC resistance and reactance, and the zero-sequence resistance and reactance. These values are sufficient to model the cable in software.

3.2.3.3 Analytical Method

Section 3.2.2.3 discusses the common analytical approaches to feeder sizing. The deterministic approach is taken in this research and the cable model used in the voltage drop calculations considers the resistive element of the conductor solely. Therefore, this model approach will make the same considerations to determine the effect this has.

3.2.3.4 Finite element model

The impedances are also calculated using finite element (FE) modelling for further comparison. The finite element model was developed using FEMM [101], which is a freely available software package.

A current carrying conductor produces a magnetic field around it. Consequently, eddy currents are induced in conductors within the magnetic field. These eddy currents can be modelled in detail using the FE method. The approximations and assumptions made are the same as those made in Section 3.2.2.3. The geometry of the cable was constructed in FEMM. For a DC current, the FEMM model will provide the dc resistance of the cable. For an AC current, the model will provide the AC impedance and capacitance of the cable. From these values, an impedance matrix of the cable can be constructed.

3.2.3.5 Experimental method

As mentioned previously in Chapter 1, most studies have been performed on primary distribution voltage levels with few being performed on LV. This is because of the highly resistive network at low voltages which allows for Ohm's law to be used for predictive purposes. However, in formulating a voltage-based fault location method, it becomes important to practically characterise the cable impedance to reduce approximations and uncertainties. Therefore, this experiment had the following objectives:

1. Verify the cable impedance model.
2. Verify the calculation of voltage drops along the cable.
3. Provide a high-resolution reference so that the impact of using lower resolution monitoring data can be assessed.

This will be completed by performing experiments to determine:

1. DC resistance.
2. Positive-sequence impedance.
3. Zero-sequence impedance
    a. With neutral and armouring bonded.
    b. With neutral bonded.
    c. With armouring bonded.

The cable used is the 95 mm^2 CBI 4 Core Copper Cable 600/1000V SANS 1507, as used for the proposed microgrid configuration. The test circuit to calculate the DC resistance is shown below in Figure 3.14.

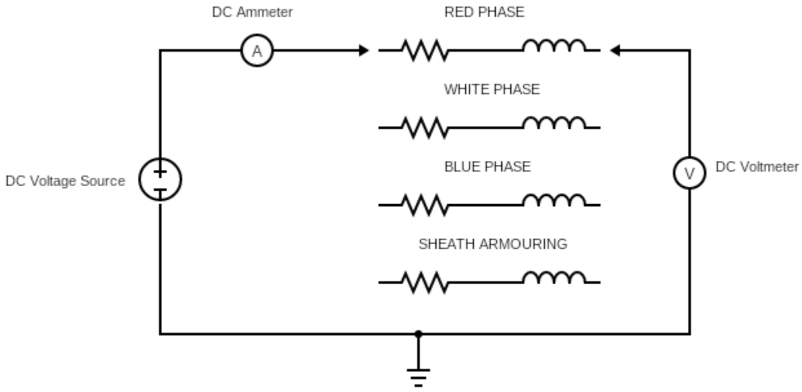

Figure 3.14: Experiment 1 - DC resistance

Each of the conductors, in turn, is excited from the DC source. The subsquent voltage drop is used to calculate the DC resistance of the conductors.

The test circuit to calculate the positive-sequence impedance is shown below in Figure 3.15.

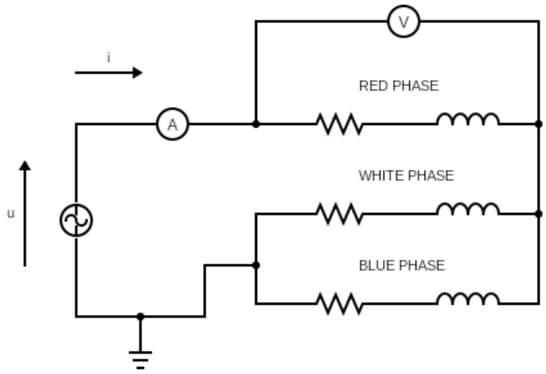

Figure 3.15: Experiment 2 - Positive-sequence impedance.

The circuit is setup as shown in Figure 3.15 with the red phase excited and the other phases used as the return path. The current flowing through the excited phase and the voltage with respect to ground are measured to obtain the positive-sequence impedance. This setup is repeated for the other two phases and an average for the positive-sequence impedance can be calculated.

The test circuit to calculate the zero-sequence impedance with both the neutral and armouring bonded is shown in Figure 3.16.

The circuit is setup as shown in Figure 3.16 with the phase conductors excited using the AC source and the sheath armour and neutral used as a return path. The current flowing through the excited conductors and the voltage with respect to ground are measured to obtain the zero-sequence impedance.

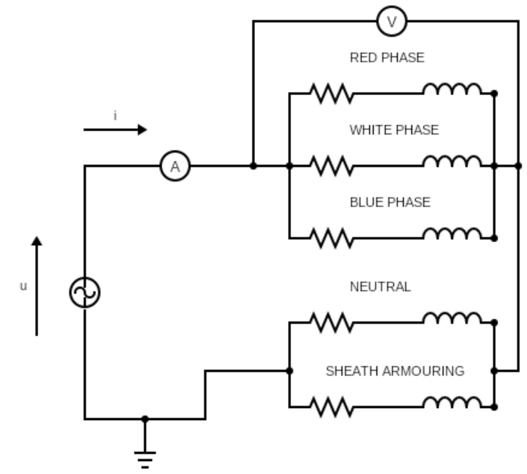

Figure 3.16: Experiment 3a - Zero-sequence impedance with neutral and armouring bonded.

The test circuit to calculate the zero-sequence impedance with the neutral bonded is shown below in Figure 3.17.

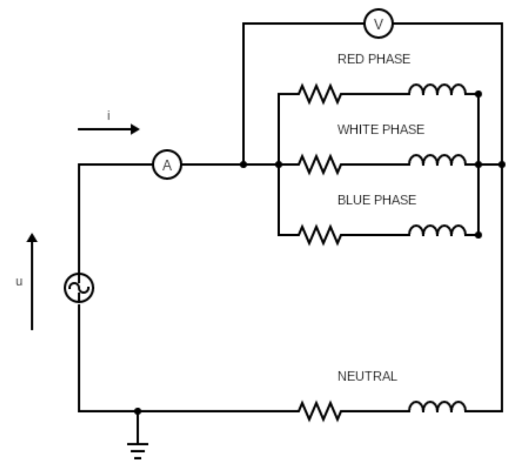

Figure 3.17: Experiment 3b - Zero-sequence impedance with neutral bonded.

The circuit is setup as shown in Figure 3.17 with the phase conductors excited using the AC source and the neutral used as a return path. The current flowing through the excited conductors and the voltage with respect to ground are measured to obtain the zero-sequence impedance.

The test circuit to calculate the zero-sequence impedance with the sheath armouring bonded is shown in Figure 3.18.

The circuit is setup as shown in Figure 3.18 with the phase conductors excited using the AC source and the sheath armouring used as a return path. The current flowing through the excited conductors and the voltage with respect to ground are measured to obtain the zero-sequence impedance.

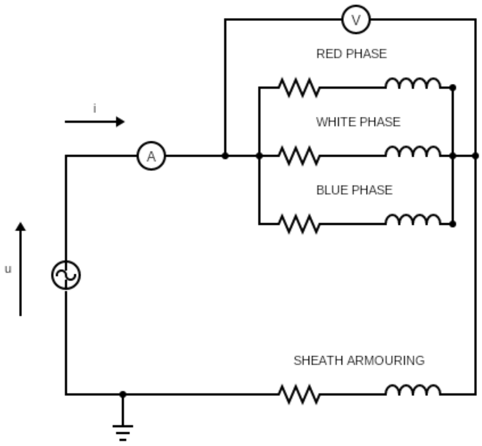

Figure 3.18: Experiment 3c - Zero-sequence with armouring bonded.

3.2.4 Simulations

3.2.4.1 Objective

The objective of the simulations is to generate the RMS voltages and profile along the feeder for the different operating conditions. This will provide the data upon which the fault location algorithm is formulated from.

3.2.4.2 Procedure

The simulations were performed using DIgSILENT.

To account for the various network configurations, simulations were conducted for the operating conditions shown in Table 3.3.

Voltage measurements are at each consumer node to emulate smart meter measurements. The study also accounted for lack of the consumer smart meter data and include the impact of this possibility. The faults studied were balanced and unbalanced faults as well as faults at varying fault resistance levels.

The expected voltage profile of the feeder is shown in Figure 3.19. It is shown that the shape of the profile differs depending on the presence of DG and will further differ depending on the DG penetration amount.

Figure 3.20 shows the voltage profile of the feeder when there is a fault and no DG present downstream of the fault. This profile will differ further depending on the location of the fault and the DG penetration amount.

Figure 3.21 shows the voltage profile of the feeder with a fault and DG downstream of the fault. This profile will differ further depending on the location of the fault and the DG penetration amount. The voltage profile along the feeder will drop up until the fault point after which it is expected to rise because of the downstream DG.

Table 3.3: Network Operating conditions

	Fault resistance	Grid-connected mode		Islanded mode
		No DG	DG	DG
Normal Operating conditions	N/A			
Single-Phase-to-ground fault	5Ω	Beginning of feeder & Middle of feeder & End of feeder		
	50Ω	Beginning of feeder & Middle of feeder & End of feeder		
	500Ω	Beginning of feeder & Middle of feeder & End of feeder		
Single-Phase-to-neutral fault	5Ω	Beginning of feeder & Middle of feeder & End of feeder		
	50Ω	Beginning of feeder & Middle of feeder & End of feeder		
	500Ω	Beginning of feeder & Middle of feeder & End of feeder		
Single-Phase-to-neutral-to ground fault	5Ω	Beginning of feeder & Middle of feeder & End of feeder		
	50Ω	Beginning of feeder & Middle of feeder & End of feeder		
	500Ω	Beginning of feeder & Middle of feeder & End of feeder		
Phase-to-phase fault	5Ω	Beginning of feeder & Middle of feeder & End of feeder		
	50Ω	Beginning of feeder & Middle of feeder & End of feeder		
	500Ω	Beginning of feeder & Middle of feeder & End of feeder		
Phase-to-phase-to-neutral fault	5Ω	Beginning of feeder & Middle of feeder & End of feeder		
	50Ω	Beginning of feeder & Middle of feeder & End of feeder		
	500Ω	Beginning of feeder & Middle of feeder & End of feeder		
Three-phase fault	5Ω	Beginning of feeder & Middle of feeder & End of feeder		
	50Ω	Beginning of feeder & Middle of feeder & End of feeder		
	500Ω	Beginning of feeder & Middle of feeder & End of feeder		

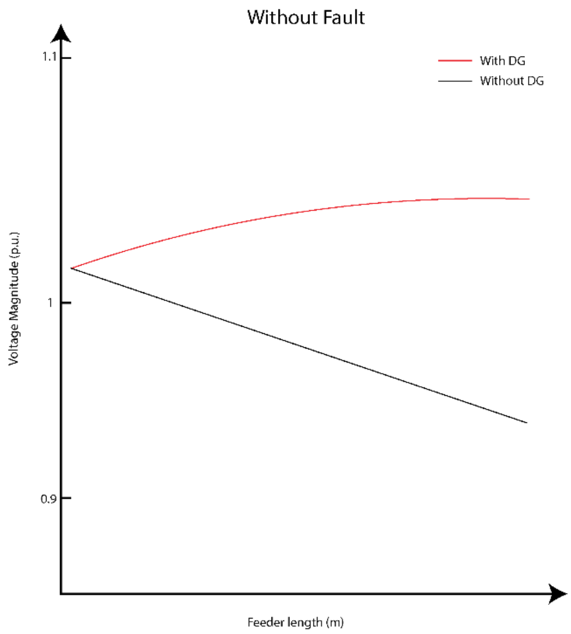

Figure 3.19: Voltage-profile without fault

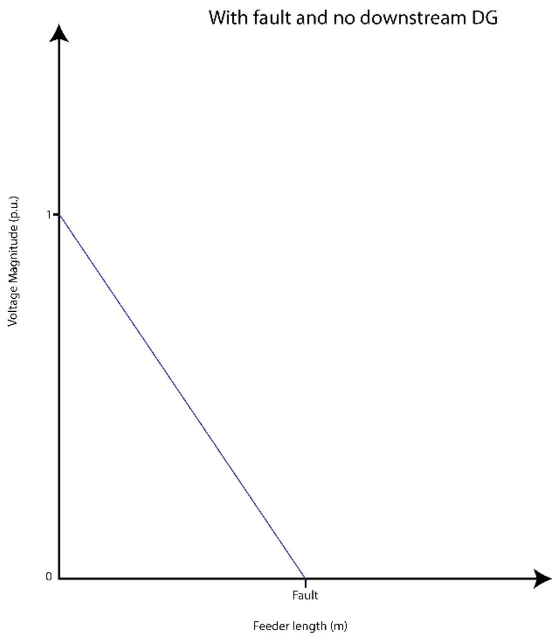

Figure 3.20: Voltage-profile with fault

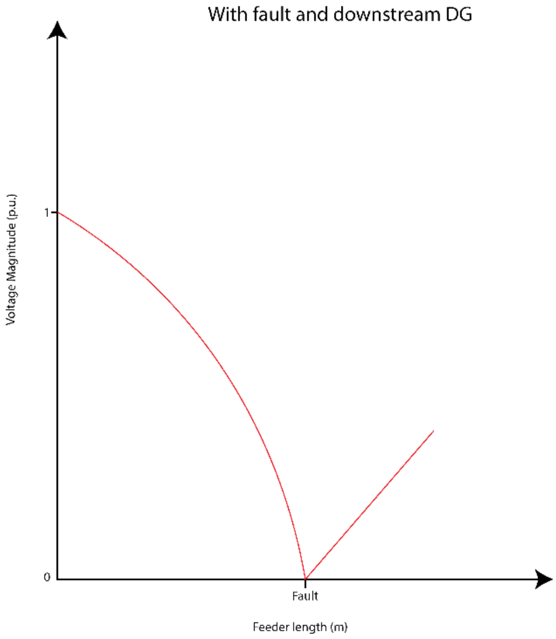

Figure 3.21: Voltage-profile with fault and DG

3.2.5 Analysis

3.2.5.1 Objective

The objective of the analysis is to evaluate the data and formulate a fault location algorithm. The algorithm has the requirements of being able to adapt to network operating conditions, operate within standard specifications and be accurate.

3.2.5.2 Procedure

As shown in Figure 3.19 to Figure 3.21, the voltage profile of the feeder can vary depending on the network operating conditions. It is proposed that the algorithm be adaptable to these conditions by recognising the pre-fault and faulted network conditions. Recognition of the pre-fault network conditions will enable operation classification such as whether the microgrid is grid-connected or islanded, presence of DG or not and DG penetration amount. Therefore, a comparison between the pre-fault voltage profile and the faulted voltage profile can be made. This approach avoids the false location of a presumed fault when it is just a change in the network operation. A circular buffer is used to retain previous voltage values. The procedure is illustrated below in Figure 3.22.

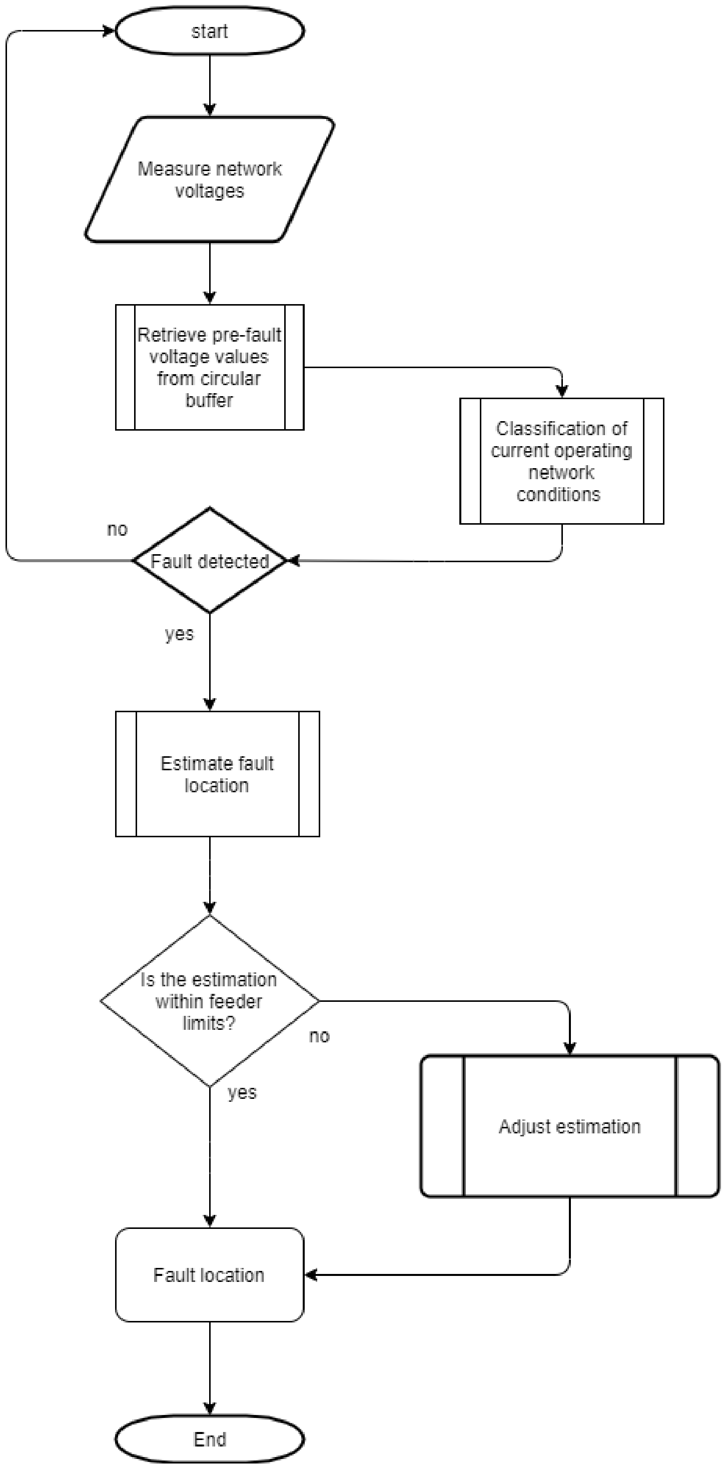

Figure 3.22: Proposed fault detection and location procedure.

Upon the detection of a change in the measured voltage values from the smart meters, a retrieval of the pre-change voltage values, from the circular buffer, is completed. Subsequently, the two voltage profiles are compared using the DTW algorithm (Section 2.2.6) and a classification of the network operating conditions is done. If a fault is detected, the location of the fault is determined from the maximum deviation found using the DTW algorithm detailed in Figure 3.23.

Algorithm: Finding minimum distance

```
Lowest global distance = infinity
For i in template frame:
    For j in test frame:
        Lowest global distance = global distance[i-1][j]
        If global distance[i][j-1] < Lowest global distance:
            Lowest global distance = global distance[i][j-1]
        If global distance[i-1][j] < Lowest global distance:
            Lowest global distance = global distance[i-1][j]
        Global distance[i][j] = Lowest global distance + local distance(template[i],test[j])
```

Figure 3.23: Dynamic Time Warping algorithm

The advantage of the DTW algorithm is its ability to recognize distortions in two separate datasets regardless of whether they have the same frame length. Its disadvantage is its inability to show the point at which these distortions occur. To compensate for this, keeping a record of the transitions made and the cost associated with each transition can be kept. A transition associated with a high cost indicates a distortion between the test and template frames.

3.3 Summary of the Research Methodology and Approach

Table 3.4: Summary of the research methodology

Research Questions	Objectives	Methodology	Expected results
How effective will be a method of detecting, classifying, and locating faults in a LV microgrid if it is based on the voltage measurements from smart meters, especially with high penetration of IIDGs?	To develop an algorithm that can detect, classify, and locate faults in a LV microgrid with high penetration of IIDGs by using voltage measurements from smart meters.	This will be investigated by: • Accurately modelling and simulating a LV microgrid. • Simulating faults in the varying operating conditions of a microgrid. • Analysing resulting RMS voltages recorded from smart meter locations.	A scheme that can accurately detect, classify and locate faults in a LV microgrid with a high penetration of IIDGs.

Can the accuracy of meters as specified in SANS 62053-22:2018 be extended to readings outside the nominal voltage range and will this accuracy be adequate?	To find the level of accuracy of a smart meter required to provide readings outside the nominal voltage range adequate for the algorithm.	This will be investigated by evaluating the performance of the proposed algorithm with the SANS 62053-22:2018 accuracy level as well as higher accuracy levels.	An evaluation of the effect of the SANS 62053-22:2018 on the proposed algorithm as well as a recommendation for accuracy levels for smart meters used in fault detection, classification and location.
What effect does an accurately modelled LV feeder have on the performance of a fault location scheme as opposed to the present methods of modelling LV feeders?	To find the effects of the accuracy of the modelled feeder on the performance of the algorithm.	The LV feeder will be modelled by: • Building an impedance model based on the manufacturer's catalogue. • Constructing a finite element model based on the actual geometry and material properties of the conductor. • Performing laboratory experiments on a cable section to validate the model.	An accurate model of the specific low voltage feeder with a comparison of its characteristics made from the models. A comparison of the performance of the proposed algorithm using the different impedance models will be presented.

Chapter 4: Results

The following sections outline the results from the simulations and experiments detailed in the preceding chapter.

4.1 Cable Modelling

The cable catalogue [102] provides both the positive- and zero-sequence impedances for the cable. Using (10) and (11), the phase impedance matrix can be derived from the sequence-components matrix as shown in Table 4.1.

Table 4.1: Catalogue impedance model

DC Resistance Ω/km	0.193
Sequence-components model, Ω/km	$Z_{012} = \begin{bmatrix} 3.2655\angle 1.09° & 0 & 0 \\ 0 & 0.24246\angle 17.02° & 0 \\ 0 & 0 & 0.24246\angle 17.02° \end{bmatrix}$
Phase model, Ω/km	$Z_{abc} = \begin{bmatrix} 1.265 + j0.068 & 1.033 + j0.003 & 1.033 + j0.003 \\ 1.033 + j0.003 & 1.265 + j0.068 & 1.033 + j0.003 \\ 1.033 + j0.003 & 1.033 + j0.003 & 1.265 + j0.068 \end{bmatrix}$

The manufacturer's catalogue details the cable's electrical parameters, Table 3.2, however it does not detail the experimental set-up to obtain those parameters. Therefore, this introduces uncertainty in the validation process particularly with the zero-sequence component as its value is dependent on the earthing method employed (Section 2.1.2.3). Therefore, it is possible to have an installation whereby the sheath armouring of the cable is earthed and the neutral is unearthed or the sheath armouring is unearthed and the neutral is earthed or both the sheath armouring and the neutral are earthed. Depending on the choice of the designer, the armouring is bonded with the earth to provide an earth continuity path [103] thereby altering the current return path. This uncertainty is considered in the experimental procedure.

As the manufacturer's datasheet does not provide mutual coupling data this is assumed to be zero. Therefore, there is no coupling in the sequence matrix and the phase impedance matrix is balanced [89].

4.1.1 Simulation

As discussed in Section 3.2.3, FEMM is also used to determine the cable parameters. The finite-element method is used to solve the magnetic field and current distribution of the planar cross-section of the cable geometry. Figure 4.1 shows the FEMM model which gives the impedances per unit length. The cross-section of the cable is shown with the four conductor sectors that are filled with copper strands. The space between the conductor strands is occupied by the polyvinyl chloride (PVC) insulation. The steel wire strands form the outer armouring of the cable.

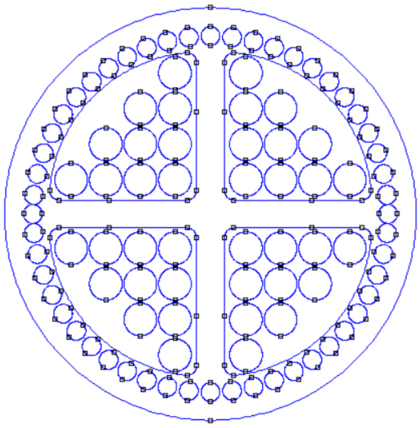

Figure 4.1: FEMM model of 4-core $95mm^2$ *cable*

Figure 4.2 shows the solution of the model when simulated using TN-C-S grounding so the earth and neutral are separated at the customer. In order to keep the magnetic flux from crossing the problem boundary, a Dirichlet-type boundary condition is defined whereby the potential at the boundary is explicity defined as zero, A = 0. This truncates the magnetic field at the boundary radius and a magnetic relative permeability of 1 is assumed.

An AC current of +1 A was applied to an 'active' conductor and the two other phase conductors had an AC current of -0.5 A, providing the return path for the current. The neutral conductor had an AC curent of zero which prevented circulating current between the conductors but allowed for the presence of eddy currents. The color contour plot in Figure 4.2 shows the current density generated. As can be seen, there is uniform current distribution showing the small effect eddy currents and proximity effect have at the low frequency of 50 Hz.

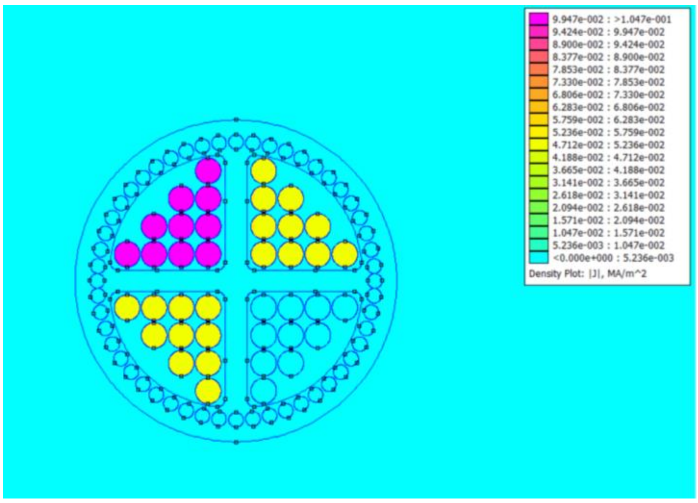

Figure 4.2: FEMM magnetics solution of 4-core $95mm^2$ *cable*

The FE runs the simulation for each individual strand, both for the copper phase and neutral conductors and for the steel wire armouring. This allows for a constant voltage to be applied across the surface of the conductors and the software to only model the longitudinal currents. However, this 2D simulator does not provide for the consideration of the uncertainties due to the cable lay as the longitudinal position of the strands is fixed. Over a given length, each section has an approximatley equal probability of being at any angle relative to each other [90] provided lay lengths are not exact repetitions. Therefore, this most likely would be negligible due to the low workability of the cable. The bending radius would be so large that any mutual coupling would be negligible. Furthermore, in a worst case scenario of a 90° bending radius, there would be no mutual coupling as the fluxes from both sections would be perpendicular.

The simulaton was run for both the positive and zero-sequence impedances, with a knowledge that the positive and negative-sequence impedances are equal [92]. Using (3.10) and (3.11), the phase impedance matrix is derived and is shown in Table 4.2.

Table 4.2: Finite element impedance model

DC resistance Ω/km	0.1918
Sequence-components model, Ω/km	$Z_{012} = \begin{bmatrix} 3.152\angle 1.34° & 0 & 0 \\ 0 & 0.236\angle 17.18° & 0 \\ 0 & 0 & 0.236\angle 17.18° \end{bmatrix}$
Phase model, Ω/km	$Z_{abc} = \begin{bmatrix} 1.201 + j0.071 & 0.97521 + j0.0013 & 0.97521 + j0.0013 \\ 0.97521 + j0.0013 & 1.201 + j0.071 & 0.97521 + j0.0013 \\ 0.97521 + j0.0013 & 0.97521 + j0.0013 & 1.201 + j0.071 \end{bmatrix}$

4.1.2 Experiment

To validate the previous cable models, it is necessary to experimentally generate the impedance model of the cable. As discussed earlier, the grounding method is uncertain therefore the experimental procedure included the scenarios where the neutral is earthed, the armouring is earthed and, both the neutral and armouring are earthed. The experimental procedure is described in Section 3.2.3.5 and the results obtained are shown in

Table 4.3.

The cable selected was 38 m long. As a 4-core 95mm^2 cable, the cable was very rigid and had poor workability. Nonetheless, it is important to ensure that both ends of the cable are close together to reduce the length of the probe wires. This is to limit any measuring error due to the induced voltages in the additional wiring. To find the positive-sequence impedance, the circuit was set up as shown in Figure 3.15 and the experimental procedure followed as outlined in Section 3.2.3.5. The positive-sequence impedance equals the positive-sequence voltage divided by the positive-sequence current.

$$Z_1 = \frac{V_1}{I_1} \tag{4.1}$$

To find the zero-sequence impedance, the circuit was set up as shown in Figure 3.16 to Figure 3.18 and the experimental procedure followed as outlined in Section 3.2.3.5. The zero-sequence impedance equals the zero-sequence voltage divided by the zero-sequence current.

$$Z_0 = \frac{V_0}{I_0} \tag{4.2}$$

Table 4.3: Experimental impedance model

Experiment impedance model	
DC Resistance, Ω/km	0.1703
Experiment with neutral earthed	
Sequence-components model, Ω/km	$Z_{012} = \begin{bmatrix} 3.1862\angle 3° & 0 & 0 \\ 0 & 0.25463\angle 4° & 0 \\ 0 & 0 & 0.25463\angle 4° \end{bmatrix}$
Phase model, Ω/km	$Z_{abc} = \begin{bmatrix} 1.22995 + j0.06747 & 0.97594 + j0.04961 & 0.97594 + j0.04961 \\ 0.97594 + j0.04961 & 1.22995 + j0.06747 & 0.97594 + j0.04961 \\ 0.97594 + j0.04961 & 0.97594 + j0.04961 & 1.22995 + j0.06747 \end{bmatrix}$
Experiment with armouring earthed	
Sequence-components model, Ω/km	$Z_{012} = \begin{bmatrix} 10.596\angle 2° & 0 & 0 \\ 0 & 0.25463\angle 4° & 0 \\ 0 & 0 & 0.25463\angle 4° \end{bmatrix}$
Phase model, Ω/km	$Z_{abc} = \begin{bmatrix} 3.6992 + j0.1351 & 3.4452 + j0.1173 & 3.4452 + j0.1173 \\ 3.4452 + j0.1173 & 3.6992 + j0.1351 & 3.4452 + j0.1173 \\ 3.4452 + j0.1173 & 3.4452 + j0.1173 & 3.6992 + j0.1351 \end{bmatrix}$
Experiment with both neutral and armouring earthed	
Sequence-components model, Ω/km	$Z_{012} = \begin{bmatrix} 2.57118\angle 2° & 0 & 0 \\ 0 & 0.25463\angle 4° & 0 \\ 0 & 0 & 0.25463\angle 4° \end{bmatrix}$
Phase model, Ω/km	$Z_{abc} = \begin{bmatrix} 1.025 + j0.06262 & 0.771 + j0.4486 & 0.771 + j0.4486 \\ 0.771 + j0.4486 & 1.025 + j0.06262 & 0.771 + j0.4486 \\ 0.771 + j0.4486 & 0.771 + j0.4486 & 1.025 + j0.06262 \end{bmatrix}$

4.1.3 Discussion

The impedances of the CBI 4-core $95\ \mathrm{mm}^2$ cable were obtained using the manufacturer's catalogue impedances, FE impedances, and experimental impedances. Using the catalogue impedance model, Table 4.1, as a baseline for comparison, it can be seen that the FE impedances provide a good approximation of the impedance matrix. A 0.6% error difference for the DC resistance is seen. The error difference for the positive- and zero-sequence impedance is 2.7% and 3.5% respectively at 50 Hz. These are expected to diverge at harmonic frequencies [104] however within this research, the primary concern was the cable impedance at the fundamental frequency, 50Hz.

The experimental procedure was performed to investigate the effect that different grounding methods would have on the impedance model. The error difference for the positive-sequence impedance is 4.95% however the experimental reactance is found to be much larger than expected. The positive-sequence impedance is the same regardless of the grounding method used as it is due to the phase conductors whereas the zero-sequence impedance is affected by the grounding method. The largest error difference is seen when the armouring is grounded, and the neutral is ungrounded with a 224% increase in the zero-sequence impedance. This large difference is due to the high resistance of the steel wire armouring that provides the return ground path. With the neutral grounded and the armouring ungrounded, there is a 2.4% decrease in the zero-sequence impedance. The similarity in this value indicates that this could be the grounding type used by the manufacturers to determine the zero-sequence impedance as this is within the margin of error. With both the neutral and armouring grounded, the error difference is a 21.3% decrease in the zero-sequence impedance. Although quite a difference from the value in the manufacturer's catalogue, this grounding type is chosen to be implemented in this work as it is good grounding practice [103] and is most likely used in the field.

4.2 LV Network Modelling

The CIGRE Benchmark LV Model from Figure 3.*4* was simulated in DIgSILENT. The following sections detail the simulation results from the CIGRE model and from the modified network according to the operating scenarios presented in Table 3.*3*.

4.2.1 CIGRE Benchmark LV Model

As outlined in [13], LV networks with single-phase consumers are inherently unbalanced however in this model only three-phase consumers are specified therefore the model is a balanced network. This limitation, with regards to the scope of this research, is addressed with the modified network model (Section 4.2.2). The CIGRE Benchmark LV Model also provides for a number of different DG types however PV is primarily used to contextualize the simulation. Figure 4.3 shows the simulated model with the added DG.

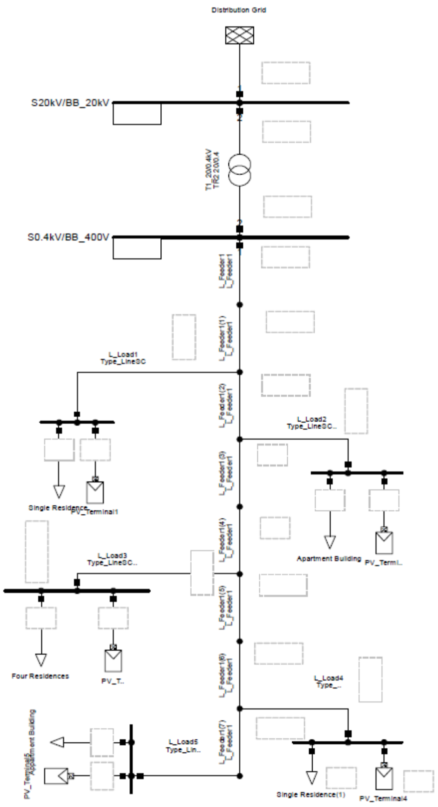

Figure 4.3: CIGRE Benchmark LV Model

The feeder voltage profile is shown in Figure 4.4. This figure shows a comparison of the voltage readings between the network without DG and when operating with DG.

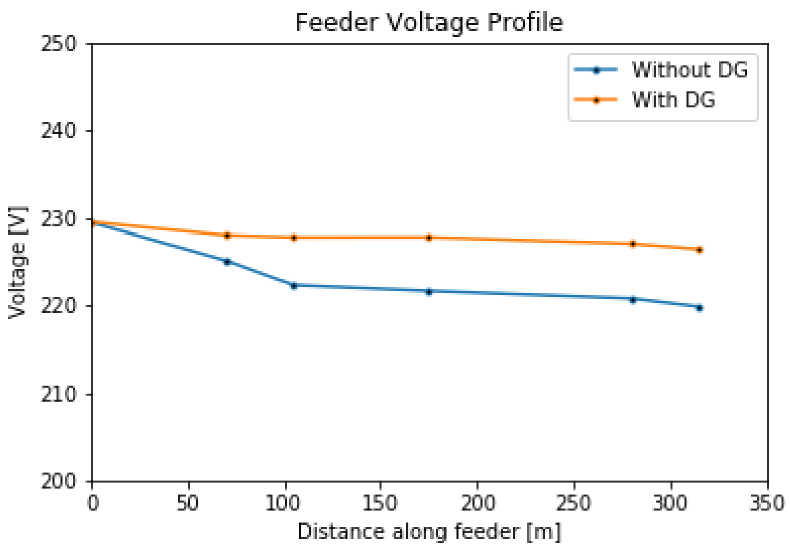

Figure 4.4: CIGRE Benchmark LV Model Feeder Voltage Profile Comparison

The plot shows the voltage at the consumer terminal against the distance along the feeder. The position of the consumer terminals along the feeder are indicated by the node points on the voltage curves. As expected, the voltage profile of the network improves with the addition of DG as the voltage drop is less than when there is no DG.

Figure 4.5 to Figure 4.7 show the fault locations at the beginning, middle and end of the feeder, respectively. These positions are chosen to assess the impact of fault location on the voltage profile of the feeder.

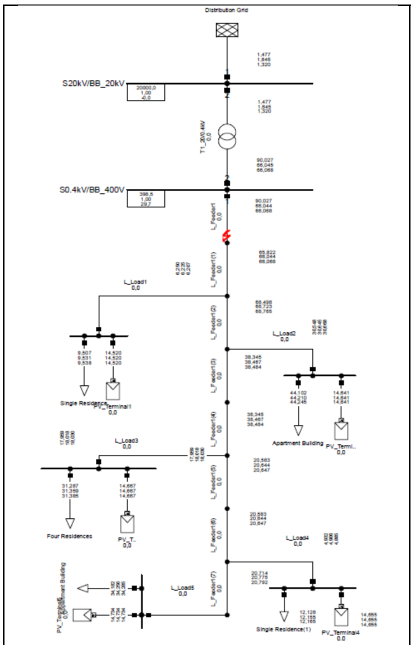

Figure 4.5: CIGRE Benchmark LV Model with fault at the beginning of the feeder

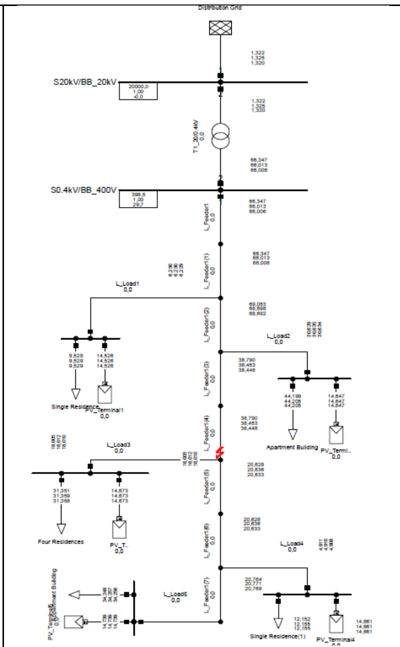

Figure 4.6: CIGRE Benchmark LV Model with fault at the middle of the feeder

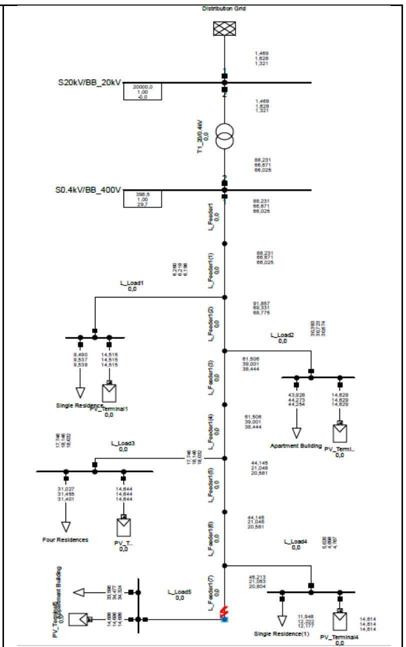

Figure 4.7: CIGRE Benchmark LV Model with fault at the end of the feeder

The fault resistance is varied between 5 Ω, 50 Ω and 500 Ω to assess the impact of fault current variation on the voltage profile of the feeder. This is initially performed on the network without the presence of DG and for a phase-to-ground fault on Phase A. The results are shown in Figure 4.8 to Figure 4.16. The results show the pre-fault and fault plots of all three phases with Phase A being the faulted phase.

With the presence of a PH-G fault on Phase A, it is seen that the Phase A voltage drops whilst the voltages on the other two non-faulted phases increase. This voltage asymmetry is greatest for the low-impedance faults and is lowest for the high-impedance faults. The comparison between pre-fault voltage levels and faulted voltage levels depicts a greater difficulty in detecting a low fault- current as the voltage levels are similar.

Table 4.4 to Table 4.6 give the percentage differences. The percentage differences are calculated using the following formula:

$$\%Diff = \frac{V_{ph-i,fault} - V_{ph-i,pre-fault}}{V_{ph-i,pre-fault}} \times 100 \qquad (4.3)$$

In Table 4.4, the quantitative results of the simulation of the network without DG and with a 5 Ω phase-to-ground fault are shown. The voltage difference due to the location, although not large, is noticeable. A fault can easily be detected as the voltage at the consumer's node is outside of the 10% limit of variation [26].

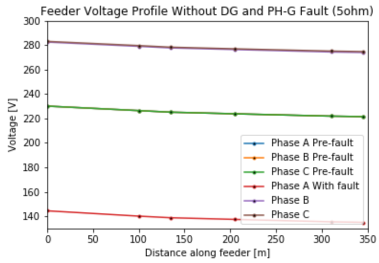

Figure 4.8: CIGRE Benchmark LV Model Voltage Profile without DG and PH-G 5Ω fault at the beginning of the feeder

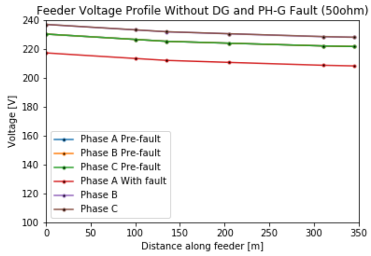

Figure 4.9:CIGRE Benchmark LV Model Voltage Profile without DG and PH-G 50Ω fault at the beginning of the feeder

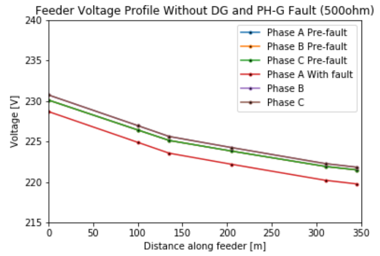

Figure 4.10: CIGRE Benchmark LV Model Voltage Profile without DG and PH-G 500Ω fault at the beginning of the feeder

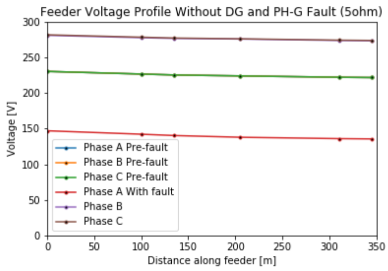

Figure 4.11:CIGRE Benchmark LV Model Voltage Profile without DG and PH-G 5Ω fault at the middle of the feeder

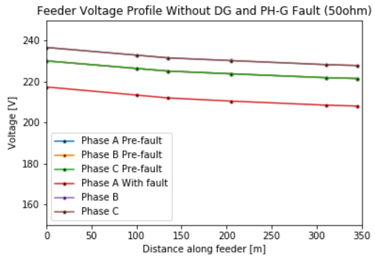

Figure 4.12: CIGRE Benchmark LV Model Voltage Profile without DG and PH-G 50Ω fault at the middle of the feeder

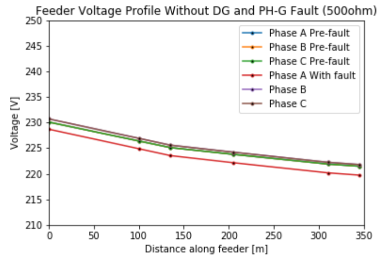

Figure 4.13: CIGRE Benchmark LV Model Voltage Profile without DG and PH-G 500Ω fault at the middle of the feeder

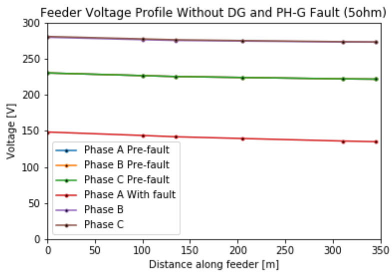

Figure 4.14: CIGRE Benchmark LV Model Voltage Profile without DG and PH-G 5Ω fault at the end of the feeder

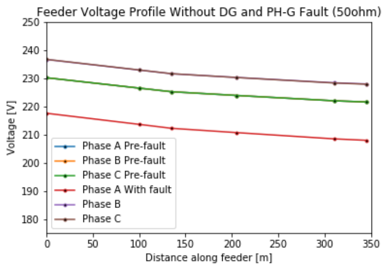

Figure 4.15: CIGRE Benchmark LV Model Voltage Profile without DG and PH-G 50Ω fault at the end of the feeder

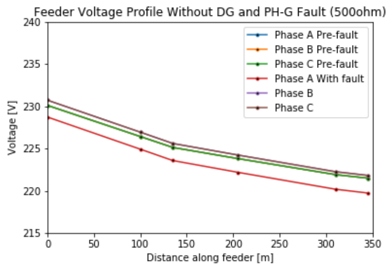

Figure 4.16: CIGRE Benchmark LV Model Voltage Profile without DG and PH-G 500Ω fault at the end of the feeder

It is seen that with the fault at the beginning of the feeder, the Phase A voltage difference is smaller at Node 0 and then increases at Node 1 to Node 5. Similarly, for Phase B and Phase C the voltage difference is smaller at Node 0 before increasing from Node 1 to Node 5. It is important to note that after the fault location, the phase voltage differences for the nodes differ much less as compared to before the fault location. This is further seen when the fault location is in the middle of the feeder, between Node 2 and Node 3; and furthermore, with the fault location at the end of the feeder, between Node 4 and Node 5.

It is also evident that with the balanced network, the faulted phase voltage differences are very similar.

In Table 4.5, the fault resistance is increased to 50 Ω. It is noticeable that the phase voltage differences are lower than with the previous simulation. With this decrease, the faulted voltages are within the limits of voltage variation. Furthermore, it is more difficult to recognise the location of the fault as the phase voltage differences do not vary substantially according to fault location.

Table 4.4: No DG & 5 Ω PH-G fault

Node	Beginning of the feeder			Middle of the feeder			End of the feeder		
	Phase A % diff	Phase B % diff	Phase C % diff	Phase A % diff	Phase B % diff	Phase C % diff	Phase A % diff	Phase B % diff	Phase C % diff
0	-37,1993501	22,7324	22,98074	-36,1653	21,94281	22,30716	-35,545	21,44015	21,93614
1	-38,0884659	23,18801	23,4651	-37,2485	22,47928	22,81872	-36,6015	21,95601	22,43437
2	-38,3247004	23,32165	23,59665	-37,712	22,71788	22,99534	-37,0528	22,18515	22,60556
3	-38,5704988	23,45381	23,7298	-38,423	23,06928	23,2234	-37,743	22,52064	22,82548
4	-38,9308999	23,6163	23,95727	-38,7615	23,2125	23,43722	-38,7816	22,99842	23,18545
5	-39,0128458	23,66069	23,99907	-38,8375	23,25113	23,47595	-39,0922	23,14903	23,27381

Table 4.5: No DG & 50 Ω PH-G fault

Node	Beginning of the feeder			Middle of the feeder			End of the feeder		
	Phase A % diff	Phase B % diff	Phase C % diff	Phase A % diff	Phase B % diff	Phase C % diff	Phase A % diff	Phase B % diff	Phase C % diff
0	-5,64604	2,891828	2,915961	-5,53254	2,831633	2,85361	-5,47995	2,80251	2,826009
1	-5,8183	2,903896	2,933016	-5,73533	2,85581	2,872582	-5,67981	2,824941	2,844158
2	-5,87217	2,900365	2,929045	-5,82405	2,866756	2,871964	-5,76715	2,835024	2,843217
3	-5,93102	2,892857	2,921655	-5,95404	2,889168	2,871462	-5,89464	2,855846	2,842252
4	-6,01726	2,876146	2,91668	-6,03733	2,870422	2,865309	-6,08573	2,883046	2,846814
5	-6,03752	2,87309	2,913137	-6,05677	2,866699	2,86154	-6,14127	2,894648	2,846664

In Table 4.6, the fault resistance is increased to 500 Ω. The percentage phase differences subsequently decreased to less than 1%. This is well below the limits of voltage variation therefore drastically increasing the difficulty of detecting a fault. Furthermore, the difficulty of locating the fault quantitatively increases as the effect of the mutual induction in the network changes with the decreased fault current.

Table 4.6: No DG & 500 Ω PH-G fault

Node	Beginning of the feeder			Middle of the feeder			End of the feeder		
	Phase A % diff	Phase B % diff	Phase C % diff	Phase A % diff	Phase B % diff	Phase C % diff	Phase A % diff	Phase B % diff	Phase C % diff
0	-0,61549	0,273734	0,275987	-0,60425	0,268389	0,270002	-0,59942	0,266072	0,267445
1	-0,67346	0,234763	0,23755	-0,66546	0,23068	0,231714	-0,66034	0,228203	0,229088
2	-0,69826	0,215145	0,217884	-0,69226	0,212549	0,212324	-0,68868	0,209992	0,209671
3	-0,72729	0,191387	0,194137	-0,73049	0,191857	0,189139	-0,72498	0,189147	0,18645
4	-0,76982	0,155983	0,160001	-0,77271	0,156255	0,154895	-0,77859	0,158257	0,15308
5	-0,78025	0,147324	0,151289	-0,78305	0,14753	0,146164	-0,79275	0,151102	0,144644

This quantitative analysis can similarly be done for all the different fault types.

The simulations are then performed with the presence of DG at the locations indicated in Figure 4.5. The power output from the DGs is the same as that detailed in the benchmark model [13] however the DG type was modified to PV. This is done to contextualize the research problem and has no quantitative effect on the static simulation. The results are shown in Figure 4.17 to Figure 4.25.

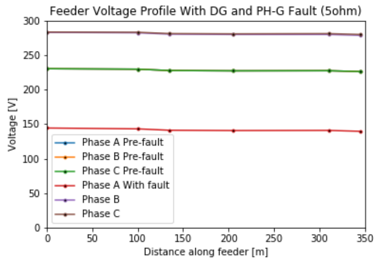

Figure 4.17: CIGRE Benchmark LV Model Voltage Profile with DG and PH-G 5Ω fault at the beginning of the feeder

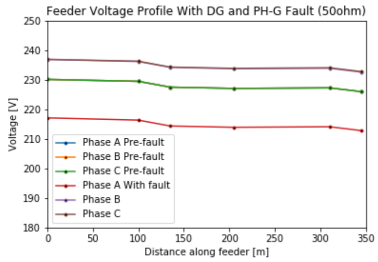

Figure 4.18: CIGRE Benchmark LV Model Voltage Profile with DG and PH-G 50Ω fault at the beginning of the feeder

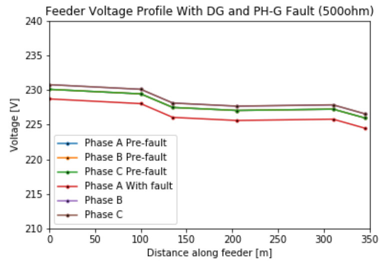

Figure 4.19: CIGRE Benchmark LV Model Voltage Profile with DG and PH-G 500Ω fault at the beginning of the feeder

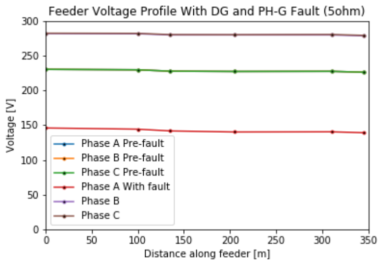

Figure 4.20: CIGRE Benchmark LV Model Voltage Profile with DG and PH-G 5Ω fault at the middle of the feeder

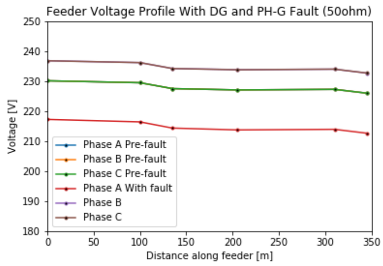

Figure 4.21: CIGRE Benchmark LV Model Voltage Profile with DG and PH-G 50Ω fault at the middle of the feeder

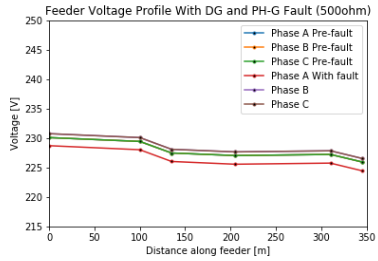

Figure 4.22: CIGRE Benchmark LV Model Voltage Profile with DG and PH-G 500Ω fault at the middle of the feeder

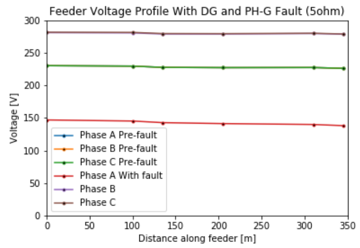

Figure 4.23: CIGRE Benchmark LV Model Voltage Profile with DG and PH-G 5Ω fault at the end of the feeder

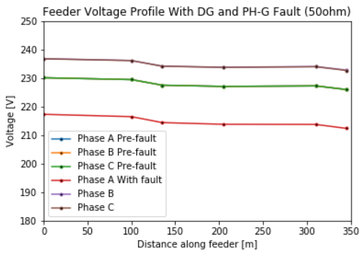

Figure 4.24: CIGRE Benchmark LV Model Voltage Profile with DG and PH-G 50Ω fault at the end of the feeder

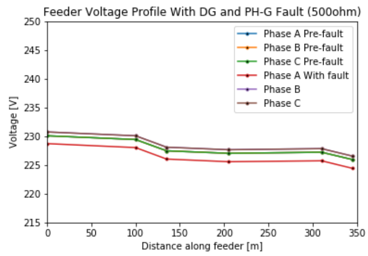

Figure 4.25: CIGRE Benchmark LV Model Voltage Profile with DG and PH-G 500Ω fault at the end of the feeder

Similar to the results with no DG present, the presence of a fault decreases the voltage on the faulted phase whilst increasing the voltage on the non-faulted phases. This difference is greatest when the fault impedance is low and smallest when the fault impedance is highest. With a quantitative analysis done, the voltage difference trend seen with no DG is continued with the presence of DG. Low-impedance faults result in voltages outside of the 10% limit for voltage variation whereas for the high impedance faults, the voltages measured are well within this range. This trend is similar for the different fault types.

Having established the difficulty of detecting the presence of a high-impedance fault solely from the voltage values, the procedure detailed in Section 3.2.5 is applied. The network operating under normal conditions with no DG is used as the reference template for the DTW algorithm. The Euclidean distance deviation is then calculated for all possible operating conditions with each being used as a test template. The results from the three phases are similar because it is a balanced network with any difference in phase voltage readings being minor. A comparison of the reference template with itself gives a Euclidean distance of zero, which is expected, and shows the ability of the system to recognise normal operating conditions. The introduction of DG in the network produces a distinct distance value that is used to classify the system as operating normally but with DG. Subsequently the different fault types, sizes and locations are simulated and compared, for when the system has DG present and not. The results for the Phase A voltages are tabulated in Table 4.7 below.

Table 4.7: DTW Euclidean distances for CIGRE Benchmark LV Model - Phase A

		PHASE A - GRID CONNECTED					
	Fault Size (Ω)	No DG			DG		
		B	M	E	B	M	E
No fault	---	0	0	0	6,645591	6,645591	6,645591
PHG	5	211,1558	208,4132	206,28	211,4559	210,8125	209,6506
	50	31,58158	31,25055	31,11865	32,10227	32,2556	32,32639
	500	3,026591	3,008673	3,01549	2,583073	2,592939	2,611299
PHN	5	1,886761	6,094283	9,433552	1,779255	5,717209	8,979681
	50	0,760271	1,307615	1,61116	0,330476	0,890505	1,206793
	500	0,604962	0,659579	0,689579	0,171129	0,227125	0,258117
PHNG	5	154,1687	153,4736	152,5092	154,2948	155,1526	154,916
	50	29,53782	29,25064	29,14128	30,39904	30,56931	30,64745
	500	2,994111	2,976816	2,983574	2,577877	2,587711	2,606079
PHPH	5	0,609163	0,669163	0,609163	0,893864	2,813791	5,074013
	50	0,609163	0,669163	0,609163	0,124603	0,509333	0,742187
	500	0,609163	0,669163	0,609163	0,148283	0,188096	0,210288
PHPHN	5	1,652525	5,200651	8,222782	1,253244	5,004556	7,926079
	50	0,68898	1,203741	1,490338	0,258521	0,786527	1,086987
	500	0,597877	0,649195	0,677436	0,163976	0,216687	0,246031
3PH	5	1,585691	3,43456	5,420885	1,164061	3,369869	5,136668
	50	0,685068	0,99186	1,162406	0,252091	0,568891	0,74854
	500	0,597582	0,628175	0,644985	0,163598	0,195138	0,212564

It is key to note that detection and classification of a fault is preceded by classification of the network operating conditions, as shown in Figure 3.22. It is only possible to detect a fault with DG by first detecting the transition to DG. The results from Table 4.7 show the ability to detect and classify the fault type and size. As this is a comparison method, a high distance-value represents a large deviation from normal values and is therefore easier to detect and classify. However, a low distance-value represents a small deviation and, although it can be detected and classified, requires careful consideration. This can be seen from the difference in values from the low-impedance PH-G fault to the high-impedance 3-PH fault. Detecting a fault is a matter of detecting a non-zero distance-value, however classifying the fault is seen to be more difficult due to the similar distance-values between some of the fault types. This is shown with the PH-PH-N and 3-PH faults at the beginning of the feeder. It is further seen that for the fault location, the distance values for the PH-PH fault, with no DG, at the beginning and at the end of the feeder are similar. However, most of the fault types and sizes are distinct and due to this, an estimation of the fault types and sizes can be provided by the procedure. Similar observations are made for Phase B and C and are shown in Appendix A.

Once detection and classification of the fault are completed, location of the fault is the next parameter to be determined. This is completed by using the database of values from Table 4.7, Table and Table . With a knowledge of expected values, it is possible to detect, classify, and locate faults anywhere along the feeder. Figure 4.26 and Figure 4.27 show the network with test faults at two separate locations along the feeder.

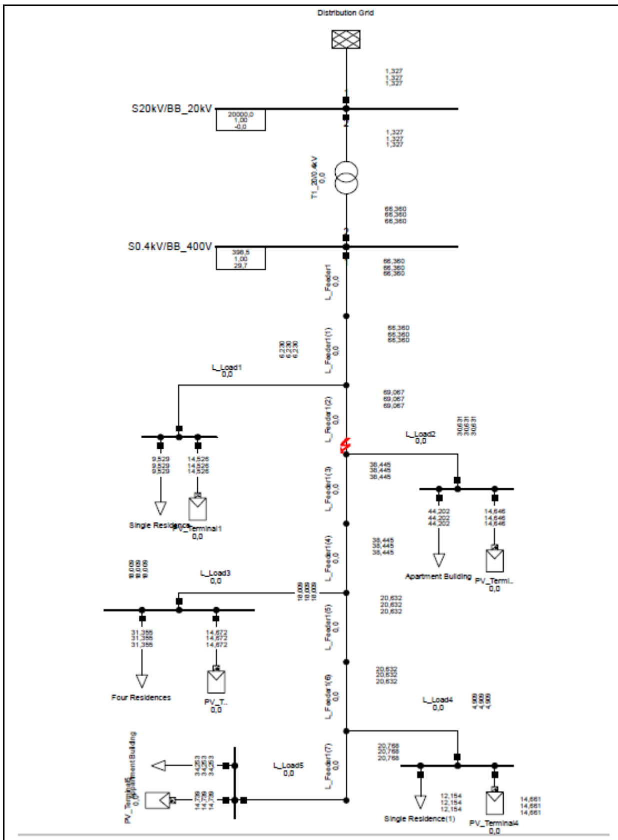

Figure 4.26: CIGRE Benchmark LV Model with Test fault 1

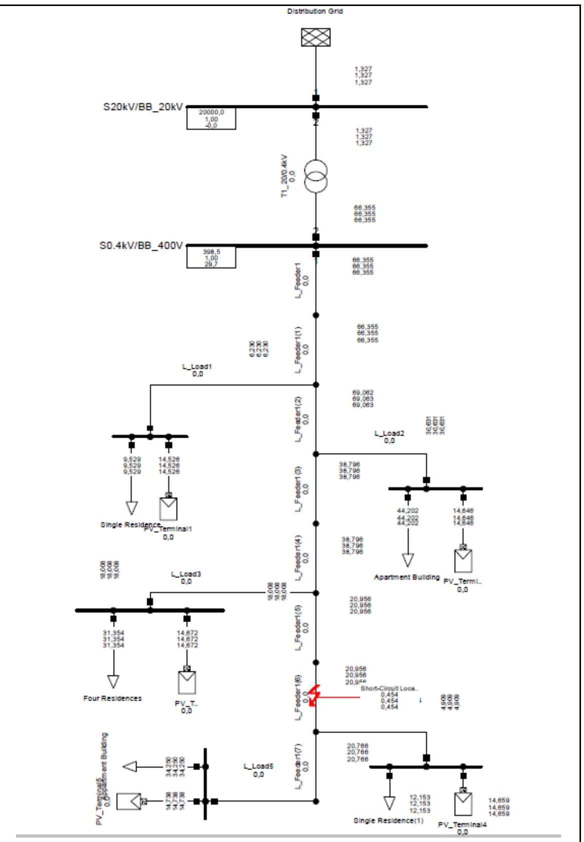

Figure 4.27: CIGRE Benchmark LV Model with Test fault 2

The simulation procedure is followed as previously done and the results for the fault location are tabulated in Table 4.8, Table 4.9 and Table 4.10. The fault location of test fault 1 is at 105 m along the feeder and for test fault 2 at 227.5 m along the feeder. The estimated fault location and the percentage error from the true location is shown below. The percentage errors are highlighted with various shades of colour. The darkest green representing very good accuracy and red representing an inaccurate estimation. Table 4.8 shows the estimation using the Phase A readings.

From Table 4.8, it is seen that the algorithm can locate the fault location with reasonable accuracy. In practice, knowing the side of the feeder along which the fault is present is sufficient. However, the results show fault location estimation of up to within 4% of the true location. It is seen that estimation improves for faults further along the feeder. The estimations marked in red show invalid estimations and this was foreseen from Table 4.7, Table and Table where the distance-values were very similar along the feeder. Table 4.9, shows the estimation using the Phase B readings.

Table 4.8: Estimation of fault location for CIGRE Benchmark LV Model - Phase A

	Fault Size (Ω)	PHASE A - GRID CONNECTED							
		No DG				DG			
		105 m	%Error	227.5 m	%Error	105 m	%Error	227.5 m	%Error
PHG	**5**	78,51936	25,21965	191,1322	15,98583	58,13695	44,63147	182,612	19,73099
	50	98,53194	6,160052	202,3808	11,04141	78,48916	25,24842	218,9562	3,755501
	500	218,4053	108,005	-36,4795	116,0349	-8,03991	107,6571	194,3607	14,56671
PHN	**5**	69,13138	34,16059	199,8443	12,15636	54,13358	48,44421	198,0457	12,94696
	50	80,3951	23,43323	199,0398	12,50996	80,7714	23,07485	198,1732	12,89089
	500	79,56393	24,22483	200,1909	12,00398	79,9961	23,81324	198,6568	12,67835
PHNG	**5**	64,05323	38,99692	184,3193	18,98055	99,41566	5,318416	135,7504	40,32951
	50	92,15874	12,22978	186,3538	18,08623	79,50621	24,2798	216,4991	4,83558
	500	94,73902	9,772362	208,4773	8,361646	-8,62271	108,2121	194,2779	14,60314
PHPH	**5**	3307,662	3050,155	-6577,35	2991,141	69,16055	34,13281	195,7076	13,9747
	50	341,9344	225,6518	-526,363	331,3682	76,97022	26,69503	198,0821	12,93093
	500	-11,8306	111,2673	203,1779	10,69101	79,49277	24,2926	198,5232	12,73706
PHPHN	**5**	62,15384	40,80587	200,0677	12,05816	64,27861	38,78228	197,8108	13,05021
	50	80,13855	23,67758	199,0881	12,48874	80,39714	23,4313	198,1909	12,88312
	500	79,50442	24,28151	200,1644	12,01565	79,78286	24,01633	198,6265	12,69164
3PH	**5**	56,67904	46,01996	199,3448	12,37593	79,67156	24,12232	195,5986	14,0226
	50	79,919	23,88667	199,123	12,47342	80,21725	23,60262	198,1845	12,88595
	500	79,48292	24,30198	199,9849	12,09453	79,72561	24,07085	198,6573	12,67811

Table 4.9: Estimation of fault location for CIGRE Benchmark LV Model – Phase B

	Fault Size (Ω)	PHASE B – GRID CONNECTED							
		No DG				DG			
		105 m	%Error	227.5 m	%Error	105 m	%Error	227.5 m	%Error
PHG	**5**	77,26381	26,41541	191,3986	15,86876	68,84975	34,42881	187,718	17,48658
	50	13,17882	87,44874	386,5661	69,91917	69,29612	34,00369	205,4729	9,68222
	500	-103,762	198,8213	-85,6949	137,6681	80,2991	23,52467	207,8299	8,646178
PHN	**5**	23,31445	77,79576	170,5445	25,03539	87,04072	17,10408	192,3415	15,45427
	50	79,71795	24,07815	206,5461	9,210503	195,2681	85,96959	195,6415	14,00372
	500	79,41519	24,36648	201,1937	11,5632	79,73473	24,06216	200,3215	11,94658
PHNG	**5**	75,01712	28,55513	190,6682	16,1898	8,991967	91,43622	182,1562	19,93132
	50	106,3029	1,24087	187,092	17,76178	69,98922	33,3436	198,0867	12,92893
	500	83,04781	20,90685	191,1399	15,98246	80,36413	23,46274	207,8375	8,642871
PHPH	**5**	275,3694	162,2566	404,6741	77,87872	70,87925	32,49595	198,2663	12,84997
	50	247,3887	135,6083	464,9102	104,3561	80,69747	23,14527	209,898	7,737145
	500	179,3158	70,77694	387,5755	70,36286	80,02738	23,78345	198,5542	12,72344
PHPHN	**5**	65,45703	37,65998	199,1467	12,46299	55,35428	47,28164	196,7504	13,51631
	50	80,24058	23,5804	199,1241	12,47294	80,67562	23,16607	198,2054	12,87676
	500	79,54413	24,24369	200,0767	12,0542	79,98141	23,82723	198,7286	12,64675
3PH	**5**	56,67895	46,02005	199,3448	12,37593	79,67153	24,12235	195,5986	14,0226
	50	79,91902	23,88665	199,123	12,47342	80,21726	23,60261	198,1845	12,88595
	500	79,48295	24,30195	199,985	12,09452	79,72564	24,07081	198,6573	12,67811

It is seen again that reasonable estimation accuracies are obtained and as expected, estimations from Phase B show similar results to estimations from Phase A. This is due to the CIGRE Benchmark LV Model being balanced and each phase reading only having minimal differences. Table 4.10 shows the estimation using the Phase C readings.

Table 4.10: Estimation of fault location for CIGRE Benchmark LV Model – Phase C

	Fault Size (Ω)	PHASE C – GRID CONNECTED							
		No DG				DG			
		105m	%Error	227.5m	%Error	105m	%Error	227.5m	%Error
PHG	5	81,65569	22,23268	192,5591	15,35863	81,82209	22,0742	191,7843	15,6992
	50	77,33431	26,34828	173,5832	23,6997	89,30712	14,9456	193,4669	14,95962
	500	6,574619	93,73846	57,45574	74,74473	87,89639	16,28915	193,6521	14,87821
PHN	5	81,59978	22,28592	192,4628	15,40095	83,01042	20,94246	197,2475	13,29779
	50	78,26797	25,45907	201,6429	11,36577	75,05388	28,52012	200,838	11,71954
	500	79,32237	24,45488	201,3565	11,49165	80,2266	23,59371	200,033	12,07339
PHNG	5	82,5956	21,33753	193,4682	14,95903	81,79355	22,10138	190,8829	16,09543
	50	88,48578	15,72783	197,2553	13,29437	89,61918	14,6484	194,2732	14,60519
	500	86,36849	17,74429	195,7061	13,97532	87,89098	16,29431	193,6429	14,88224
PHPH	5	-86,5828	182,4598	-95,6849	142,0593	76,67951	26,97189	201,3834	11,47983
	50	-100,659	195,8661	-187,38	182,3648	4353,217	4045,921	5459,625	2299,835
	500	-148,712	241,6303	-253,427	211,3967	76,82963	26,82893	201,5702	11,39772
PHPHN	5	112,1085	6,770021	187,2662	17,68517	90,09972	14,19074	184,3663	18,95985
	50	78,68563	25,0613	211,7274	6,933004	0,720255	99,31404	197,1368	13,34648
	500	79,3392	24,43885	201,3012	11,51596	79,56078	24,22783	200,5593	11,84207
3PH	5	56,67896	46,02004	199,3448	12,37593	79,67154	24,12234	195,5986	14,0226
	50	79,91901	23,88665	199,123	12,47342	80,21726	23,60261	198,1845	12,88595
	500	79,48296	24,30194	199,9849	12,09454	79,72563	24,07083	198,6573	12,6781

Similar to the previous results, the inaccurate fault location estimations are the same and the accuracy for the valid estimations is similar. The advantage of using a comparison method for fault location with three different phases is the ability to compare estimations from each phase to reach the correct estimation. However, this advantage is negated with a balanced network as the phase readings are the same therefore the fault location estimations are similar. This limitation is explored with the next section where the network is unbalanced.

4.2.2 Modified Network Model

4.2.2.1 Grid-connected mode

The CIGRE Benchmark LV Model was modified into the network shown in Figure 4.28 according to the procedure detailed in Section 3.2.2.5. The feeder feeds 10 single-phase consumers with an alternating phase allocation beginning with phase A.

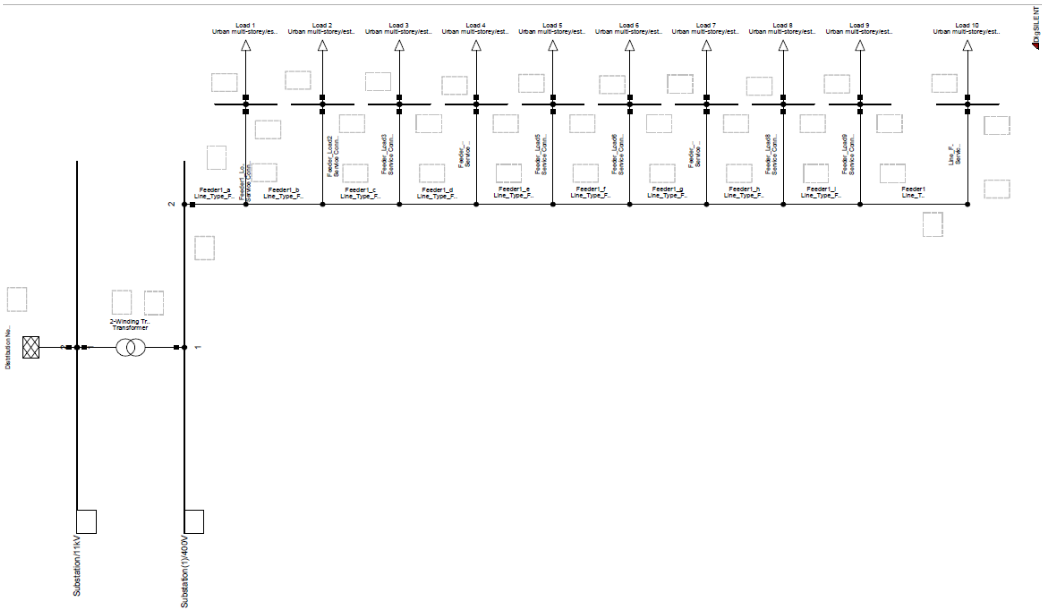

Figure 4.28: Modified Network

The load type is changed as described in Section 3.2 and is done for each of the consumers to simplify the problem. Furthermore, at each load node there is PV connected indicating a 100% PV penetration in the network. Each of the loads and PVs are simulated (as detailed in Section 3.2.2) using IEEE datasets. Fault simulations are static and therefore are conducted at selected times. In this study, noon (12 p.m.) and 6 p.m. are the selected times to show the effects of when there is back-feeding in the network and when there is not. This is shown in Table 4.11 below.

Table 4.11: Load and PV generation scenarios

Time of Day	Load [kW]	PV [kW]
Noon	0,91129	4,59685
6 p.m.	3,29462	1,97632

Figure 4.29 shows the feeder voltage profile with all three phases both with and without DG. Figure 4.30 to Figure 4.32 show the individual phase comparison. These results and the subsequent initial results are simulated using the manufacturer's catalogue feeder impedance model, Table 4.1. Furthermore, the simulations are initially conducted for the noon operating scenario.

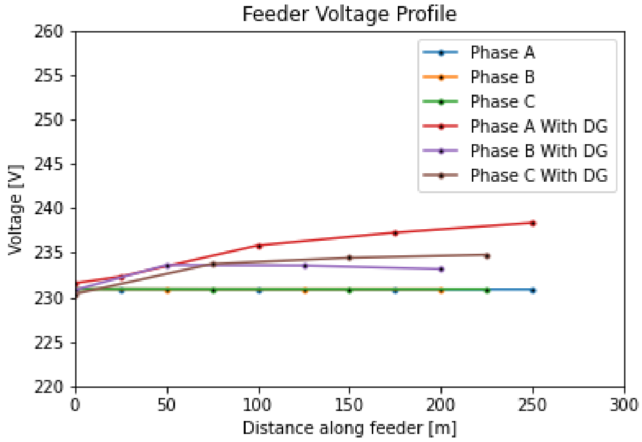

Figure 4.29: Modified Network Combined Phase Comparison at noon

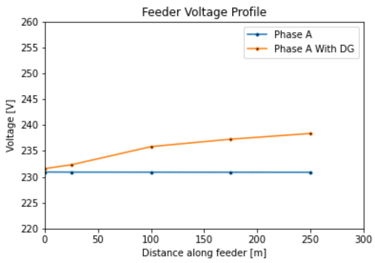

Figure 4.30: Modified Network Phase A Comparison at noon

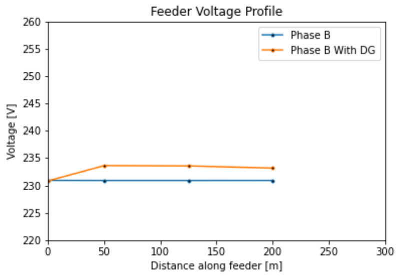

Figure 4.31: Modified Network Phase B Comparison at noon

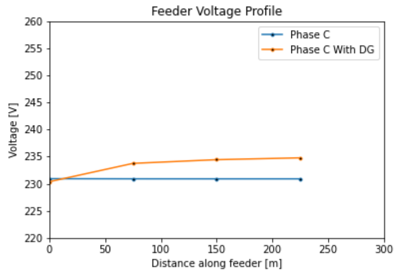

Figure 4.32: Modified Network Phase C Comparison at noon

The x-axis represents the distance along the feeder and the consumer node is indicated on the voltage curves with the associated dot points. It is noticeable that with the presence of DG, the feeder voltage profile improves such that there is a voltage rise along the feeder. The network is unbalanced and this is evident as well in the unbalanced voltage rise in the phases which was not seen in the balanced phases in Figure 4.4. This can be partially attributed to the mutual induction between adjacent conductors in the multi-core feeder. The effect of the induced voltages is seen to be more pronounced in the unbalanced network than when compared with the balanced network.

The locations of the induced faults are shown in Figure 4.33 to Figure 4.35. As with the previous network model, the fault resistance is varied between 5 Ω, 50 Ω and 500 Ω to assess the impact of fault current variation on the voltage profile of the feeder.

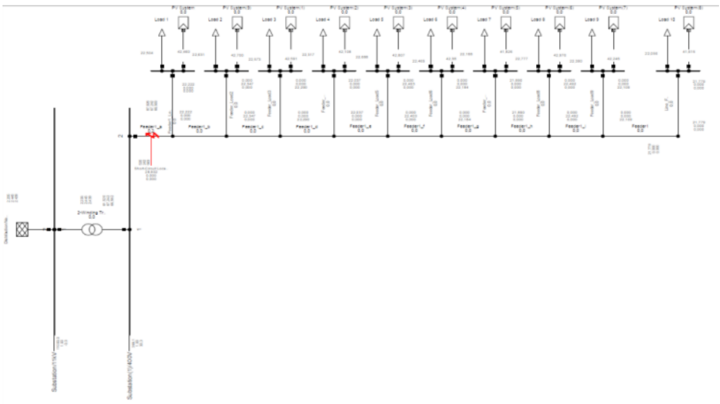

Figure 4.33: Modified network with fault at the beginning of the feeder

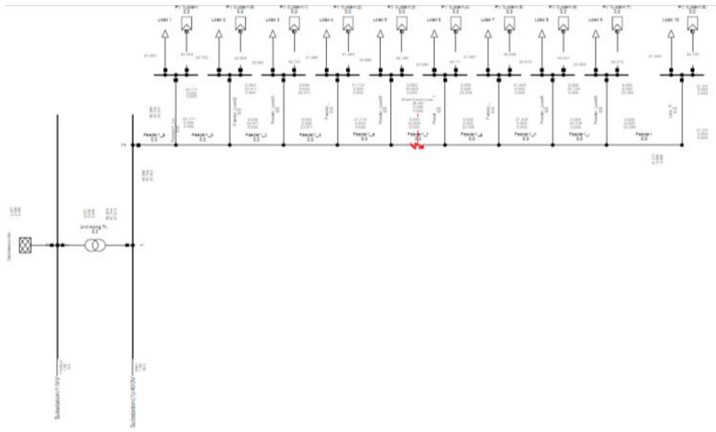

Figure 4.34: Modified network with fault at the middle of the feeder

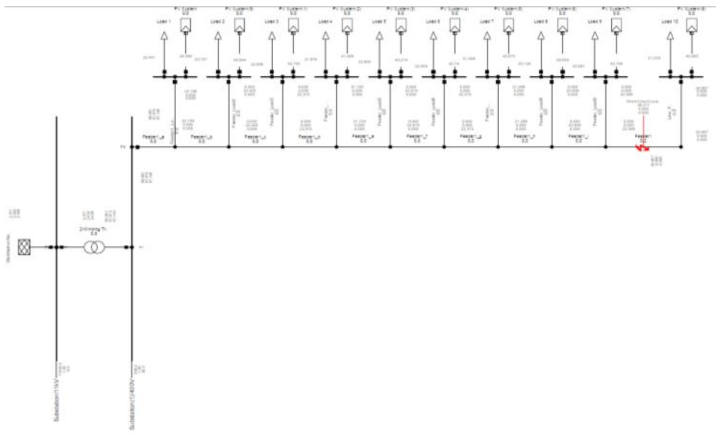

Figure 4.35: Modified network with fault at the end of the feeder

The result of this simulation are shown in Figure 4.36 to Figure 4.44 for the network without the presence of DGs. The graphs show the feeder voltage profile for all three phases both before and during the PH-G fault. This includes the scenarios for the variation in fault current level.

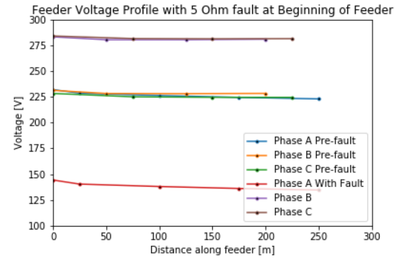

Figure 4.36: Modified network feeder voltage profile with PH-G 5 Ω fault at the beginning of the feeder

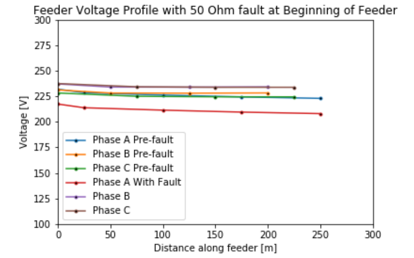

Figure 4.37: Modified network feeder voltage profile with PH-G 50 Ω fault at the beginning of the feeder

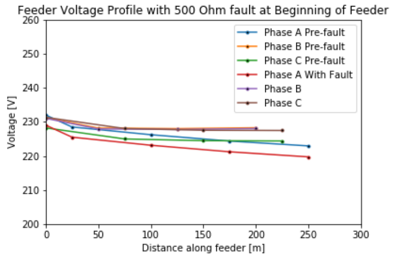

Figure 4.38: Modified network feeder voltage profile with PH-G 500 Ω fault at the beginning of the feeder

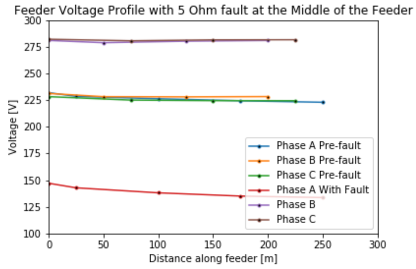

Figure 4.39: Modified network feeder voltage profile with PH-G 5 Ω fault at the middle of the feeder

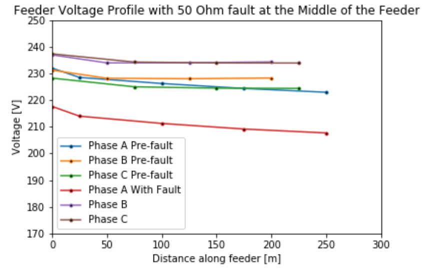

Figure 4.40: Modified network feeder voltage profile with PH-G 50 Ω fault at the middle of the feeder

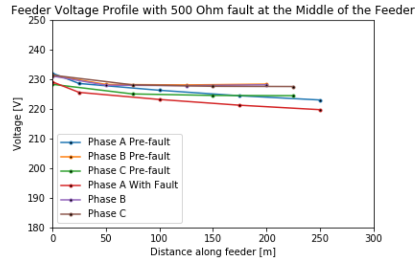

Figure 4.41: Modified network feeder voltage profile with PH-G 500 Ω fault at the middle of the feeder

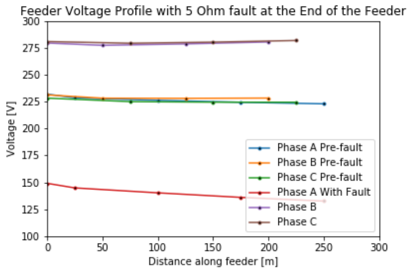

Figure 4.42: Modified network feeder voltage profile with PH-G 5 Ω fault at the end of the feeder

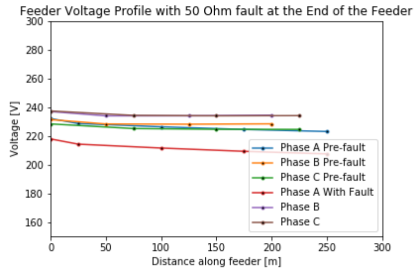

Figure 4.43: Modified network feeder voltage profile with PH-G 50 Ω fault at the end of the feeder

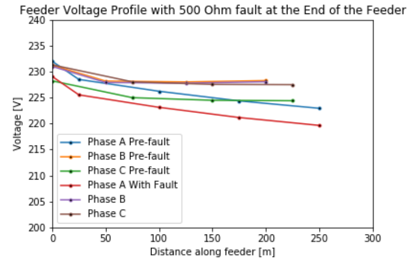

Figure 4.44: Modified network feeder voltage profile with PH-G 500 Ω fault at the end of the feeder

Immediately, it is noticeable that there is a difference in the phase voltage profiles between the unbalanced network and the previously simulated balanced network. The trend of decrease in the voltage of the faulted phase and increase in voltage of the non-faulted phase, that increases largely with decrease in fault resistance, is similar to that found in Section 4.2.1. However, the effect of mutual induction due to the unbalanced network is seen in the curve of the voltage profile.

The difference in the feeder voltage profile due to the variation in fault resistance is only slightly visible in the graphs but is quantifiably visible in Table 4.12 to Table 4.14. This is done for the network operating at noon.

In Table 4.12, the quantitative results of the simulation of the network without DG and with a 5 Ω phase-ground fault are shown. Node 0 is the substation terminal at the beginning of the feeder with Nodes 1-10 being the consumer terminals. As the consumers in this model are single-phase, the nodes have a single voltage reading corresponding to the phase allocation. For the fault at the beginning of the feeder, the fault is between Nodes 0 and 1. For the fault in the middle of the feeder, the fault is between Nodes 5 and 6. For the fault at the end of the feeder, the fault is between Nodes 9 and 10. However, unlike the balanced network, recognising the fault location using the percentage phase voltage differences is more difficult due to the smaller asymmetrical differences. The unbalanced network results in asymmetrical mutual induction between the conductors which results in the more unbalanced phase voltages. This is further evident in the voltages and percentage phase voltage differences for the non-faulted phases, Phase B and C, being unequal where in the previous balanced network they were equal.

Table 4.12: Modified network with No DG & 5 Ω PH-G fault

Node	Beginning of the feeder			Middle of the feeder			End of the feeder		
	Phase A % diff	Phase B % diff	Phase C % diff	Phase A % diff	Phase B % diff	Phase C % diff	Phase A % diff	Phase B % diff	Phase C % diff
0	-37,7627	22,39798	24,37968	-36,5513	21,47977	23,5681	-35,6978	20,82362	23,01356
1	-38,542	n/a	n/a	-37,462	n/a	n/a	-36,5774	n/a	n/a
2	n/a	22,81965	n/a	n/a	22,17398	n/a	n/a	21,48626	n/a
3	n/a	n/a	25,05558	n/a	n/a	24,6942	n/a	n/a	24,08566
4	-38,9585	n/a	n/a	-38,9129	n/a	n/a	-37,9656	n/a	n/a
5	n/a	22,92311	n/a	n/a	22,88311	n/a	n/a	22,16043	n/a
6	n/a	n/a	25,22869	n/a	n/a	25,3596	n/a	n/a	24,81676
7	-39,3064	n/a	n/a	-39,7684	n/a	n/a	-39,3278	n/a	n/a
8	n/a	22,9843	n/a	n/a	23,02785	n/a	n/a	22,81495	n/a
9	n/a	n/a	25,35566	n/a	n/a	25,45464	n/a	n/a	25,54434
10	-39,5795	n/a	n/a	-40,018	n/a	n/a	-40,4885	n/a	n/a

In Table 4.13, the fault resistance is increased to 50 **Ω**. As with the previous simulation, a comparison of the phase terminal voltages due to the location of the fault leaves little quantitative indication.

Table 4.13: Modified network with No DG & 50 Ω PH-G fault

Node	Beginning of the feeder			Middle of the feeder			End of the feeder		
	Phase A % diff	Phase B % diff	Phase C % diff	Phase A % diff	Phase B % diff	Phase C % diff	Phase A % diff	Phase B % diff	Phase C % diff
0	-6,28869	2,527679	4,033731	-6,18665	2,466802	3,983504	-6,1182	2,423604	3,952333
1	-6,42787	n/a	n/a	-6,34774	n/a	n/a	-6,27608	n/a	n/a
2	n/a	2,551516	n/a	n/a	2,524307	n/a	n/a	2,478879	n/a
3	n/a	n/a	4,115159	n/a	n/a	4,118064	n/a	n/a	4,081978
4	-6,53045	n/a	n/a	-6,60984	n/a	n/a	-6,53092	n/a	n/a
5	n/a	2,568468	n/a	n/a	2,61314	n/a	n/a	2,564977	n/a
6	n/a	n/a	4,144539	n/a	n/a	4,204859	n/a	n/a	4,177353
7	-6,61662	n/a	n/a	-6,77459	n/a	n/a	-6,77573	n/a	n/a
8	n/a	2,585621	n/a	n/a	2,640779	n/a	n/a	2,653588	n/a
9	n/a	n/a	4,171603	n/a	n/a	4,228118	n/a	n/a	4,275939
10	-6,68342	n/a	n/a	-6,83832	n/a	n/a	-6,98126	n/a	n/a

In Table 4.14, the fault resistance is increased to 500 **Ω**. The trend of the fault voltage being highly indistinguishable from the pre-fault voltage for low fault current continues.

These quantitative analyses can be done for the various fault types and the trend remains consistent. The simulations are then performed with the presence of DGs, as indicated in Figure 4.33. The results are shown in Figure 4.45 to Figure 4.53.

Table 4.14: Modified network with No DG & 500 Ω PH-G fault

Node	Beginning of the feeder			Middle of the feeder			End of the feeder		
	Phase A % diff	Phase B % diff	Phase C % diff	Phase A % diff	Phase B % diff	Phase C % diff	Phase A % diff	Phase B % diff	Phase C % diff
0	-1,27342	0,08804	1,356387	-1,26405	0,0933	1,352121	-1,2579	0,09701	1,349589
1	-1,31058	n/a	n/a	-1,30355	n/a	n/a	-1,29709	n/a	n/a
2	n/a	0,10996	n/a	n/a	0,11186	n/a	n/a	0,11576	n/a
3	n/a	n/a	1,35537	n/a	n/a	1,356338	n/a	n/a	1,353344
4	-1,36314	n/a	n/a	-1,37298	n/a	n/a	-1,3658	n/a	n/a
5	n/a	0,10911	n/a	n/a	0,1039	n/a	n/a	0,10804	n/a
6	n/a	n/a	1,360272	n/a	n/a	1,366888	n/a	n/a	1,364751
7	-1,40762	n/a	n/a	-1,42578	n/a	n/a	-1,42709	n/a	n/a
8	n/a	0,10307	n/a	n/a	0,09681	n/a	n/a	0,09492	n/a
9	n/a	n/a	1,368025	n/a	n/a	1,374265	n/a	n/a	1,379565
10	-1,44154	n/a	n/a	-1,45938	n/a	n/a	-1,47571	n/a	n/a

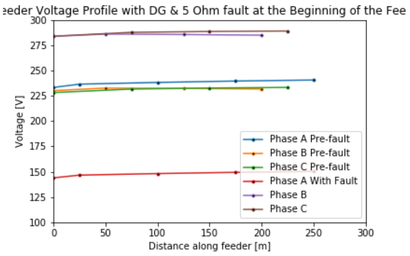

Figure 4.45: Modified network feeder voltage profile with DG & PH-G 5 Ω fault at the beginning of the feeder

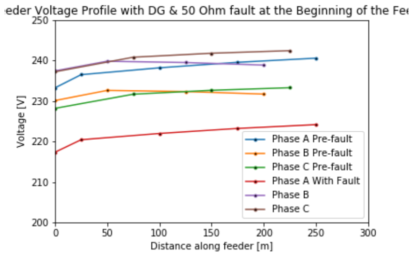

Figure 4.46: Modified network feeder voltage profile with DG & PH-G 50 Ω fault at the beginning of the feeder

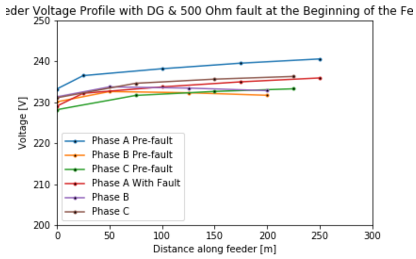

Figure 4.47: Modified network feeder voltage profile with DG & PH-G 500 Ω fault at the beginning of the feeder

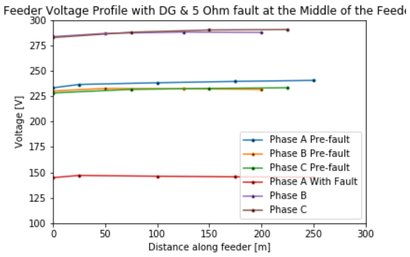

Figure 4.48: Modified network feeder voltage profile with DG & PH-G 5 Ω fault at the middle of the feeder

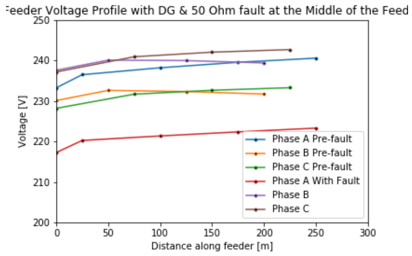

Figure 4.49: Modified network feeder voltage profile with DG & PH-G 50 Ω fault at the middle of the feeder

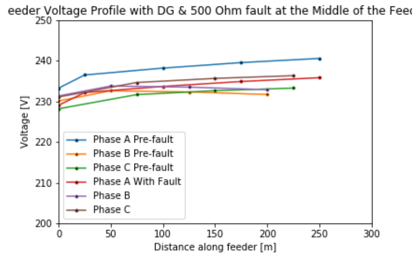

Figure 4.50: Modified network feeder voltage profile with DG & PH-G 500 Ω fault at the middle of the feeder

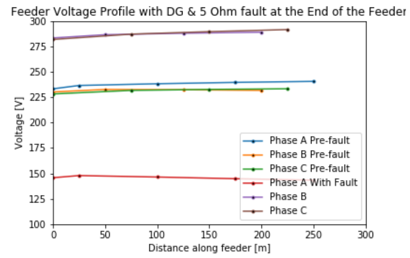

Figure 4.51: Modified network feeder voltage profile with DG & PH-G 5 Ω fault at the end of the feeder

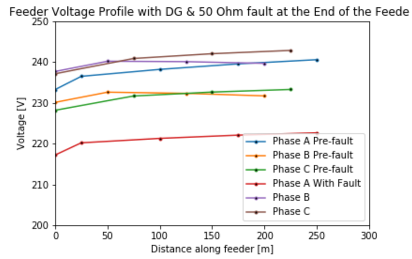

Figure 4.52: Modified network feeder voltage profile with DG & PH-G 50 Ω fault at the end of the feeder

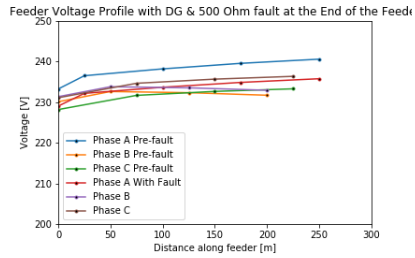

Figure 4.53: Modified network feeder voltage profile with DG & PH-G 500 Ω fault at the end of the feeder

As expected, the voltage on the faulted phase decreases whilst the voltage on the non-faulted phases increases with the presence of the phase-to-ground fault. This difference grows more pronounced the lower the fault resistance is. Although, even with a similar trend to the balanced network simulation, the unbalanced network's faulted-voltage profile deviates more from the pre-fault voltage profile.

The quantitative analysis can be similarly done for when there is DG and the voltage difference trend seen with no DG is continued. A fault is evident as the phase voltage difference is outside of the 10% voltage variation limit. However, the trend exhibited in Table 4.12 to Table 4.14 is continued here where the fault location is indistinguishable from the difference in the percentage phase voltage differences. These observations are repeated for the different fault types.

The simulations were initially performed using the impedance model from the manufacturer's catalogue, Table 4.1. Following this, the simulations were then performed using the analytical model, Section 3.2.3, which comprised the resistive part of the impedance model from the manufacturer's catalogue. Next, the simulations were performed using the FE impedance model, Table 4.2, and with the experimental impedance model,

Table 4.3. Consequently, a comparison of the difference between the consumer terminal voltages found using the catalogue impedance model and the other impedance models is made. This is done to quantify the effect that the impedance modelling method has on the feeder voltage profile and the subsequent fault location algorithm.

Table 4.15 shows the comparison of feeder voltage values between the catalogue data feeder model and the analytical feeder model for Phase A. The percentage differences are calculated using the following formula:

$$\%Diff = \frac{V_{ph-i,model} - V_{ph-i,catalogue\ data\ model}}{V_{ph-i,catalogue\ data\ model}} \times 100 \tag{4.4}$$

The effect of considering the resistive part of the impedance model solely is shown. It is noticeable that the percentage differences are greater with the lower voltages when there is no DG and further along the feeder. Contrastingly, the percentage voltage difference is lower when there is DG and closer to the beginning of the feeder. Although the percentage differences are all less than 1%, a comparison of the change of the percentage differences from normal operation to faulted operation show that the differences increase with the presence of the 5 Ω fault. However, the percentage differences decrease as the fault resistance is increased for both the cases of when there is DG and when not.

Table 4.15: Comparison of feeder voltage values between catalogue impedance model and analytical impedance model for Phase A

Node	%diff No DG	%diff No DG & PH-G fault at the beginning of the feeder			%diff DG	%diff With DG & PH-G fault at the beginning of the feeder		
		5Ω	50Ω	500Ω		5Ω	50Ω	500Ω
0	0,018963	0,034956	0,00554	0,002459	0,04692	0,01527	0,002568	0,002615
1	0,040739	0,115869	0,071073	0,064934	0,059296	0,024875	0,00281	0,007326
2	n/a	n/a	n/a	n/a	n/a	n/a	n/a	n/a
3	n/a	n/a	n/a	n/a	n/a	n/a	n/a	n/a
4	0,146239	0,297378	0,192112	0,180046	0,035415	0,080131	0,031681	0,025001
5	n/a	n/a	n/a	n/a	n/a	n/a	n/a	n/a
6	n/a	n/a	n/a	n/a	n/a	n/a	n/a	n/a
7	0,253209	0,483812	0,314205	0,295885	0,044057	0,079162	0,030667	0,023879
8	n/a	n/a	n/a	n/a	n/a	n/a	n/a	n/a
9	n/a	n/a	n/a	n/a	n/a	n/a	n/a	n/a

10	0,360982	0,672608	0,43613	0,41134	0,083734	0,024624	0,004871	0,009835

The quantitative observations are repeated for Phase B and Phase C. The trends observed in Phase A are continued for the other phases. However, for Phase B the percentage phase voltage differences are slightly higher than those calculated for Phase A as the voltage profile is now generally lower than that of Phase A.

Table 4.16 shows the comparison of feeder voltage values between the catalogue impedance model and the FE impedance model for Phase A. It is seen that the FE impedance model provides a good approximation of the catalogue impedance model as the percentage voltage differences are all very low, less than 0.5%. Furthermore, the trends noted for Table 4.15 are applicable here.

Table 4.16: Comparison of feeder voltage values between catalogue impedance model and finite element impedance model for Phase A

Node	%diff No DG	%diff No DG & PH-G fault at the beginning of the feeder			%diff DG (10kW)	%diff With DG & PH-G fault at the beginning of the feeder		
		5Ω	50Ω	500Ω		5Ω	50Ω	500Ω
0	0,015157	0,008404	0,000421	5,85E-05	0,026456	5,1E-05	0,000448	0,000148
1	6,89E-05	0,027372	0,017543	0,016237	0,040511	0,009743	0,012304	0,012899
2	n/a	n/a	n/a	n/a	n/a	n/a	n/a	n/a
3	n/a	n/a	n/a	n/a	n/a	n/a	n/a	n/a
4	0,031712	0,081505	0,053378	0,050271	0,064288	0,042156	0,034581	0,034157
5	n/a	n/a	n/a	n/a	n/a	n/a	n/a	n/a
6	n/a	n/a	n/a	n/a	n/a	n/a	n/a	n/a
7	0,058681	0,12851	0,084047	0,079349	0,083819	0,068991	0,052902	0,05162
8	n/a	n/a	n/a	n/a	n/a	n/a	n/a	n/a
9	n/a	n/a	n/a	n/a	n/a	n/a	n/a	n/a
10	0,080689	0,167385	0,109067	0,103032	0,099182	0,090675	0,067525	0,06553

Similar observations are made for Phase B and Phase C. Table 4.17 shows the comparison of feeder voltage values between the catalogue impedance model and the experimental impedance model for Phase A. These differences are seen to be of very low value, less than 1%, which is consistent with the previous simulations undertaken. As previously discussed in Section 3.2.3, the experimental impedance model used is with both the neutral and armouring earthed. The observations made for Table 4.15 are similarly applicable here.

Table 4.17: Comparison of feeder voltage values between catalogue impedance model and experimental impedance model for Phase A

Node	%diff No DG	%diff No DG & PH-G fault at the beginning of the feeder			%diff DG (10kW)	%diff With DG & PH-G fault at the beginning of the feeder		
		5Ω	50Ω	500Ω		5Ω	50Ω	500Ω
0	0,02154051	0,03324899	1,0866E-05	0,00168833	0,0492236	0,01346091	0,00205392	0,00186073
1	0,02944626	0,10330982	0,06107072	0,05518417	0,07016363	0,01344591	0,01226265	0,01658551
2	n/a	n/a	n/a	n/a	n/a	n/a	n/a	n/a
3	n/a	n/a	n/a	n/a	n/a	n/a	n/a	n/a
4	0,12610784	0,26901548	0,17182707	0,16054652	0,06986037	0,03173421	0,00300009	0,00828545
5	n/a	n/a	n/a	n/a	n/a	n/a	n/a	n/a
6	n/a	n/a	n/a	n/a	n/a	n/a	n/a	n/a
7	0,22825545	0,44639918	0,28816169	0,27093709	0,09758864	0,00120926	0,02440259	0,02884373
8	n/a	n/a	n/a	n/a	n/a	n/a	n/a	n/a
9	n/a	n/a	n/a	n/a	n/a	n/a	n/a	n/a
10	0,33542837	0,63354484	0,40913016	0,38549367	0,15221331	0,07630625	0,07586031	0,07773619

Similar observations were made for Phase B and Phase C.

Following the analysis of the voltage profile and the arising differences between the impedance models, next to be determined was the ability of the algorithm to detect, classify and locate faults as well as the impact the cable impedance modelling technique used has on this. This was done for all the fault types and when the fault is at the beginning, middle and end of the feeder. Table 4.18, Table and Table show the Euclidean distances with the catalogue data impedance model at noon for Phase A, Phase B and Phase C, respectively. Table 4.19, Table , Table show the same for the 6 p.m. operating scenario.

Table 4.18: DTW Euclidean distances for the modified network (catalogue impedance) at noon - Phase A

		PHASE A - GRID CONNECTED					
	Fault Size (Ω)	No DG			DG		
		B	M	E	B	M	E
No fault	---	0	0	0	11,11232	11,11232	11,11232
PHG	5	194,0702	195,914	195,1683	196,0647	200,2202	200,8726
	50	29,3418	30,10616	30,37656	31,1619	32,33129	32,86519
	500	3,092626	3,181497	3,216774	3,913322	4,013073	4,094066
PHN	5	1,406923	12,12448	16,7515	2,864982	15,51684	20,76257
	50	0,127876	1,244042	1,769926	1,76305	2,72181	3,439238
	500	0,011285	0,11546	0,170883	1,68441	1,73419	1,76608
PHNG	5	141,4702	145,0222	145,2583	143,4469	148,9664	150,2629
	50	27,77694	28,54992	28,82637	29,59626	30,74476	31,25143
	500	3,074373	3,163277	3,198587	3,899864	3,997601	4,076282
PHPH	5	1,509926	1,773355	2,933275	143,4469	148,9664	150,2629
	50	0,146535	0,178242	0,296388	29,59626	30,74476	31,25143
	500	0,013488	0,015604	0,027232	3,899864	3,997601	4,076282
PHPHN	5	0,406958	6,44644	8,907086	1,81918	7,939895	11,83293
	50	0,036289	0,682412	0,992115	1,684354	2,139149	2,510425
	500	0,004154	0,06174	0,095001	1,677132	1,70467	1,721912
3PH	5	0,250852	2,325499	3,292481	1,823692	4,262953	7,058276
	50	0,020164	0,221738	0,321297	1,688499	2,021258	2,464447
	500	0,002762	0,018959	0,029238	1,677577	1,70801	1,744551

From Table 4.18, it can be seen that the algorithm is capable of distinctly distinguishing the fault type and resistance. Like the procedure described with the CIGRE Benchmark LV Model, the algorithm first classifies the current operating scenario (whether DG is present or not) and consequently can detect the fault for the appropriate operating scenario. However, from the results it appears that the values for the PH-N fault are similar to those of the PH-PH fault. This possible conflation is negated by the analyses of the results from Table and Table . Having readings from the other two phases allows for cross-analysis which increases the accuracy of the algorithm. Analysis of the results for the different impedance models show similar detection ability as the catalogue impedance model.

Table 4.19 shows the Euclidean distance for the 6 p.m. scenario.

Table 4.19: DTW Euclidean distances for the modified network (catalogue impedance) at 6pm - Phase A

		PHASE A - GRID CONNECTED					
	Fault Size (Ω)	No DG			DG		
		B	M	E	B	M	E
No fault	---	0	0	0	4,467261	4,467261	4,467261
PHG	5	194,0702	195,914	195,1683	194,4797	197,3298	197,1989
	50	29,3418	30,10616	30,37656	29,6723	30,61063	30,99493
	500	3,092626	3,181497	3,216774	2,796601	2,883176	2,957435
PHN	5	1,406923	12,12448	16,7515	1,358337	13,14467	18,03985
	50	0,127876	1,244042	1,769926	0,460246	1,419616	2,166604
	500	0,011285	0,11546	0,170883	0,332416	0,440413	0,489521
PHNG	5	141,4702	145,0222	145,2583	141,8697	146,2659	146,9625
	50	27,77694	28,54992	28,82637	28,107	29,0406	29,41615
	500	3,074373	3,163277	3,198587	2,781282	2,866389	2,939318
PHPH	5	1,509926	1,773355	2,933275	1,115191	1,809983	3,176106
	50	0,146535	0,178242	0,296388	0,169527	0,426341	0,548058
	500	0,013488	0,015604	0,027232	0,303405	0,326444	0,336396
PHPHN	5	0,406958	6,44644	8,907086	0,639119	7,121855	9,762825
	50	0,036289	0,682412	0,992115	0,341182	0,830544	1,235805
	500	0,004154	0,06174	0,095001	0,320636	0,383762	0,412404
3PH	5	0,250852	2,325499	3,292481	0,57279	2,573717	4,664482
	50	0,020164	0,221738	0,321297	0,3423	0,61877	0,80322
	500	0,002762	0,018959	0,029238	0,320905	0,355037	0,383581

Regardless of a load or PV generation change, the algorithm retains the ability to detect and classify the fault type and resistance. However, as at 6 p.m. the PV generation is much lower, the Euclidean distance calculated shows a much lower distinction from normal operation. This indicates that careful consideration of the range of acceptable distance values is required to maintain accuracy. Analysis of the results for the different impedance models shows similar detection ability as the catalogue data impedance model.

Figure 4.54 and Figure 4.55 show the fault locations for evaluating the accuracy of the fault location estimation. Test fault 1 is 62.5 m along the feeder and test fault 2 is 187.5 m along the feeder. Their locations are chosen to compare for when the fault is further up the feeder and when it is further down the feeder.

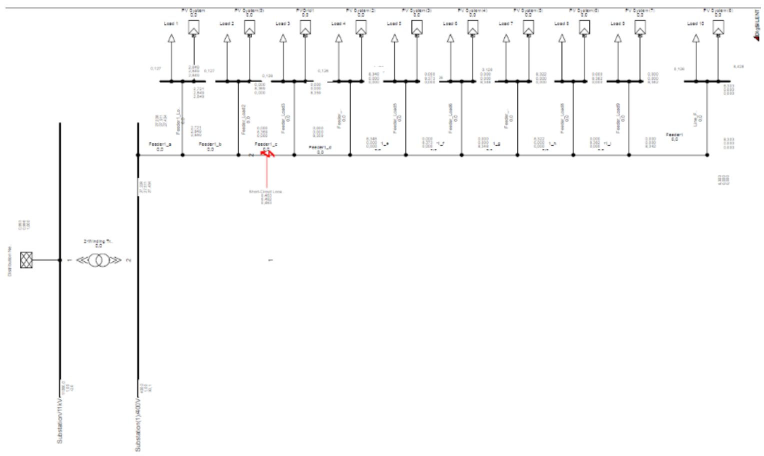

Figure 4.54: Modified network with test fault 1

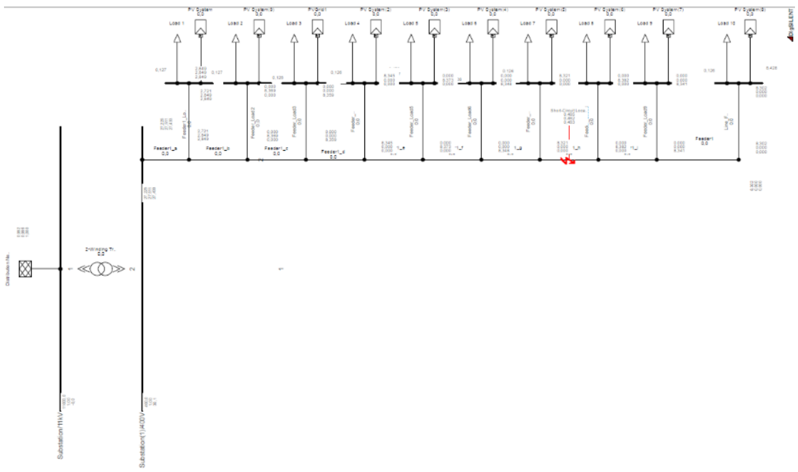

Figure 4.55: Modified network with test fault 2

The results of the estimation for the fault location are shown below in Tables 4.20 – 4.22. Table 4.20 show the results from using the Phase A readings at noon.

Table 4.20 shows that the algorithm can locate a fault with extremely good accuracy. However, the faults highlighted in red are not able to be detected by the results from Phase A. This inaccuracy is improved by cross-analysing with the results below.

Table 4.21 show the results from using the Phase B readings at noon.

Table 4.21 similarly shows that the algorithm can locate a fault with extremely good accuracy. The fault location estimation from Phase A proved inaccurate for the PH-PH fault with no DG. This, however, is accurately estimated by the results from Phase B. Where the results from Phase B are inaccurate, they are accurate in the results from Phase A. The consistently wrong estimations are for the PH-PH fault with DG. This is now compared with the results from Phase C.

Table 4.22 show the results from using the Phase C readings at noon.

Table 4.20: Estimation of fault location for modified network (catalogue impedance) at noon - Phase A

		PHASE A - GRID CONNECTED							
	Fault Size (Ω)	No DG				DG			
		62.5 m	%Error	187.5 m	%Error	62.5 m	%Error	187.5 m	%Error
PHG	**5**	74,07444	18,51911	135,9726	27,48128	59,2899	5,136159	240,3502	28,18675
	50	58,71952	6,048768	191,8538	2,322048	54,06144	13,5017	188,1564	0,350092
	500	57,8431	7,451035	188,6233	0,599107	45,77551	26,75918	180,3312	3,823383
PHN	**5**	56,40245	9,756085	187,5957	0,051052	41,56571	33,49487	188,0643	0,300938
	50	55,09847	11,84244	186,0945	0,749619	47,9759	23,23856	176,9398	5,632116
	500	49,52199	20,76482	185,6421	0,990907	61,86725	1,012393	165,6056	11,67703
PHNG	**5**	64,62758	3,404136	320,3214	70,83808	59,51165	4,781361	209,9274	11,9613
	50	58,63493	6,184116	191,5548	2,162551	54,84838	12,24259	188,2658	0,408446
	500	57,83736	7,460218	188,6175	0,595992	46,28078	25,95075	180,1821	3,902898
PHPH	**5**	-280,791	549,2652	184,6904	1,498436	-3216,85	5246,96	-11094,4	6016,993
	50	-234,784	475,6538	184,074	1,827221	-3044,33	4970,922	-5606,88	3090,337
	500	-243,208	489,1333	178,5029	4,79848	-2850,52	4660,828	-2825	1606,668
PHPHN	**5**	56,61828	9,410749	188,7262	0,653981	44,60313	28,63499	198,2544	5,735682
	50	54,117	13,4128	186,1366	0,727151	49,15196	21,35687	174,0782	7,158281
	500	45,69086	26,89463	185,1459	1,255518	63,53921	1,662738	163,7662	12,65805
3PH	**5**	55,34516	11,44774	186,1961	0,695391	44,54896	28,72166	174,6298	6,864099
	50	52,77419	15,56129	185,8812	0,863343	26,3766	57,79744	177,5866	5,287151
	500	57,22745	8,436075	182,2672	2,790818	27,93447	55,30485	177,4329	5,369126

Table 4.21: Estimation of fault location for modified network (catalogue impedance) at noon - Phase B

		PHASE B - GRID CONNECTED							
	Fault Size (Ω)	No DG				DG			
		62.5 m	%Error	187.5 m	%Error	62.5 m	%Error	187.5 m	%Error
PHG	**5**	153,0543	144,8869	160,5703	14,36252	63,02779	0,844466	-385,669	305,6899
	50	64,3241	2,918563	234,5516	25,09419	55,00293	11,99532	185,9819	0,809655
	500	62,49297	0,011254	207,1021	10,45443	54,30869	13,1061	183,9801	1,877254
PHN	**5**	55,13388	11,78579	208,8973	11,41189	57,05122	8,71805	204,3293	8,975604
	50	53,92932	13,7131	204,4083	9,017743	60,24615	3,606159	199,8771	6,60111
	500	55,3862	11,38208	204,0202	8,810747	57,19164	8,493378	199,6536	6,481905
PHNG	**5**	79,81568	27,70508	145,7663	22,258	64,03915	2,462635	402,5607	114,699
	50	64,13426	2,61482	230,5985	22,98584	-849,122	1458,596	188,376	0,467225
	500	62,47436	0,041025	206,9709	10,38449	55,70647	10,86965	185,6409	0,991512
PHPH	**5**	59,00279	5,595531	205,8475	9,785332	-3175,12	5180,19	-64144,1	34310,18
	50	58,55174	6,317222	204,125	8,866689	-2930,36	4788,578	-6309,53	3465,081
	500	58,50741	6,388136	203,9609	8,779121	-2966,95	4847,118	-5855,56	3222,967
PHPHN	**5**	60,48668	3,221308	209,2846	11,61844	61,31734	1,892253	213,7868	14,01964
	50	58,71954	6,048739	204,4374	9,033277	73,05299	16,88478	207,4075	10,61735
	500	58,53391	6,345747	203,9511	8,773919	80,24562	28,39299	105,197	43,89491
3PH	**5**	58,61378	6,217954	203,9453	8,770834	65,36212	4,579393	182,2403	2,805182
	50	58,33945	6,656875	202,727	8,12108	15,40972	75,34445	167,0625	10,90001
	500	58,29433	6,729079	202,4648	7,981204	14,41797	76,93125	167,0656	10,89836

Table 4.22: Estimation of fault location for modified network (catalogue impedance) at noon - Phase C

		PHASE C - GRID CONNECTED							
	Fault Size (Ω)	No DG				DG			
		62.5 m	%Error	187.5 m	%Error	62.5 m	%Error	187.5 m	%Error
PHG	5	82,76758	32,42812	158,2374	15,60674	66,03205	5,651283	91,2009	51,35952
	50	60,94882	2,481892	191,3623	2,059888	57,40511	8,151827	201,5595	7,498392
	500	59,9024	4,156167	187,4943	0,00304	60,8191	2,689433	198,2948	5,757235
PHN	5	58,42112	6,526204	186,0559	0,770164	59,14509	5,36785	187,616	0,061868
	50	57,88308	7,387078	184,9359	1,367541	57,49591	8,00655	185,6683	0,976895
	500	49,2464	21,20577	184,8344	1,421644	58,99651	5,605584	185,3454	1,149146
PHNG	5	69,1286	10,60576	107,6962	42,56203	63,65975	1,855592	332,185	77,16532
	50	60,86481	2,616303	191,0551	1,89606	56,62793	9,395305	197,6433	5,409786
	500	59,90392	4,153731	187,5172	0,009182	60,57018	3,087706	194,2532	3,601716
PHPH	5	50,80709	18,70865	173,1306	7,663658	-3624,43	5899,094	-54194,3	29003,65
	50	49,05306	21,5151	172,392	8,05762	-3962,74	6440,381	-9633,98	5238,123
	500	97,73741	56,37985	159,6728	14,84119	-3869,17	6290,672	-8885,56	4838,966
PHPHN	5	60,31896	3,489657	187,9241	0,22621	61,21648	2,053639	189,6868	1,166269
	50	58,20892	6,865723	185,0518	1,305705	57,11962	8,608602	186,1908	0,698259
	500	53,4635	14,4584	184,7687	1,456712	58,19981	6,880298	185,4272	1,105497
3PH	5	58,07714	7,076582	185,0999	1,280069	-43,1334	169,0135	178,9213	4,575326
	50	57,32657	8,277493	185,0356	1,314371	76,67959	22,68735	130,314	30,49919
	500	55,47005	11,24792	184,7027	1,491899	72,07917	15,32667	127,1352	32,19453

Table 4.22 similarly shows that the algorithm can locate a fault with extremely good accuracy. The inaccuracies in the fault location estimation from this fault are resolved with cross-analysis with the preceding results. However, fault location estimation for the PH-PH fault with DG is inaccurate for all phases. This is true for both locations and all the fault resistances. This inaccuracy is however not seen with the results from the other impedance models, where cross-analysis resolves all the inaccuracies. This is illustrated in Table 4.23 below. The average accuracy percentage is shown for the different impedance models and all the phases. The number of invalid estimations of the fault location is also shown.

The accuracy of the algorithm is maintained regardless of the impedance modelling technique used. The number of invalid estimations is low compared to the number of estimations made in total. Cross-analysis of the three phases shows the ability to improve invalid estimations.

Table 4.24 show the results from using the Phase A readings at 6 p.m.

With a change in the load and PV generation, it can be seen from Table 4.24 that the algorithm maintains its ability to locate a fault accurately. The inaccuracies in these results are cross analysed with results from the phases below.

Table 4.25 show the results from using the Phase B readings at 6 p.m.

Table 4.23: Average accuracy for Modified Network (Grid-connected) at noon

		Phase A	Phase B	Phase C
Catalogue impedance model	Average % error	9.86	9.29	7.83
	Invalid estimations out of 72	12	12	10
Analytical impedance model	Average % error	10.52	8.57	8.50
	Invalid estimations out of 72	6	7	6
F.E. impedance model	Average % error	9.86	9.49	7.72
	Invalid estimations out of 72	6	4	5
Experiment impedance model	Average % error	10.25	8.30	7.40
	Invalid estimations out of 72	5	6	3

Table 4.24: Estimation of fault location for modified network (catalogue impedance) at 6pm - Phase A

		PHASE A - GRID CONNECTED							
	Fault Size (Ω)	**No DG**				**DG**			
		62.5 m	**%Error**	**187.5 m**	**%Error**	**62.5 m**	**%Error**	**187.5 m**	**%Error**
PHG	**5**	74,07444	18,51911	135,9726	27,48128	64,60745	3,371921	-92,5435	149,3565
	50	58,71952	6,048768	191,8538	2,322048	56,2074	10,06816	189,6161	1,128606
	500	57,8431	7,451035	188,6233	0,599107	50,56234	19,10025	173,4839	7,475253
PHN	**5**	56,40245	9,756085	187,5957	0,051052	56,15811	10,14702	187,777	0,147727
	50	55,09847	11,84244	186,0945	0,749619	46,32926	25,87319	179,2787	4,384667
	500	49,52199	20,76482	185,6421	0,990907	55,53106	11,15031	186,8666	0,337839
PHNG	**5**	64,62758	3,404136	320,3214	70,83808	61,82297	1,083253	231,0407	23,22172
	50	58,63493	6,184116	191,5548	2,162551	56,62559	9,39906	189,6264	1,134069
	500	57,83736	7,460218	188,6175	0,595992	50,88491	18,58414	173,2378	7,606503
PHPH	**5**	-280,791	549,2652	184,6904	1,498436	-51,5236	182,4378	189,3551	0,989407
	50	-234,784	475,6538	184,074	1,827221	54,99317	12,01092	186,0159	0,791538
	500	-243,208	489,1333	178,5029	4,79848	56,49876	9,601987	187,3394	0,085653
PHPHN	**5**	56,61828	9,410749	188,7262	0,653981	42,30819	32,30689	188,6929	0,636208
	50	54,117	13,4128	186,1366	0,727151	67,30364	7,685818	174,1147	7,138809
	500	45,69086	26,89463	185,1459	1,255518	55,65041	10,95935	186,9073	0,316121
3PH	**5**	55,34516	11,44774	186,1961	0,695391	39,42006	36,9279	183,6816	2,036487
	50	52,77419	15,56129	185,8812	0,863343	46,97492	24,84013	169,013	9,859712
	500	57,22745	8,436075	182,2672	2,790818	38,25335	38,79464	182,5909	2,618191

Table 4.25 similarly shows that the algorithm can locate a fault with extremely good accuracy. Where the estimations are inaccurate, they are accurate in the estimations from Phase A. Also, where the estimations in Phase A were inaccurate, they are accurate in the estimations in Phase B. This cross analysis between phase readings increases the accuracy of the algorithm.

Table 4.26 show the results from using the Phase C readings at 6 p.m.

Table 4.25: Estimation of fault location for modified network (catalogue impedance) at 6pm - Phase B

		PHASE B - GRID CONNECTED							
	Fault Size (Ω)	No DG				DG			
		62.5 m	%Error	187.5 m	%Error	62.5 m	%Error	187.5 m	%Error
PHG	5	153,0543	144,8869	160,5703	14,36252	77,12017	23,39227	147,4895	21,33896
	50	64,3241	2,918563	234,5516	25,09419	58,6364	6,181757	194,3492	3,652932
	500	62,49297	0,011254	207,1021	10,45443	57,60896	7,825665	189,6624	1,153299
PHN	5	55,13388	11,78579	208,8973	11,41189	55,92135	10,52583	206,7699	10,27727
	50	53,92932	13,7131	204,4083	9,017743	54,00711	13,58863	202,4778	7,988134
	500	55,3862	11,38208	204,0202	8,810747	56,80538	9,111395	202,0077	7,737439
PHNG	5	79,81568	27,70508	145,7663	22,258	69,96796	11,94873	111,8417	40,35109
	50	64,13426	2,61482	230,5985	22,98584	59,67229	4,524332	197,2446	5,197124
	500	62,47436	0,041025	206,9709	10,38449	58,53078	6,350758	191,4729	2,118896
PHPH	5	59,00279	5,595531	205,8475	9,785332	58,98548	5,623239	206,2364	9,992738
	50	58,55174	6,317222	204,125	8,866689	60,51633	3,173872	204,7546	9,202432
	500	58,50741	6,388136	203,9609	8,779121	-10,4773	116,7636	203,6818	8,630319
PHPHN	5	60,48668	3,221308	209,2846	11,61844	60,78933	2,737071	211,0143	12,54098
	50	58,71954	6,048739	204,4374	9,033277	59,34427	5,049176	205,8436	9,783237
	500	58,53391	6,345747	203,9511	8,773919	-1,62039	102,5926	204,758	9,204265
3PH	5	58,61378	6,217954	203,9453	8,770834	71,07446	13,71913	256,645	36,87736
	50	58,33945	6,656875	202,727	8,12108	54,03431	13,54511	169,8757	9,399614
	500	58,29433	6,729079	202,4648	7,981204	-54,8945	187,8312	165,5965	11,68186

Table 4.26: Estimation of fault location for modified network (catalogue impedance) at 6pm - Phase C

		PHASE C - GRID CONNECTED							
	Fault Size (Ω)	No DG				DG			
		62.5 m	%Error	187.5 m	%Error	62.5 m	%Error	187.5 m	%Error
PHG	5	82,76758	32,42812	158,2374	15,60674	72,67526	16,28042	141,7763	24,38597
	50	60,94882	2,481892	191,3623	2,059888	59,19356	5,290296	196,4818	4,790309
	500	59,9024	4,156167	187,4943	0,00304	56,14812	10,16301	190,3496	1,519761
PHN	5	58,42112	6,526204	186,0559	0,770164	58,01263	7,179788	186,5471	0,508227
	50	57,88308	7,387078	184,9359	1,367541	48,36179	22,62114	184,7409	1,471526
	500	49,2464	21,20577	184,8344	1,421644	58,36877	6,609969	186,6545	0,450949
PHNG	5	69,1286	10,60576	107,6962	42,56203	66,23667	5,978667	-175,191	193,4353
	50	60,86481	2,616303	191,0551	1,89606	59,16319	5,3389	194,0782	3,508375
	500	59,90392	4,153731	187,5172	0,009182	56,09779	10,24354	189,2138	0,914028
PHPH	5	50,80709	18,70865	173,1306	7,663658	51,75791	17,18734	173,6799	7,370718
	50	49,05306	21,5151	172,392	8,05762	50,61089	19,02258	173,0751	7,693289
	500	97,73741	56,37985	159,6728	14,84119	50,772	18,76479	172,9066	7,783152
PHPHN	5	60,31896	3,489657	187,9241	0,22621	59,92124	4,12602	188,6674	0,622629
	50	58,20892	6,865723	185,0518	1,305705	53,54988	14,3202	185,3194	1,163006
	500	53,4635	14,4584	184,7687	1,456712	57,62654	7,797542	186,2274	0,678694
3PH	5	58,07714	7,076582	185,0999	1,280069	57,17128	8,525956	177,2848	5,448088
	50	57,32657	8,277493	185,0356	1,314371	302,6212	384,194	173,0397	7,712134
	500	55,47005	11,24792	184,7027	1,491899	66,95981	7,135703	149,1589	20,44857

Table 4.26 similarly shows that the algorithm can locate a fault with extremely good accuracy. With results from all three phases, the most accurate fault location estimation can be determined. Cross analysing multiple results increases the accuracy of the algorithm and makes it more robust by providing multiple sources of information sources.

The results for the different impedance models are shown below in Table 4.27.

Table 4.27: Average accuracy for Modified Network (Grid-connected) at 6 p.m.

		Phase A	Phase B	Phase C
Catalogue impedance model	Average % error	8.85	10.13	8.29
	Invalid estimations out of 72	6	4	3
Analytical impedance model	Average % error	9.31	10.13	7.83
	Invalid estimations out of 72	6	4	5
F.E. impedance model	Average % error	8.85	11.60	8.29
	Invalid estimations out of 72	6	3	2
Experiment impedance model	Average % error	9.13	10.59	6.92
	Invalid estimations out of 72	6	4	4

It is noted that the average accuracies are comparatively similar to the average accuracies obtained at noon, Table 4.23. This shows the ability of the algorithm to maintain accuracy at different times of the day with varying load and generation.

4.2.2.2 Islanded mode

The modified network is then operated in islanded mode to evaluate the performance of the algorithm in this mode. The network is shown below in Figure 4.56.

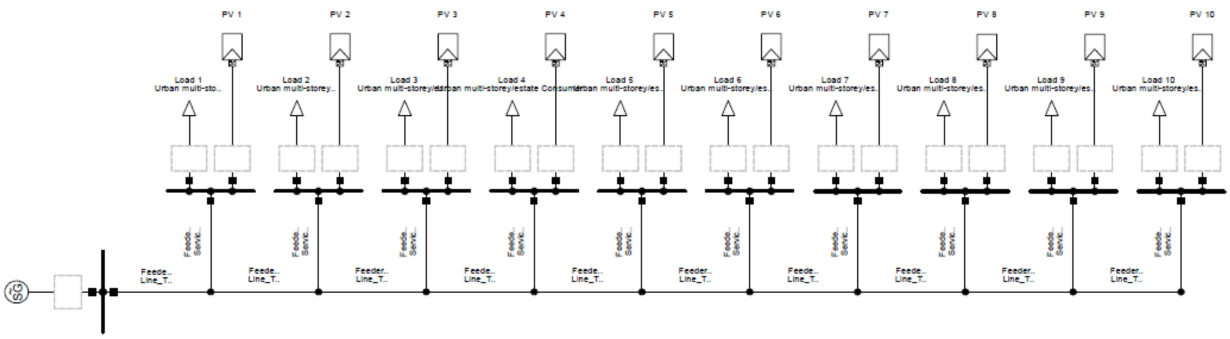

Figure 4.56: Modified network (Islanded mode)

The network has disconnected from the grid however power supply to the consumers is maintained through each consumers' individual DG and through the connected diesel generator. The diesel generator acts as the reference and feeds power to the islanded network.

Figure 4.57 shows the voltage profile of the network at noon and Figure 4.58 shows the voltage profile at 6 p.m.

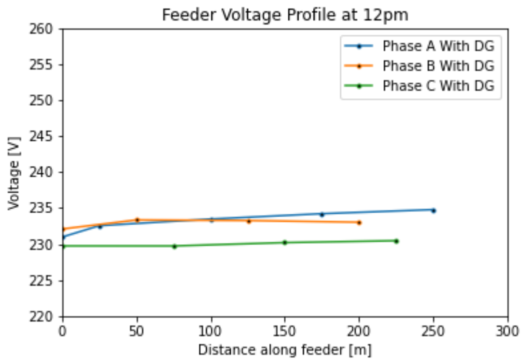

Figure 4.57: Islanded Modified Network Combined Phase Comparison at noon

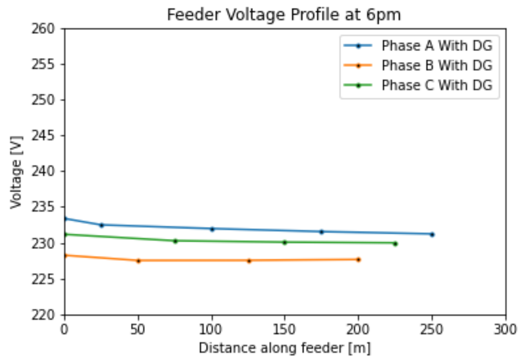

Figure 4.58: Islanded Modified Network Combined Phase Comparison at 6pm

Figure 4.57 shows a better voltage profile due to the higher PV generation that occurs at noon when compared with at 6 p.m. The network is unbalanced and is evidenced by the unbalanced voltage rise in the phases.

The procedure is followed, as for the grid connected network, with faults being simulated at the locations shown in Figure 4.59 to Figure 4.61. This is done for all the impedance models.

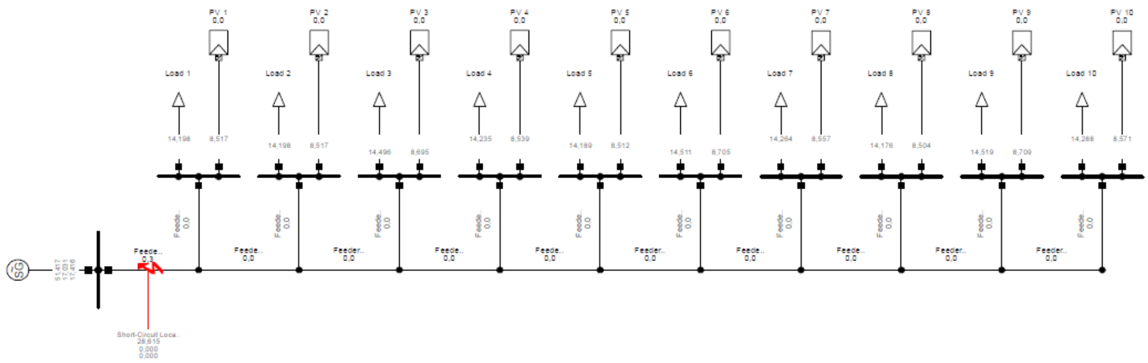

Figure 4.59: Modified network (Islanded mode) with fault at the beginning of the feeder

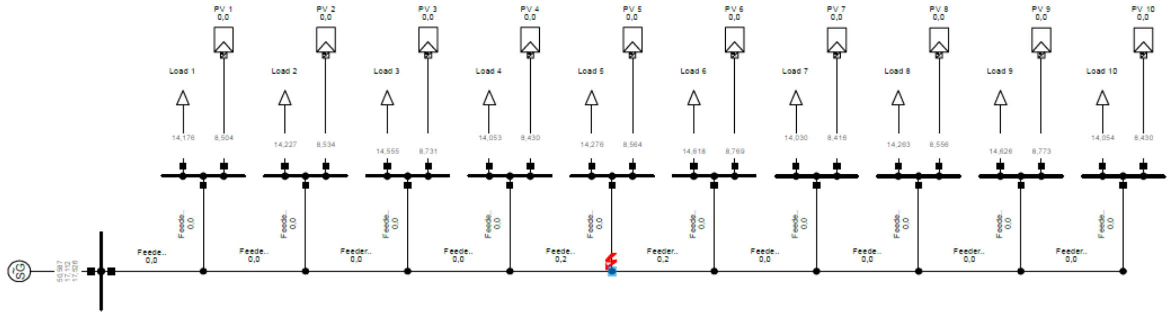

Figure 4.60: Modified network (Islanded mode) with fault at the middle of the feeder

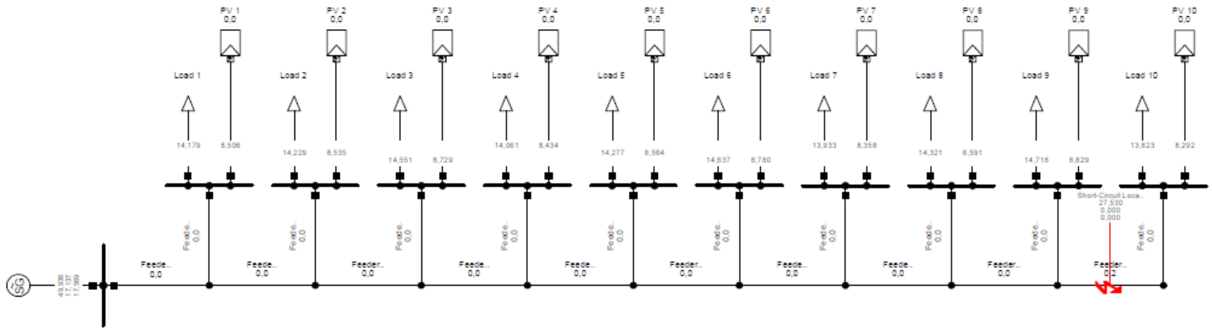

Figure 4.61: Modified network (Islanded mode) with fault at the end of the feeder

Detailed analysis of the voltage readings along the feeder showed similarity to those in Section 4.2.2.1 except with differing values. This is expected and hence for brevity is not included.

Figure 4.62 and Figure 4.63 show the test fault locations used to evaluate accuracy of the fault location estimation. As with the grid connected network, the location of test faults 1 and 2 are at 62.5 m and 187.2 m along the feeder, respectively.

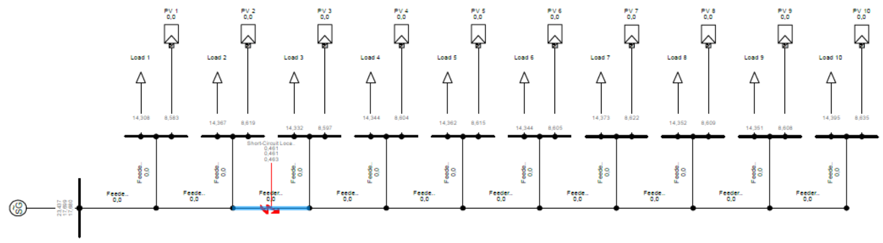

Figure 4.62: Islanded Modified network with test fault 1

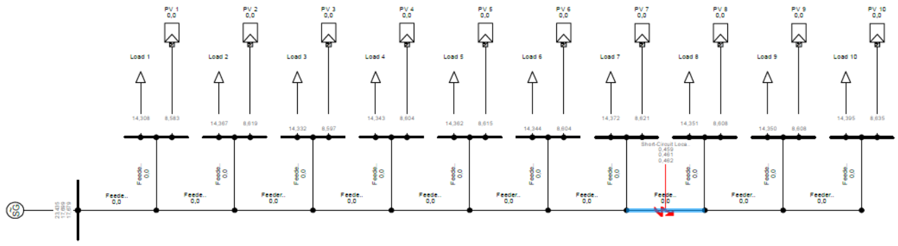

Figure 4.63: Islanded Modified network with test fault 2

The results of the fault location estimation are shown in Table 4.28 to Table 4.34 for the catalogue impedance model.

Table 4.28 show the results from using the Phase A readings at noon.

Table 4.28: Estimation of fault location for islanded modified network (catalogue impedance) at noon - Phase A

		PHASE A - ISLANDED			
	Fault Size (Ω)	DG			
		62.5 m	%Error	187.5 m	%Error
PHG	**5**	66,10336	5,765375	-1040,17	654,7579
	50	57,23925	8,417199	189,8095	1,231729
	500	50,76265	18,77975	176,507	5,862953
PHN	**5**	43,40904	30,54554	187,8623	0,193247
	50	68,00836	8,813373	177,7481	5,201001
	500	59,80669	4,30929	125,5981	33,01432
PHNG	**5**	62,53512	0,056191	228,4192	21,82355
	50	57,43376	8,105987	189,8908	1,275068
	500	54,43677	12,90116	176,3502	5,946549
PHPH	**5**	56,03614	10,34218	182,5146	2,65887
	50	52,25518	16,39171	184,079	1,824525
	500	54,16961	13,32863	185,0764	1,292582
PHPHN	**5**	77,92868	24,68588	159,4393	14,96573
	50	139,0227	122,4363	180,2683	3,856902
	500	56,64694	9,364888	188,3342	0,444891
3PH	**5**	-1063,87	1802,198	173,4851	7,474605
	50	47,90295	23,35528	194,9396	3,967766
	500	47,36923	24,20922	182,2927	2,777244

Table 4.28 shows that the algorithm can locate a fault with good accuracy. As seen with the results from the grid connected network, the accuracy seems to increase for faults further down the feeder. However, the faults highlighted in red are not able to be detected by the results from Phase A. This inaccuracy is improved by cross-analysing with the results below.

Table 4.29 show the results from using the Phase B readings at noon.

Table 4.29; Estimation of fault location for islanded modified network (catalogue impedance) at noon - Phase B

		PHASE B - ISLANDED			
	Fault Size (Ω)	DG			
		62.5 m	%Error	187.5 m	%Error
PHG	5	73,5692	17,71071	134,0257	28,5196
	50	59,62779	4,595541	193,0214	2,944732
	500	58,62425	6,201205	189,4159	1,021792
PHN	5	61,91817	0,930922	248,6375	32,60666
	50	74,43847	19,10156	228,1703	21,69082
	500	82,99673	32,79477	205,8133	9,767078
PHNG	5	67,94099	8,705582	-29,8737	115,9327
	50	60,31884	3,489852	195,8986	4,479266
	500	59,24231	5,212298	191,2643	2,007649
PHPH	5	64,7409	3,585434	251,8915	34,34214
	50	61,74134	1,213859	204,7751	9,213406
	500	71,04125	13,66599	204,0415	8,822107
PHPHN	5	59,54181	4,7331	195,9072	4,483837
	50	65,30847	4,493545	202,9259	8,227127
	500	74,02041	18,43265	204,4178	9,022835
3PH	5	181,3945	190,2312	171,5764	8,492562
	50	20,49203	67,21274	166,2121	11,35352
	500	25,34693	59,44492	166,2092	11,3551

Table 4.29 similarly shows that the algorithm can locate a fault with extremely good accuracy. The inaccuracies in the fault location estimation from this fault are resolved with cross-analysis with the preceding results. However, the inaccuracy of the 3-PH fault is not resolved by the Phase B results therefore further cross analysis with the Phase C results is required.

Table 4.30 show the results from using the Phase C readings at noon.

Table 4.30 similarly shows that the algorithm can locate a fault with extremely good accuracy. With results from all three phases, the most accurate fault location estimation can be determined. The results for the average accuracy for the different impedance models are shown in Table 4.31.

Table 4.30: Estimation of fault location for islanded modified network (catalogue impedance) at noon - Phase C

		PHASE C - ISLANDED			
	Fault Size (Ω)	DG			
		62.5 m	%Error	187.5 m	%Error
PHG	5	76,63686	22,61898	143,458	23,48905
	50	60,47188	3,244992	198,5891	5,914175
	500	58,04256	7,131908	194,6426	3,809376
PHN	5	59,55395	4,713673	-71,7743	138,2796
	50	57,53264	7,947775	187,7461	0,131249
	500	57,35942	8,224925	187,7815	0,150153
PHNG	5	68,85644	10,17031	122,3086	34,76875
	50	60,19318	3,690918	195,5238	4,279372
	500	57,77965	7,552567	192,2643	2,540945
PHPH	5	39,40806	36,9471	173,956	7,223493
	50	-37,6809	160,2895	171,4971	8,53489
	500	-751,503	1302,405	170,6647	8,9788
PHPHN	5	59,7376	4,41984	189,203	0,908272
	50	57,61418	7,817308	187,0876	0,219959
	500	57,4796	8,032647	187,3727	0,067869
3PH	5	60,97138	2,445794	202,1972	7,838525
	50	56,89963	8,960598	160,406	14,45015
	500	56,44225	9,692395	158,9935	15,20345

Table 4.31: Average accuracy for Modified Network (Islanded) at noon

		Phase A	Phase B	Phase C
Catalogue impedance model	Average % error	10.20	10.96	8.87
	Invalid estimations out of 36	2	3	2
Analytical impedance model	Average % error	9.91	10.51	10.79
	Invalid estimations out of 36	3	5	1
F.E. impedance model	Average % error	8.26	11.12	8.26
	Invalid estimations out of 36	3	5	3
Experiment impedance model	Average % error	10.45	7.52	10.51
	Invalid estimations out of 36	4	6	1

The algorithm proves to maintain accuracy through the network transition to islanded operating mode. The low number of invalid estimations highlight the robustness of the algorithm to the different fault types. Furthermore, cross-analysis between the phases improves the invalid estimations.

The procedure is repeated for the 6 p.m. scenario with Table 4.32 showing the results for Phase A.

Table 4.32: Estimation of fault location for islanded modified network (catalogue impedance) at 6pm - Phase A

		PHASE A - ISLANDED			
	Fault Size (Ω)	DG			
		62.5 m	%Error	187.5 m	%Error
PHG	**5**	87,20968	39,53549	153,717	18,01762
	50	60,01731	3,97231	194,1722	3,558489
	500	58,70248	6,076026	188,8515	0,720792
PHN	**5**	56,85284	9,035459	187,7809	0,149829
	50	54,91841	12,13055	186,3146	0,6322
	500	55,86142	10,62173	186,7448	0,402796
PHNG	**5**	66,66996	6,67193	-172,348	191,9191
	50	59,66796	4,53127	193,299	3,092787
	500	58,48133	6,429874	188,7272	0,654488
PHPH	**5**	57,71885	7,649842	185,1748	1,240129
	50	45,13766	27,77974	181,2183	3,350257
	500	56,36204	9,820728	187,906	0,216534
PHPHN	**5**	54,73852	12,41837	190,7124	1,713299
	50	55,12992	11,79212	187,0102	0,261237
	500	56,06206	10,30071	186,942	0,297611
3PH	**5**	62,95775	0,732402	197,6119	5,393
	50	145,8562	133,3699	175,1797	6,570813
	500	-4488,05	7280,879	176,5307	5,850307

With a change in the load and PV generation, it can be seen from Table 4.32 that the algorithm maintains its ability to locate a fault accurately. The inaccuracies in these results are cross analysed with results from the phases below.

Table 4.33 show the results from using the Phase B readings at 6 p.m.

Table 4.33 similarly shows that the algorithm can locate a fault with extremely good accuracy. Where the estimations are inaccurate, they are accurate in the estimations from Phase A. Also, where the estimations in Phase A were inaccurate, they are accurate in the estimations in Phase B.

Table 4.34 shows the results from using the Phase C readings at 6 p.m.

Table 4.34 similarly shows that the algorithm can locate a fault with extremely good accuracy. With results from all three phases, the most accurate fault location estimation can be determined.

The average accuracy results for the different impedance models are summarised below in Table 4.35.

Table 4.33: Estimation of fault location for islanded modified network (catalogue impedance) at 6pm - Phase B

		PHASE B - ISLANDED			
	Fault Size (Ω)	DG			
		62.5 m	%Error	187.5 m	%Error
PHG	5	734,4501	1075,12	162,3162	13,43138
	50	70,22451	12,35922	40,4762	78,41269
	500	67,66128	8,258043	400,1448	113,4105
PHN	5	76,93816	23,10106	277,7309	48,12312
	50	61,78405	1,145517	203,873	8,732244
	500	62,67261	0,276182	204,5728	9,105507
PHNG	5	79,96999	27,95198	144,3739	23,0006
	50	68,24621	9,193938	-1679,74	995,8638
	500	66,40604	6,24966	275,8015	47,09413
PHPH	5	67,96184	8,738941	-266,573	242,1724
	50	61,06675	2,293195	206,8258	10,30709
	500	62,93416	0,694662	206,159	9,951456
PHPHN	5	60,74441	2,808951	197,8436	5,516602
	50	59,82033	4,287468	195,3135	4,167217
	500	62,66228	0,259643	204,8489	9,252763
3PH	5	56,11101	10,22238	187,4417	0,031109
	50	53,79155	13,93352	177,8972	5,121487
	500	52,62205	15,80473	177,1276	5,531965

Table 4.34: Estimation of fault location for islanded modified network (catalogue impedance) at 6pm - Phase C

		PHASE C - ISLANDED			
	Fault Size (Ω)	DG			
		62.5 m	%Error	187.5 m	%Error
PHG	5	120,7486	93,19769	167,2367	10,80712
	50	61,66016	1,343749	187,3937	0,056715
	500	51,48435	17,62504	180,3822	3,796173
PHN	5	59,80041	4,319337	188,6175	0,59602
	50	45,64009	26,97586	202,9579	8,244232
	500	58,56768	6,291719	183,3426	2,217267
PHNG	5	74,97934	19,96695	153,4777	18,14525
	50	61,68494	1,30409	188,8374	0,713305
	500	51,54759	17,52385	180,8127	3,566546
PHPH	5	43,93489	29,70418	175,6206	6,335701
	50	42,23652	32,42156	176,7777	5,71858
	500	41,94062	32,89501	177,0854	5,554454
PHPHN	5	58,62096	6,206458	187,2526	0,131943
	50	46,40901	25,74558	188,3466	0,451507
	500	58,17502	6,919974	188,4641	0,514174
3PH	5	58,51619	6,374102	192,8779	2,868197
	50	77,00217	23,20347	253,0333	34,95109
	500	60,0445	3,928803	203,1174	8,329273

Table 4.35: Average accuracy for Modified Network (Islanded) at 6 p.m.

		Phase A	Phase B	Phase C
Catalogue impedance model	Average % error	7.14	11.46	10.87
	Invalid measurements out of 36	3	5	1
Analytical impedance model	Average % error	11.30	10.83	10.83
	Invalid measurements out of 36	3	4	1
F.E. impedance model	Average % error	7.06	10.03	10.86
	Invalid measurements out of 36	3	6	1
Experiment impedance model	Average % error	7.77	10.05	10.50
	Invalid measurements out of 36	2	3	2

It is noted that the average accuracies are comparatively similar to the average accuracies obtained at noon, Table 4.31. This shows the ability of the algorithm to maintain accuracy at different times of the day with varying load and generation. The results also show similar accuracies in detecting, classifying, and locating faults in the network for the different impedance models. This indicates that although the impedance modelling technique applied will affect any voltage-based protection solution, the algorithm developed in this study is robust enough to maintain accuracy.

Chapter 5: Discussion

The results for the simulations of both the CIGRE Benchmark LV Model and the modified network model are shown in this section. Seven influencing parameters were analysed: (a) load and PV generation levels (these were determined from the time of day scenarios detailed in Table 4.11), (b) presence of DG (scenarios where there is DG and when there is no DG were considered), (c) grid connection (both grid-connected and islanded modes were considered), (d) fault type (various fault types were considered which included PH-G, PH-N, PH-N-G, PH-PH, PH-PH-N and 3-PH faults), (e) fault impedance (three different values were considered: 5 Ω, 50 Ω, 500 Ω), (f) fault location (the fault locations were varied between the beginning, middle and end of the feeder), (g) impedance model (various impedance models were considered including the manufacturer's catalogue impedance model, an analytical impedance model, a finite element impedance model and an experimental impedance model). Furthermore, the effect of a balanced network and an unbalanced network were considered with the comparison between the CIGRE Benchmark LV Model and the modified network model. The results obtained indicated the ability to clearly distinguish fault types, resistances, and locations. However, the distinction grew smaller for the higher resistance faults, as expected [80].

It is noticeable from the tabulated results that the percentage voltage difference increases as the terminal voltage decreases. This is evident with the larger differences seen with the terminal voltage values further down the feeder, with the lower fault resistance values and, with the difference in the values between no DG present and with the presence of DG. This conveys that the lower the terminal voltage, the greater the effect the impedance modelling approach has on the accuracy of the voltage reading. This is because the low differences in the impedance values between the different models are amplified in the voltage calculation in the network simulations. Following from the results presented in Section 4.1.3, the FE impedance model provided the lowest differences to the catalogue impedance model. This is reflected by the low differences in the impedance values in the models themselves. However, the analytical impedance model provided a slightly larger percentage voltage difference representing the effect of solely considering the cable to be purely resistive. Although the differences are small, they can be amplified depending on the application.

Initially it was thought a quantitative approach based on the successive nodal differences would suffice. However, the variation in the terminal voltage values indicated difficulty in building an algorithm that can detect and locate faults in the network that is purely quantitative. Furthermore, the 10% permissible voltage variation limit is not applicable for faults within this limit, and it is difficult to differentiate faults from voltage overloads for values outside this limit. Therefore, a comparative algorithm based on the voltage measurements was formulated (Section 3.2.5.2).

From the results of the CIGRE Benchmark LV Model, Section 4.2.1, the fault location could be accurately estimated however the average fault location estimation error was higher than that for the modified network model. Though still within reason this is assumed to be a result of the balanced network having a shared effect on all three phases. Therefore, a voltage distinction because of a fault becomes harder to analyse. This is detailed in the variation of the voltage differences for the CIGRE Benchmark LV Model and the modified network model. Furthermore, it was noted that the algorithm developed works more accurately for an unbalanced network as the phase voltages provide distinct sources of information. Fault location was able to be conducted regardless of the presence of DG or not. This is because of the comparison approach used that ensures robustness despite network operational changes. The comparative method provides a distinct pattern (Euclidean value) for faults which can then be used to differentiate from events such as overload which would create a different pattern.

The results of modified network show that the fault location could be accurately estimated regardless of the change in variable parameters. In Section 4.2, the effect of the impedance modelling technique, Section 4.1, has on the voltage profile of the feeder was detailed. For any voltage-based protection scheme this must be considered. Even more so for an analysis of high-impedance faults as the voltage profile under faulted conditions approaches that of the normal load condition. The algorithm proved to be adaptable to this change in impedance model because it is a comparison method therefore the voltage profile of the impedance model in use is always accounted. The estimations for the different impedance models were comparatively similar.

5.1.1.1 Practical Implementation

A. Fault Location estimation.

The DTW algorithm was able to provide good accuracy for the fault location for the different scenarios. An adequate accuracy for the fault location can be defined as an accuracy that is helpful to field staff locating a fault in a network. It often suffices to provide a sector of the feeder to field staff. However, the accuracies obtained with the DTW algorithm are much higher. The greatest impacting parameters on accuracy of the fault location estimation were the size of the fault resistances and the accuracy of the voltage measurements. A minimum accuracy from the smart meters is required in order to maintain any useful estimation accuracy.

B. Fault resistance sensitivity.

The fault resistance was varied to determine the effect this has on the DTW algorithm. The effect on the voltage profile was detailed and showed that for low-resistance faults; the effect was distinct enough to fall outside of the 10% limit of variation [26]. However, the voltage values were within limits for the high-resistance faults. The increased difficulty in detecting and locating faults was reflected in the decrease in the accuracy of the DTW algorithm. However, a high accuracy was still maintained but this is highly dependent on the accuracy of the voltage measurements. Low accuracy voltage measurements increase the accuracy error of the DTW algorithm particularly for high-resistance faults.

C. Smart meter accuracy.

The performance of the algorithm is highly dependent on the accuracy of the smart meters. Defined as metering devices, smart meters have two accuracy classes (Section 2.5). The ranges for the permissible accuracy are defined with 0.2%, for the 0.2S accuracy class, around 0,9 U_n< U < 1.1 U_n. For voltages below 80% of the nominal voltage, the error of the smart meter may vary between +10% and -100%. It is noted that this accuracy would not be useful for fault detection and location using the proposed DTW algorithm. The low-resistance faults cause voltages outside the 10% variation limit however the permissible accuracy of the smart meter is too low to be useful to the algorithm. High-resistance faults occur within the 10% limit however due to their much smaller impact on the voltage variation, 0.2% (= 0.46V) is insufficient to accurately apply the DTW algorithm. Results for an accuracy of 0.043% (= 0.1V) are shown in Table 5.1 with the detailed results shown in the Annexure.

Table 5.1: Method accuracy for smart meter with accuracy of 0.043%

	Catalogue impedance model	
	Average error %	Invalid estimations out of 72
Phase A	11.48	22
Phase B	10.80	25
Phase C	12.98	30

The accuracy is generally lower than that shown in the previous result. This accuracy level is adequate for lower resistance faults but is reduced for higher resistance faults. Cross-analysis between the phases showed that the number of undetectable faults increased for this accuracy level. The simulation was repeated for an accuracy of 0.0043% (= 0.01V) to ascertain the minimum accuracy required for high-resistance faults. The results are shown in Table 5.2 with the detailed results shown in the Annexure.

Table 5.2: Method accuracy for smart meter with accuracy of 0.0043%

	Catalogue impedance model	
	Average error %	Invalid estimations out of 72
Phase A	9.86	12
Phase B	8.73	12
Phase C	7.98	10

The accuracy of the fault location estimation improved and there was a large reduction in the number of undetectable faults per phase. Cross-analysis between the three phases further increases the accuracy of the estimation.

It can be concluded that as low-resistance faults result in a low voltage being recorded at the consumers' terminals, a lower smart meter accuracy can be applied. A higher accuracy should be applied for voltages within the 10% limit to cater for the higher resistance faults. Therefore, an adjustable accuracy for the voltage range can be determined. It is recommended that 0.2% be applicable for voltages as low as 0.2 U_n. For 0,9 U_n< U < 1.1 U_n, a minimum accuracy of 0.04% is recommended.

D. Smart meter availability.

In this study, it was assumed that there would be 100% smart meter data availability. However, it is possible this may not be the case because of numerous reasons such as a consumer lacking a smart meter or smart meter communication packet loss amongst others. As detailed in Section 2.2.6, the DTW algorithm compares two frames and gives a measure of similarity. This is illustrated in Figure 5.1 with a comparison being made of the voltage profile against itself. The point-by-point comparison shows the similarity procedure and the Euclidean distance for this is calculated as 0. In Figure 5.2, a data point in the middle of the feeder is missing and the distance calculated is 1.62. This small difference is comparable to the detection of a fault/change however the fault location estimation shows an improbable inaccuracy for all the known faults. This is used to classify the network as missing a data point. In Figure 5.3, a data point at the end of the feeder is missing and the distance calculated is 1.18. As described above, this can also be classified as missing data. In Figure 5.4, two data points from the end of the feeder are missing and the distance calculated is 2.37. Similarly, this can be classified as missing data. In Figure 5.5, there is a false zero value given from the middle of the feeder and the distance calculated is 223.27. This value also fails to trigger the location of any known faults however the high distance value would indicate the voltage profile is far from normal operation.

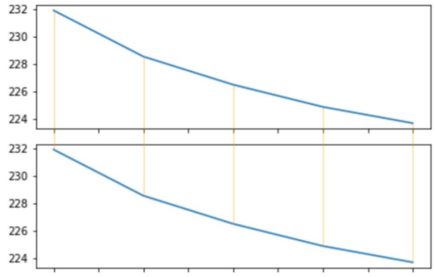

Figure 5.1: DTW comparison of voltage profile against itself

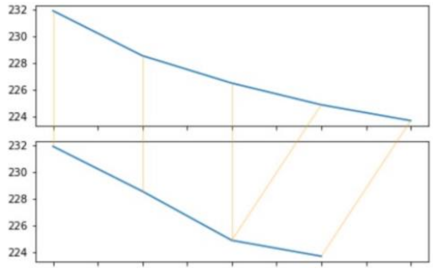

Figure 5.2: DTW comparison of voltage profile with middle data point missing

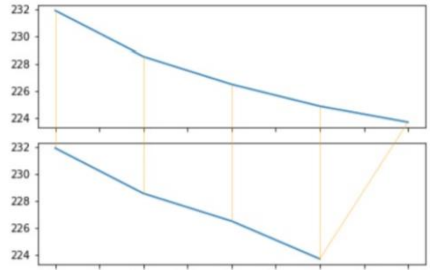

Figure 5.3: DTW comparison of voltage profile with end data point missing

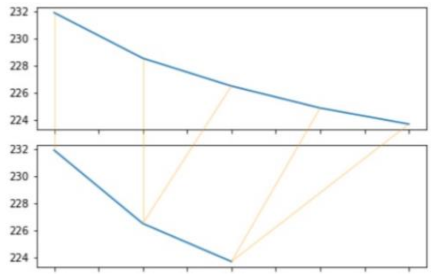

Figure 5.4: DTW comparison of voltage profile with 2 data points missing from the end

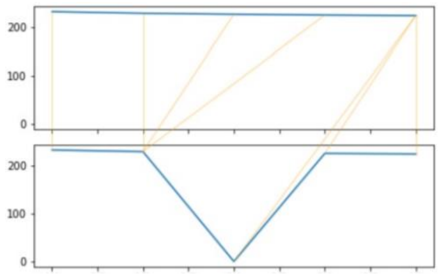

Figure 5.5: DTW comparison of voltage profile with false zero value

When a fault occurs in a phase in the network, a voltage change occurs in all the other phases as well. Hence, this is used to distinguish between faults and missing data, as in the case of missing data the other phases are unaffected. However, a missing data point/packet loss is better than the reporting of a false value as a large deviation from normal operation is inferred.

The minimum number of smart meters adequate for the algorithm to be useful is dependent on the number of consumer nodes and the location of the smart meters. The results indicate that at minimum, more than half of the consumers on the feeder should have an installed smart meter. The locations of these smart meters should be such that a suitable voltage profile of the beginning, middle and end of the feeder can be generated. This is to ensure sufficient visibility of the feeder's voltage profile and to maintain accuracy of the DTW algorithm.

Chapter 6: Conclusion and Future work

6.1 Conclusion

Protection is a critical task in the design and operation of an AC microgrid. The complexities therewith are numerous due to the varying network conditions. This study provides a comprehensive review of the microgrid and the protection issues. The solutions proposed in previous research are explored and a case is made for the application of a voltage-based protection technique. Basing a fault location technique on voltage measurements reduces the associated complexities of current monitoring. This technique proves advantageous with the global trend of smart meter adoption. The adoption of smart meters into households provides the opportunity for creating a distributed sensor network in the microgrid. The proposed fault location technique builds on using distributed voltage measurements to create a voltage profile of the network. The voltage profile of the network is then used to detect, classify and locate faults.

To achieve the objectives, this study is constructed of three main sections. These are LV network modelling, simulation and data analysis. An emphasis is made on the different cable impedance modelling techniques with the experimental impedance modelling results used for validation. The microgrid network simulations indicated the complexity of fault detection and location for high-resistance faults and for certain fault types. This observation led to the novel application of Dynamic Time Warping (DTW) for fault detection and location in an LV microgrid. The proposed DTW algorithm has been described and the application of the DTW algorithm evaluated. The proposed DTW algorithm has been evaluated through DIgSILENT simulations. The results of the fault location estimation show that the DTW algorithm is not reliant on the impedance modelling technique used, time of day, grid connection or presence of DG. It can maintain its accuracy as it is built on pre-knowledge of normal operation of the network regardless of the operating scenario. As the method used is voltage-based, this indicates the robustness of the algorithm. The fault location estimation showed good accuracy but decreased slightly for high-resistance faults. It was found that high-resistance faults were not the most determining factor in the accuracy of the DTW algorithm, but it was the quality of the input data. Low-accuracy voltage measurements led to the DTW algorithm showing high inaccuracies for the fault location estimation. The current standards define smart meters as metering devices and assign them an accuracy accordingly. However, to extend their functionality to include fault detection, classification and location, an improvement in their accuracy is recommended. This increase in accuracy will ensure greater benefit from having smart meters dispersed in a network.

6.2 Future work

Future work should include the practical implementation of the suggested system. A test smart meter with the recommended accuracy can be built and deployed in a test microgrid. As in the work done by [79], this investigation would determine the viability of the proposed algorithm. Furthermore, in this study two operating times were considered, noon and 6 p.m. Further work should include simulations that cover a complete day. This would allow a database of results for the normal operation to be created hence more accurate parameters for fault detection and location could be created. An investigation into at what time of the day, or under what load and PV generation conditions, make the DTW algorithm more susceptible to conflation errors should also be done. The Euclidean distance was the preferred method however it would be interesting to investigate whether using alternative distance metrics such as the Manhattan, Canberra or Cosine distance [66] could improve the performance of the DTW algorithm. Of particular interest would be the Cosine distance metric due its high robustness. The main disadvantage of the Euclidean algorithm is its high sensitivity to accuracy of data. Any future work that could improve this aspect would improve this study.

References

[1] G. Pepermans, J. Driesen, D. Haeseldonckx, W. D'haeseleer, and R. Belmans, "Distributed generation : Definition , Benefits and Issues," *Energy Transp. Environ. KULEVEN - ENERGY Inst.*, no. August 2003, 2003.
[2] T. Ackermann, G. Andersson, and L. Soder, "Distributed generation : a definition,", *Elsevier*, vol. 57, pp. 195–204, 2001.
[3] E. C. Piesciorovsky, "Microgrid Fault Location : Challenges and Solutions Microgrid Fault Location : Challenges and Solutions," no. June, 2018, doi: 10.13140/RG.2.2.34247.39842.
[4] N. Nimpitiwan and G. Heydt, "Consequences of Fault Currents Contributed by Distributed Generation," *Power Syst. Eng. Res. Cent.*, no. PSERC Publication 06-21, 2006.
[5] N. Sapountzoglou, B. Raison, and N. Silva, "A Fault Localization Method for Single-phase to Ground Faults in LV Smart Distribution Grids,", *HAL*, p. 7, 2019.
[6] V. Van Thong, J. Driesen, and R. Belmans, "Interconnection of Distributed Generators and Their Influences on Power System," *Int. Energy J.*, vol. 6, no. 1, pp. 127–140, 2005.
[7] Y. Bansal, "Microgrid fault detection methods : Reviews , issues and future trends," *2018 IEEE Innov. Smart Grid Technol. - Asia ISGT Asia*, pp. 401–406, 2018, doi: 10.1109/ISGT-Asia.2018.8467938.
[8] S. S. Venkata, M. J. Reno, W. Bower, S. Manson, J. Reilly, and G. W. Sey, "Microgrid Protection: Advancing the State of the Art,", Sandia National Laboratories, California, 2019.
[9] E. Lakervi and E. J. Holmes, *Electricity distribution network design*. London, United Kingdom: IEEE Power and Energy Series, 1989.
[10] C. Marnay, F. J. Robio, and A. S. Siddiqui, "Shape of the microgrid," in *2001 IEEE Power Engineering Society Winter Meeting. Conference Proceedings (Cat. No.01CH37194)*, Columbus, OH, USA, 2001, vol. 1, pp. 150–153. doi: 10.1109/PESW.2001.917022.
[11] S. S. Venkata, M. J. Reno, W. Bower, and S. Manson, "Microgrid Protection - Advancing the State of the Art," Sandia National Laboratories, New Mexico, USA, May 2019.
[12] D. Chen and L. Xu, "AC and DC Microgrid with Distributed Energy Resources," in *Technologies and Applications for Smart Charging of Electric and Plug-in Hybrid Vehicles*, O. Veneri, Ed. Cham: Springer International Publishing, 2017, pp. 39–64. doi: 10.1007/978-3-319-43651-7_2.
[13] S. Papathanassiou, N. Hatziargyriou, and K. Strunz, "A Benchmark Low Voltage Microgrid Network," *Power Syst. Dispersed Gener. Technol. Impacts Dev. Oper. Perform.*, p. 9, Apr. 2005, doi: CIGRE.
[14] C. Buque, "Metering and adaptive protection for a Microgrid with distributed generation,", MSc Dissertation, University of Cape Town, Cape Town, SA, 2013.
[15] J. Csatár and A. Dán, "LV Grid Modeling Including Consumption and Distributed PV Generation with Focus on Voltage Profile," *Period. Polytech. Electr. Eng. Comput. Sci.*, vol. 59, no. 3, pp. 110–117, 2015, doi: 10.3311/PPee.8574.
[16] F. Olivier, R. Fonteneau, and D. Ernst, "Modelling of three-phase four-wire Low-Voltage cables taking into account the neutral connection to the earth," *CIRED Workshop*, no. 0593, p. 4, 2018.
[17] H. Nikkhajoei and R. H. Lasseter, "Microgrid Protection," presented at the IEEE PES General Meeting, Tampa, FL, Jun. 2007.
[18] H. J. Laaksonen, "Protection Principles for Future Microgrids," *IEEE Trans. Power Electron.*, vol. 25, no. 12, pp. 2910–2918, Dec. 2010, doi: 10.1109/TPEL.2010.2066990.

[19] A. Oudalov and A. Fidigatti, "Adaptive Network protection in microgrids," Switzerland, p. 24.
[20] J. Peronnet, "Electrical Installation Guide 2018." Schneider Electric, 2018. [Online]. Available: schneider-electric.com/eig
[21] N. Jayawarna, N. Jenkins, M. Barnes, M. Lorentzou, S. Papthanassiou, and N. Hatziagyriou, "Safety analysis of a microgrid," in *2005 International Conference on Future Power Systems*, Amsterdam, The Netherlands, 2005, p. 7 pp. – 7. doi: 10.1109/FPS.2005.204228.
[22] J. L. Blackburn and T. J. Domin, "Protective Relaying: Principles and Applications," p. 638, 2006.
[23] D. T. K. Abdel-Galil, A. E. B. Abu-Elanien, D. E. F. El-Saadany, and D. A. Girgis, "Protection Coordination Planning with Distributed Generation," *Final Rep.*, p. 197, 2007.
[24] A. R. Haron, A. Mohamed, and H. Shareef, "Coordination of Overcurrent, Directional and Differential Relays for the Protection of Microgrid System," *Procedia Technol.*, vol. 11, pp. 366–373, 2013, doi: 10.1016/j.protcy.2013.12.204.
[25] K. Balamurugan, D. Srinivasan, and T. Reindl, "Impact of Distributed Generation on Power Distribution Systems," *Energy Procedia*, vol. 25, pp. 93–100, 2012, doi: 10.1016/j.egypro.2012.07.013.
[26] SABS, "SANS 1019 Standard voltages, currents and insulation levels for electricity supply." SABS Standards Division, 2014.
[27] M. Farhoodnea, A. Mohamed, H. Shareef, and H. Zayandehroodi, "Power quality impacts of high-penetration electric vehicle stations and renewable energy-based generators on power distribution systems," *Measurement*, vol. 46, no. 8, pp. 2423–2434, Oct. 2013, doi: 10.1016/j.measurement.2013.04.032.
[28] S. H. Horowitz and A. G. Phadke, *Power System Relaying*, Fourth Edition. United Kingdom: Wiley, 2014.
[29] M. Bamber, M. Bergstom, A. Darby, and S. Darby, *Network Protection & Automation Guide*, First Edition. Stafford, UK: Alstom Grid, 2011.
[30] S. Beheshtaein, M. Savaghebi, J. C. Vasquez, and J. M. Guerrero, "Protection of AC and DC microgrids: Challenges, solutions and future trends," in *IECON 2015 - 41st Annual Conference of the IEEE Industrial Electronics Society*, Yokohama, Nov. 2015, pp. 005253–005260. doi: 10.1109/IECON.2015.7392927.
[31] Y. Bansal and R. Sodhi, "Microgrid fault detection methods: Reviews, issues and future trends," in *2018 IEEE Innovative Smart Grid Technologies - Asia (ISGT Asia)*, Singapore, May 2018, pp. 401–406. doi: 10.1109/ISGT-Asia.2018.8467938.
[32] S. S. Hossain-Mckenzie, E. C. Piesciorovsky, M. J. Reno, and J. C. Hambrick, "Microgrid Fault Location: Challenges and Solutions," 2018, doi: 10.13140/rg.2.2.34247.39842.
[33] R. M. Tumilty, M. Brucoli, G. M. Burt, and T. C. Green, "Approaches to network protection for inverter dominated electrical distribution systems," in *3rd IET International Conference on Power Electronics, Machines and Drives (PEMD 2006)*, Dublin, Ireland, 2006, vol. 2006, pp. 622–626. doi: 10.1049/cp:20060183.
[34] E. Sortomme, G. J. Mapes, B. A. Foster, and S. S. Venkata, "Fault analysis and protection of a microgrid," in *2008 40th North American Power Symposium*, Calgary, AB, Canada, Sep. 2008, pp. 1–6. doi: 10.1109/NAPS.2008.5307360.
[35] U. Shahzad, S. Kahrobaee, and S. Asgarpoor, "Protection of Distributed Generation: Challenges and Solutions," *Energy Power Eng.*, vol. 09, no. 10, pp. 614–653, 2017, doi: 10.4236/epe.2017.910042.
[36] A. R. Haron, A. Mohamed, H. Shareef, and H. Zayandehroodi, "Analysis and solutions of overcurrent protection issues in a microgrid," in *2012 IEEE International Conference on*

Power and Energy (PECon), Kota Kinabalu, Malaysia, Dec. 2012, pp. 644–649. doi: 10.1109/PECon.2012.6450293.
[37] N. Kang, J. Wang, R. Singh, and X. Lu, “Interconnection, Integration, and Interactive Impact Analysis of Microgrids and Distribution Systems,” ANL/ESD--17/4, 1349056, Jan. 2017. doi: 10.2172/1349056.
[38] J. L. Blackburn and T. J. Domin, *Protective Relaying: Principles and Applications*, Third Edition. Boca Raton, FL: CRC Press, 2006.
[39] L. Che, M. E. Khodayar, and M. Shahidehpour, “Adaptive Protection System for Microgrids: Protection practices of a functional microgrid system.,” *IEEE Electrification Mag.*, vol. 2, no. 1, pp. 66–80, Mar. 2014, doi: 10.1109/MELE.2013.2297031.
[40] A. M. Ibrahim, W. El-Khattam, M. ElMesallamy, and H. A. Talaat, “Adaptive protection coordination scheme for distribution network with distributed generation using ABC,” *J. Electr. Syst. Inf. Technol.*, vol. 3, no. 2, pp. 320–332, Sep. 2016, doi: 10.1016/j.jesit.2015.11.012.
[41] Y. Ates *et al.*, “Adaptive Protection Scheme for a Distribution System Considering Grid-Connected and Islanded Modes of Operation,” *Energies*, vol. 9, no. 5, p. 378, May 2016, doi: 10.3390/en9050378.
[42] Z. Wang, Z. Huang, C. Song, and H. Zhang, “Multiscale Adaptive Fault Diagnosis Based on Signal Symmetry Reconstitution Preprocessing for Microgrid Inverter Under Changing Load Condition,” *IEEE Trans. Smart Grid*, vol. 9, no. 2, pp. 797–806, Mar. 2018, doi: 10.1109/TSG.2016.2565667.
[43] Z. Li, W. Tong, F. Li, and S. Feng, “Study on Adaptive Protection System of Power Supply and Distribution Line,” in *2006 International Conference on Power System Technology*, Chongqing, China, Oct. 2006, pp. 1–6. doi: 10.1109/ICPST.2006.321948.
[44] H. F. Habib, C. R. Lashway, and O. A. Mohammed, “On the adaptive protection of microgrids: A review on how to mitigate cyber attacks and communication failures,” in *2017 IEEE Industry Applications Society Annual Meeting*, Cincinnati, OH, Oct. 2017, pp. 1–8. doi: 10.1109/IAS.2017.8101886.
[45] C. Chandraratne, T. Logenthiran, R. T. Naayagi, and W. L. Woo, “Overview of Adaptive Protection System for Modern Power Systems,” in *2018 IEEE Innovative Smart Grid Technologies - Asia (ISGT Asia)*, Singapore, May 2018, pp. 1239–1244. doi: 10.1109/ISGT-Asia.2018.8467827.
[46] G. K. Purushothama, A. U. Narendranath, D. Thukaram, and K. Parthasarathy, “ANN applications in fault locators,” *Int. J. Electr. Power Energy Syst.*, vol. 23, no. 6, pp. 491–506, Aug. 2001, doi: 10.1016/S0142-0615(00)00068-5.
[47] M. Shafiullah and M. A. Abido, “A Review on Distribution Grid Fault Location Techniques,” *Electr. Power Compon. Syst.*, vol. 45, no. 8, pp. 807–824, May 2017, doi: 10.1080/15325008.2017.1310772.
[48] A. S. Bretas, L. Pires, M. Moreto, and H. Salim, “A BP Neural Network Based Technique for HIF Detection and Location on Distribution Systems With Distributed Generation,” p. 6.
[49] G. Cardoso, J. G. Rolim, and H. H. Zurn, “Application of Neural-Network Modules to Electric Power System Fault Section Estimation,” *IEEE Trans. Power Deliv.*, vol. 19, no. 3, pp. 1034–1041, Jul. 2004, doi: 10.1109/TPWRD.2004.829911.
[50] S. A. M. Javadian, A. M. Nasrabadi, M.-R. Haghifam, and J. Rezvantalab, “Determining fault’s type and accurate location in distribution systems with DG using MLP Neural networks,” in *2009 International Conference on Clean Electrical Power*, Capri, Italy, Jun. 2009, pp. 284–289. doi: 10.1109/ICCEP.2009.5212044.
[51] T. M. Hagh, K. Razi, and H. Taghizadeh, “Fault classification and location of power transmission lines using artificial neural network,” 2007.

[52] S. S. Gururajapathy, H. Mokhlis, and H. A. Illias, “Fault location and detection techniques in power distribution systems with distributed generation: A review,” *Renew. Sustain. Energy Rev.*, vol. 74, pp. 949–958, Jul. 2017, doi: 10.1016/j.rser.2017.03.021.
[53] R. Salat and S. Osowski, “Accurate Fault Location in the Power Transmission Line Using Support Vector Machine Approach,” *IEEE Trans. Power Syst.*, vol. 19, no. 2, pp. 979–986, May 2004, doi: 10.1109/TPWRS.2004.825883.
[54] P. Janik and T. Lobos, “Automated Classification of Power-Quality Disturbances Using SVM and RBF Networks,” Jul. 2006.
[55] X. Deng, R. Yuan, Z. Xiao, T. Li, and K. L. L. Wang, “Fault location in loop distribution network using SVM technology,” *Int. J. Electr. Power Energy Syst.*, vol. 65, pp. 254–261, Feb. 2015, doi: 10.1016/j.ijepes.2014.10.010.
[56] A. K. Pradhan, A. Routray, and B. Biswal, “Higher Order Statistics-Fuzzy Integrated Scheme for Fault Classification of a Series-Compensated Transmission Line,” *IEEE Trans. Power Deliv.*, vol. 19, no. 2, pp. 891–893, Apr. 2004, doi: 10.1109/TPWRD.2003.820413.
[57] B. Das and J. V. Reddy, “Fuzzy-Logic-Based Fault Classification Scheme for Digital Distance Protection,” in *IEEE Transactions on Power Delivery*, Apr. 2005, vol. 20, pp. 609–617.
[58] B. Das, “Fuzzy Logic-Based Fault-Type Identification in Unbalanced Radial Power Distribution System,” in *IEEE Transactions on Power Delivery*, Jan. 2006, vol. 21, pp. 278–286.
[59] P. P. Bedekar, S. R. Bhide, and V. S. Kale, “Fault section estimation in power system using Hebb’s rule and continuous genetic algorithm,” *Int. J. Electr. Power Energy Syst.*, vol. 33, no. 3, pp. 457–465, Mar. 2011, doi: 10.1016/j.ijepes.2010.10.008.
[60] Y. Li, S. Zhang, H. Li, Y. Zhai, W. Zhang, and Y. Nie, “A fault location method based on genetic algorithm for high-voltage direct current transmission line: Genetic-algorithm-based Fault Location method for HVDC Line,” *Eur. Trans. Electr. Power*, vol. 22, no. 6, pp. 866–878, Sep. 2012, doi: 10.1002/etep.1659.
[61] M. Jamil, S. K. Sharma, and D. K. Chaturvedi, “Fault Classification of Three-Phase Transmission Network using Genetic Algorithm,” vol. 2, no. 7, p. 5, 2015.
[62] H. Mokhlis and H. Y. Li, “Fault location estimation for distribution system using simulated voltage sags data,” in *2007 42nd International Universities Power Engineering Conference*, Brighton, UK, Sep. 2007, pp. 242–247. doi: 10.1109/UPEC.2007.4468953.
[63] H. Mokhlis and H. Li, “Non-linear representation of voltage sag profiles for fault location in distribution networks,” *Int. J. Electr. Power Energy Syst.*, vol. 33, no. 1, pp. 124–130, Jan. 2011, doi: 10.1016/j.ijepes.2010.06.020.
[64] L. J. Awalin, H. Mokhlis, and A. H. A. Halim, “Improved fault location on distribution network based on multiple measurements of voltage sags pattern,” in *2012 IEEE International Conference on Power and Energy (PECon)*, Kota Kinabalu, Malaysia, Dec. 2012, pp. 767–772. doi: 10.1109/PECon.2012.6450319.
[65] S. Salvador and P. Chan, “FastDTW: Toward Accurate Dynamic Time Warping in Linear Time and Space,” p. 12.
[66] I. H. Witten, E. Frank, M. A. Hall, and C. J. Pal, *Data Mining: Practical Machine Learning Tools and Techniques*, 4th ed. Elsevier, 2017.
[67] N. Kulkarni, “Effect of Dynamic Time Warping using different Distance Measures on Time Series Classification,” *Int. J. Comput. Appl.*, vol. 179, no. 6, pp. 34–39, Dec. 2017, doi: 10.5120/ijca2017915974.
[68] “IEEE Standard for Interconnection and Interoperability of Distributed Energy Resources with Associated Electric Power Systems Interfaces,” IEEE. doi: 10.1109/IEEESTD.2018.8332112.

[69] C. A. Plet, "Fault response of inverter-based distributed generation,", PHD Thesis, Imperial College, London, United Kingdom, 2011.
[70] W.-M. Guo, L.-H. Mu, and X. Zhang, "Fault Models of Inverter-Interfaced Distributed Generators Within a Low-Voltage Microgrid," *IEEE Trans. Power Deliv.*, vol. 32, no. 1, pp. 453–461, Feb. 2017, doi: 10.1109/TPWRD.2016.2541344.
[71] C. A. Plet, M. Brucoli, J. D. F. McDonald, and T. C. Green, "Fault models of inverter-interfaced distributed generators: Experimental verification and application to fault analysis," in *2011 IEEE Power and Energy Society General Meeting*, San Diego, CA, Jul. 2011, pp. 1–8. doi: 10.1109/PES.2011.6039183.
[72] M. El Khatib, J. Hernandez Alvidrez, and A. Ellis, "Fault Analysis and Detection in Microgrids with High PV Penetration," SAND2017-5472, 1367437, May 2017. doi: 10.2172/1367437.
[73] M. Brucoli and T. C. Green, "Fault Behaviour in Islanded Microgrids," no. 0548, p. 4, 2007.
[74] Po-Tai Cheng and Yu-Hsing Chen, "Design and implementation of solid-state transfer switches for power quality enhancement," in *2004 IEEE 35th Annual Power Electronics Specialists Conference (IEEE Cat. No.04CH37551)*, Aachen, Germany, 2004, pp. 1108–1114. doi: 10.1109/PESC.2004.1355576.
[75] A. Sannino, "Static transfer switch: analysis of switching conditions and actual transfer time," in *2001 IEEE Power Engineering Society Winter Meeting. Conference Proceedings (Cat. No.01CH37194)*, Columbus, OH, USA, 2001, vol. 1, pp. 120–125. doi: 10.1109/PESW.2001.917013.
[76] M. Brucoli, "Fault behaviour and fault detection in islanded inverter-only microgrids," Imperial College, London, United Kingdom, 2008.
[77] M. Takeda, H. Yamamoto, Y. Hosokawa, and I. Kamiyama, "A low loss solid-state transfer switch using hybrid switch devices," in *Proceedings IPEMC 2000. Third International Power Electronics and Motion Control Conference (IEEE Cat. No.00EX435)*, Beijing, China, 2000, vol. 1, pp. 235–240. doi: 10.1109/IPEMC.2000.885363.
[78] H. Yasaman and H. Mokhtari, "Performance evaluation of hybrid transfer switches in grounded and ungrounded medium-voltage electrical systems," in *CIGRE/IEEE PES International Symposium Quality and Security of Electric Power Delivery Systems, 2003. CIGRE/PES 2003.*, Montreal, Quebec, Canada, 2003, pp. 91–96. doi: 10.1109/QSEPDS.2003.159802.
[79] S. Chakraborty and S. Das, "Application of Smart Meters in High Impedance Fault Detection on Distribution Systems," *IEEE Trans. Smart Grid*, vol. 10, no. 3, pp. 3465–3473, May 2019, doi: 10.1109/TSG.2018.2828414.
[80] N. Sapountzoglou, B. Raison, and N. Silva, "Fault Detection and Localization in LV Smart Grids," *IEEE Trans. Smart Grid*, p. 7, Jun. 2019.
[81] A. Bahmanyar *et al.*, "Emerging smart meters in electrical distribution systems: Opportunities and challenges," in *2016 24th Iranian Conference on Electrical Engineering (ICEE)*, Shiraz, May 2016, pp. 1082–1087. doi: 10.1109/IranianCEE.2016.7585682.
[82] SABS Standards Division, "SANS 62053-22 Static meters for acrive energy (classes 0,2 S and 0,5 S)." SABS Standards Division, 2018.
[83] C. Benoit, "Models for investigation of flexibility benefits in unbalanced low voltage smart grids," p. 175.
[84] F. Postigo Marcos *et al.*, "A Review of Power Distribution Test Feeders in the United States and the Need for Synthetic Representative Networks," *Energies*, vol. 10, no. 11, p. 1896, Nov. 2017, doi: 10.3390/en10111896.

[85] C. T. Gaunt, R. Herman, E. Namanya, and J. Chihota, "Voltage modelling of LV feeders with dispersed generation: Probabilistic analytical approach using Beta PDF," *Electr. Power Syst. Res.*, vol. 143, pp. 25–31, Feb. 2017, doi: 10.1016/j.epsr.2016.09.016.

[86] C. S. Cheng and D. Shirmohammadi, "A three-phase power flow method for real-time distribution system analysis," *IEEE Trans. Power Syst.*, vol. 10, no. 2, pp. 671–679, May 1995, doi: 10.1109/59.387902.

[87] R. Herman, "The formulation and revision of low voltage design guidelines for Southern Africa," in *3D Africon Conference. Africon '92 Proceedings (Cat. No.92CH3215)*, Ezulwini Valley, Swaziland, 1992, pp. 592–595. doi: 10.1109/AFRCON.1992.624554.

[88] SABS Standards Division, *SANS507-1 Planning and design of distribution networks*. Pretoria: SABS Standards Division, 2014.

[89] A. J. Urquhart and M. Thomson, "Assumptions and Approximations Typically Applied in Modelling LV Networks with High Penetrations of Low Carbon Technologies," 2019, p. 8. [Online]. Available: https://hdl.handle.net/2134/13425

[90] A. J. Urquhart and M. Thomson, "Series impedance of distribution cables with sector-shaped conductors," *IET Gener. Transm. Distrib.*, vol. 9, no. 16, pp. 2679–2685, Dec. 2015, doi: 10.1049/iet-gtd.2015.0546.

[91] Aberdare, "Aberdare Low Voltage Cables Datasheet." PowerTech.

[92] W. Kersting, *Distribution system modeling and analysis*, Third. New Mexico, USA: CRC Press, 2012.

[93] SABS Standards Division, *SANS 60287-1-1 Current rating equations (100 % load factor) and calculation of losses — General*. Pretoria: SABS Standards Division, 2010.

[94] R. Herman and C. T. Gaunt, "A Practical Probabilistic Design Procedure for LV Residential Distribution Systems," *IEEE Trans. Power Deliv.*, vol. 23, no. 4, pp. 2247–2254, Oct. 2008, doi: 10.1109/TPWRD.2008.919041.

[95] J. A. Alberts, "Impact of energy efficiency and renewable energy on electricity master planning and design parameters," 2017.

[96] CSIR, "Guidlines for Human Settlement Planning and Design."

[97] B. Canizes, M. Silva, P. Faria, S. Ramos, and Z. Vale, "Resource scheduling in residential microgrids considering energy selling to external players," in *2015 Clemson University Power Systems Conference (PSC)*, Clemson, SC, USA, Mar. 2015, pp. 1–7. doi: 10.1109/PSC.2015.7101700.

[98] W. Toussaint, "The Domestic Electrical Load (DEL) Study Datasets for South Africa," p. 25.

[99] L. Pereira, F. Quintal, R. Goncalves, and N. J. Nunes, "SustData: A Public Dataset for ICT4S Electric Energy Research," presented at the ICT for Sustainability 2014 (ICT4S-14), Stockholm, Sweden, 2014. doi: 10.2991/ict4s-14.2014.44.

[100] S. Vergura, "A Complete and Simplified Datasheet-Based Model of PV Cells in Variable Environmental Conditions for Circuit Simulation," *Energies*, vol. 9, no. 5, p. 326, Apr. 2016, doi: 10.3390/en9050326.

[101] D. Meeker, "Finite Element Method Magnetics.pdf." Jan. 2018.

[102] CBi Electric African Cables, "1kV FR PVC Copper 4 Core Armoured.pdf." CBi.

[103] SABS Standards Division, "SANS10142-1 Low-voltage installations." SABS Standards Division, 2017.

[104] A. Urquhart, "Accuracy of Low Voltage Electricity Distribution Network Modelling," PHD Thesis, Loughborough University, Loughborough, United Kingdom, 2016.

Appendices

6.1 Appendix A

The following tables show the results for the CIGRE Benchmark LV Model.

Table A.1: DTW Euclidean distances for CIGRE Benchmark LV Model - Phase B

	Fault Size (Ω)	PHASE B - GRID CONNECTED					
		No DG			DG		
		B	M	E	B	M	E
No fault	---	0	0	0	6,645588	6,645588	6,645588
PHG	5	128,4375	125,4021	123,1771	128,7454	127,5776	126,1982
	50	12,51857	12,38796	12,43113	16,08153	16,23426	16,3544
	500	1,150449	1,137734	1,131258	1,535699	1,549735	1,556944
PHN	5	0,633311	1,512484	2,486475	0,314944	1,66802	3,126149
	50	0,585867	0,384356	0,288024	0,153504	0,086678	0,207205
	500	0,587662	0,567028	0,555819	0,153669	0,132849	0,121961
PHNG	5	89,04955	87,55083	86,26426	89,3672	89,18589	88,50082
	50	11,65854	11,54855	11,60011	14,98519	15,14172	15,29267
	500	1,157622	1,145145	1,138826	1,525743	1,539782	1,546975
PHPH	5	0,778367	3,15092	5,581065	2,260088	7,031247	10,14275
	50	0,555468	0,946417	1,167822	0,517381	1,053027	1,249179
	500	0,603265	0,642099	0,663457	0,189175	0,243481	0,273515
PHPHN	5	1,911886	4,344404	6,50506	1,736022	3,97816	6,05862
	50	0,757071	1,0959	1,282969	0,3262	0,673627	0,86851
	500	0,604679	0,638568	0,657141	0,170781	0,205608	0,224701
3PH	5	1,585696	3,434564	5,420889	1,164062	3,36987	5,136668
	50	0,685074	0,991865	1,162411	0,252092	0,568892	0,748542
	500	0,597587	0,628181	0,64499	0,163599	0,195139	0,212565

Table A.2: DTW Euclidean distances for CIGRE Benchmark LV Model - Phase C

		PHASE C - GRID CONNECTED					
	Fault Size (Ω)	No DG			DG		
		B	M	E	B	M	E
No fault	---	0	0	0	6,645588	6,645588	6,645588
PHG	**5**	130,0468	126,8583	125,0238	131,0078	128,8805	127,5298
	50	12,77904	12,46364	12,35133	16,47467	16,24109	16,15623
	500	1,166283	1,136558	1,123671	1,56481	1,5434	1,534635
PHN	**5**	0,331748	0,539004	0,684441	0,643057	0,951657	1,124194
	50	0,518133	0,484765	0,466113	0,088931	0,057734	0,039408
	500	0,580869	0,577561	0,575769	0,146885	0,143554	0,141827
PHNG	**5**	90,54408	88,58364	87,45285	91,36911	90,09668	89,28198
	50	11,84838	11,56194	11,46256	15,3744	15,14494	15,06683
	500	1,173416	1,143909	1,13113	1,554729	1,533458	1,524746
PHPH	**5**	3,244218	7,539289	10,63618	0,145858	0,191951	0,219756
	50	0,965338	1,490239	1,779632	0,153094	0,157606	0,160331
	500	0,644147	0,697065	0,726189	0,15388	0,15433	0,154601
PHPHN	**5**	0,323911	1,733256	3,354784	0,657135	2,078279	4,103394
	50	0,51528	0,282243	0,175188	0,085348	0,173967	0,312353
	500	0,580586	0,556648	0,543644	0,146555	0,122419	0,109845
3PH	**5**	1,585696	3,434563	5,420888	1,164062	3,36987	5,136668
	50	0,685073	0,991865	1,162411	0,252092	0,568892	0,748541
	500	0,597586	0,62818	0,64499	0,163599	0,195139	0,212565

6.2 Appendix B

The following tables show the results for the modified network operating in grid-connected mode.

Table B.1: DTW Euclidean distances for the modified network (catalogue impedance model) at noon - Phase B

		PHASE B - GRID CONNECTED					
	Fault Size (Ω)	No DG			DG		
		B	M	E	B	M	E
No fault	---	0	0	0	4,414584	4,414584	4,414584
PHG	**5**	106,3978	106,7341	105,4291	106,2074	108,5419	108,5008
	50	13,59607	13,87698	13,91514	13,68351	14,26074	14,50148
	500	1,382391	1,413977	1,420931	1,51174	1,573664	1,601777
PHN	**5**	0,272332	3,91562	4,897029	0,27324	4,840736	6,139103
	50	0,027295	0,400398	0,513642	0,129522	0,557308	0,735836
	500	0,002735	0,03962	0,051218	0,135777	0,173035	0,184942
PHNG	**5**	73,91532	75,18975	74,4704	73,8343	76,60988	76,72035
	50	12,84063	13,12479	13,16567	12,93103	13,47263	13,67544
	500	1,374156	1,40577	1,412752	1,503542	1,562353	1,586858
PHPH	**5**	2,004791	5,002931	5,803002	73,8343	76,60988	76,72035
	50	0,199357	0,504576	0,590283	12,93103	13,47263	13,67544
	500	0,019935	0,050511	0,05914	1,503542	1,562353	1,586858
PHPHN	**5**	1,238026	6,636124	7,913742	1,173642	6,991408	8,210562
	50	0,123946	0,698127	0,858272	0,069166	0,511852	0,708368
	500	0,012407	0,070195	0,086593	0,125679	0,096279	0,09666
3PH	**5**	0,236673	2,064877	2,581164	0,158585	1,10802	1,820406
	50	0,023503	0,208414	0,26231	0,120966	0,326734	0,658781
	500	0,002361	0,020895	0,02633	0,13509	0,160112	0,200378

Table B.2: DTW Euclidean distances for the modified network (catalogue impedance model) at noon - Phase C

		PHASE C - GRID CONNECTED					
	Fault Size (Ω)	No DG			DG		
		B	M	E	B	M	E
No fault	---	0	0	0	5,987048	5,987048	5,987048
PHG	**5**	107,3897	108,3696	107,6314	108,0938	109,9287	109,6301
	50	13,70823	14,04549	14,13661	14,7419	15,15581	15,28485
	500	1,393495	1,430062	1,441777	2,382455	2,426419	2,441297
PHN	**5**	1,012655	5,271448	6,806495	2,02599	6,8502	8,544324
	50	0,101533	0,534434	0,700309	1,059504	1,459751	1,628908
	500	0,00932	0,053616	0,070319	0,979257	1,012223	1,026437
PHNG	**5**	74,98207	76,82199	76,61732	75,81997	78,4019	78,54449
	50	12,95261	13,29204	13,38503	13,97153	14,38167	14,51912
	500	1,385258	1,421821	1,433532	2,373597	2,418924	2,434999
PHPH	**5**	0,000295	0,000347	0,000395	75,81997	78,4019	78,54449
	50	0,00015	0,000154	0,000158	13,97153	14,38167	14,51912
	500	0,000137	0,000136	0,000137	2,373597	2,418924	2,434999
PHPHN	**5**	1,002712	9,043585	11,5897	2,041441	11,26668	14,12423
	50	0,101047	0,965129	1,292474	1,053661	1,942054	2,303894
	500	0,009242	0,097266	0,130848	0,978521	1,048149	1,078534
3PH	**5**	0,2331	2,222874	2,981329	0,844856	1,493738	2,482578
	50	0,023359	0,221204	0,298807	0,955117	0,8057	0,756625
	500	0,002232	0,021151	0,029073	0,969114	0,950271	0,942818

Table B.3: DTW Euclidean distances for the modified network (catalogue impedance model) at 6pm - Phase B

		PHASE B - GRID CONNECTED					
	Fault Size (Ω)	No DG			DG		
		B	M	E	B	M	E
No fault	---	0	0	0	1,932349	1,932349	1,932349
PHG	**5**	106,3978	106,7341	105,4291	106,2908	107,4948	106,7419
	50	13,59607	13,87698	13,91514	13,60973	14,01839	14,14403
	500	1,382391	1,413977	1,420931	1,414266	1,459001	1,475095
PHN	**5**	0,272332	3,91562	4,897029	0,263853	4,274592	5,383427
	50	0,027295	0,400398	0,513642	0,033605	0,461694	0,588894
	500	0,002735	0,03962	0,051218	0,033208	0,071947	0,083835
PHNG	**5**	73,91532	75,18975	74,4704	73,85497	75,77325	75,4124
	50	12,84063	13,12479	13,16567	12,85556	13,25038	13,36095
	500	1,374156	1,40577	1,412752	1,406046	1,449434	1,463969
PHPH	**5**	2,004791	5,002931	5,803002	1,974515	5,001177	5,803238
	50	0,199357	0,504576	0,590283	0,166628	0,415891	0,513538
	500	0,019935	0,050511	0,05914	0,015795	0,028086	0,036816
PHPHN	**5**	1,238026	6,636124	7,913742	1,231154	6,799748	8,055875
	50	0,123946	0,698127	0,858272	0,096715	0,619721	0,796004
	500	0,012407	0,070195	0,086593	0,023618	0,05103	0,067491
3PH	**5**	0,236673	2,064877	2,581164	0,201164	1,508577	1,697871
	50	0,023503	0,208414	0,26231	0,021691	0,122155	0,208449
	500	0,002361	0,020895	0,02633	0,032525	0,037305	0,05291

Table B.4: DTW Euclidean distances for the modified network (catalogue impedance model) at 6pm - Phase C

		PHASE C - GRID CONNECTED					
	Fault Size (Ω)	No DG			DG		
		B	M	E	B	M	E
No fault	---	0	0	0	2,825269	2,825269	2,825269
PHG	**5**	107,3897	108,3696	107,6314	107,406	108,7659	108,2265
	50	13,70823	14,04549	14,13661	13,86808	14,2396	14,34814
	500	1,393495	1,430062	1,441777	1,524456	1,559116	1,572163
PHN	**5**	1,012655	5,271448	6,806495	1,199688	5,594576	7,223682
	50	0,101533	0,534434	0,700309	0,281361	0,639835	0,818928
	500	0,00932	0,053616	0,070319	0,190396	0,230324	0,244587
PHNG	**5**	74,98207	76,82199	76,61732	75,05587	77,21951	77,16946
	50	12,95261	13,29204	13,38503	13,11379	13,49096	13,6044
	500	1,385258	1,421821	1,433532	1,518954	1,553886	1,567227
PHPH	**5**	0,000295	0,000347	0,000395	0,174074	0,171207	0,168711
	50	0,00015	0,000154	0,000158	0,179734	0,179412	0,179117
	500	0,000137	0,000136	0,000137	0,18031	0,180277	0,180247
PHPHN	**5**	1,002712	9,043585	11,5897	1,210813	9,666449	12,36901
	50	0,101047	0,965129	1,292474	0,273278	1,10744	1,462187
	500	0,009242	0,097266	0,130848	0,189606	0,272568	0,303435
3PH	**5**	0,2331	2,222874	2,981329	0,123225	2,173714	2,958432
	50	0,023359	0,221204	0,298807	0,160897	0,130359	0,206361
	500	0,002232	0,021151	0,029073	0,178382	0,15952	0,154078

6.3 Appendix C

The following tables show the results for the modified network operating in grid-connected mode. The accuracy of the voltage measurements is stated.

Table C.1: Estimation of fault location for modified network (catalogue impedance model) at noon - Phase A with accuracy of 0.043%

		PHASE A - GRID CONNECTED							
	Fault Size (Ω)	No DG				DG			
		67.5m	%Error	187.5m	%Error	67.5m	%Error	187.5m	%Error
PHG	5	74,48441	19,17505	130,8838	30,19529	59,16754	5,331936	246,1978	31,30549
	50	61,8855	0,983195	190,4878	1,593518	52,81424	15,49722	193,317	3,102393
	500	26,20685	58,06904	-2,2E+07	11938422	65,3105	4,496805	165,2601	11,86128
PHN	5	56,45016	9,679748	187,6763	0,094008	41,32698	33,87683	188,6219	0,598328
	50	49,8498	20,24033	179,2448	4,402795	50,59659	19,04546	176,5199	5,856067
	500	65,78313	5,253004	2,38E+08	1,27E+08	123,0489	96,87816	191,5271	2,147771
PHNG	5	62,87615	0,601837	316,9745	69,05306	59,51	4,784003	207,824	10,83948
	50	62,41827	0,130774	195,3623	4,193227	55,23993	11,61611	185,596	1,015453
	500	3,126763	94,99718	180,5205	3,722383	61,47467	1,640529	147,3145	21,43228
PHPH	5	-225,267	460,4274	185,7898	0,912089	-3206,83	5230,934	-10885	5905,343
	50	443,5684	609,7094	187,0541	0,237794	-2963,05	4840,877	-5586,36	3079,393
	500	69641401	1,11E+08	-6,8E+07	36509724	-1685,78	2797,245	-2427,61	1394,724
PHPHN	5	55,69308	10,89107	188,688	0,633579	44,19107	29,29429	198,1213	5,664693
	50	51,88176	16,98919	183,7741	1,987153	46,25466	25,99255	173,2281	7,611706
	500	70,27145	12,43432	130,0188	30,65664	190,9315	205,4904	358041,6	190855,5
3PH	5	55,88716	10,58055	187,7797	0,14918	42,82475	31,4804	175,0346	6,648224
	50	62,15978	0,544354	164,7356	12,141	9,346202	85,04608	176,5459	5,842165
	500	64911849	1,04E+08	-6,1E+07	32720426	-7,7E+07	1,23E+08	167,5806	10,62366

Table C.2: Estimation of fault location for modified network (catalogue impedance model) at noon - Phase B with accuracy of 0.043%

		PHASE B - GRID CONNECTED							
	Fault Size (Ω)	No DG				DG			
		67.5m	%Error	187.5m	%Error	67.5m	%Error	187.5m	%Error
PHG	5	160,2325	156,3719	158,6606	15,38104	61,907	0,948797	-755,712	503,0465
	50	69,72086	11,55337	168,4068	10,18306	57,61448	7,816836	182,0508	2,90622
	500	67733930	1,08E+08	268,7648	43,34121	68,9244	10,27904	73891476	39408687
PHN	5	56,39811	9,763021	205,9695	9,850408	57,99606	7,206304	206,2485	9,999191
	50	66,20762	5,932195	185,4043	1,117691	55,88415	10,58536	193,1883	3,033774
	500	88,81698	42,10716	-3,5E+07	18541110	80,51006	28,81609	1772027	944981
PHNG	5	77,21319	23,5411	144,968	22,68372	64,7979	3,676644	373,9649	99,44796
	50	56,89702	8,964771	194,1525	3,547976	-822,427	1415,884	179,8729	4,067797
	500	5,75E+08	9,19E+08	253,1828	35,03082	57,4337	8,10608	-5,6E+07	30085894
PHPH	5	59,68333	4,506679	203,4554	8,509571	-3213,29	5241,268	-52241,3	27962,05
	50	50,84378	18,64995	209,8486	11,91923	-2872,31	4695,704	-4183,96	2331,446
	500	40618277	64989143	-4,1E+07	22011383	-1758,16	2913,051	-1,5E+10	7,79E+09
PHPHN	5	59,40911	4,945424	209,0314	11,48342	61,73245	1,228078	212,906	13,54985
	50	65,40593	4,649482	196,9358	5,03245	70,06158	12,09854	209,4166	11,68888
	500	5119446	8191013	-655740	3497381	536633,2	858513,1	-493288	263186,9
3PH	5	61,01133	2,381872	209,17	11,55732	66,60417	6,566679	186,0702	0,76256
	50	69,16556	10,6649	214,6828	14,49747	22,97962	63,23261	157,6514	15,91927
	500	69603682	1,11E+08	-4,9E+07	26305048	111,5645	78,50321	163,2908	12,9116

Table C.3: Estimation of fault location for modified network (catalogue impedance model) at noon - Phase C with accuracy of 0.043%

		PHASE C - GRID CONNECTED							
	Fault Size (Ω)	No DG				DG			
		67.5m	%Error	187.5m	%Error	67.5m	%Error	187.5m	%Error
PHG	5	85,74483	37,19173	157,9201	15,77593	67,5311	8,049761	68,71507	63,35197
	50	42,02344	32,7625	91,96893	50,94991	54,8867	12,18128	188,6192	0,596924
	500	7,12E+08	1,14E+09	282,9256	50,89368	88,52648	41,64237	1,81E+08	96376964
PHN	5	57,28456	8,344711	184,1769	1,77234	59,8621	4,220634	189,9444	1,303705
	50	42,02132	32,76588	162,7292	13,21111	51,58166	17,46934	203,7653	8,674803
	500	92,60908	48,17454	127,7881	31,84634	127,8223	104,5157	2,76E+08	1,47E+08
PHNG	5	69,49249	11,18798	94,12905	49,79784	62,87941	0,607051	374,0053	99,46947
	50	58,03434	7,14506	170,0717	9,295086	54,58466	12,66454	195,973	4,51893
	500	6,09E+08	9,74E+08	267,2514	42,53406	68,79943	10,07908	1,08E+08	57432109
PHPH	5	6,35E+08	1,02E+09	56478906	30121983	-3542,06	5767,296	-77156,3	41250,04
	50	6,34E+08	1,01E+09	56357875	30057433	-4197,56	6816,093	-8968,89	4883,406
	500	6,34E+08	1,01E+09	56345344	30050750	-3347,3	5455,684	-1,6E+09	8,68E+08
PHPHN	5	60,03158	3,949475	187,8445	0,183711	61,8702	1,007677	190,0168	1,342274
	50	50,49427	19,20917	165,9318	11,50305	58,53169	6,349299	192,3078	2,564176
	500	65,00864	4,013828	-2565629	1368436	113,3071	81,29138	199,9805	6,65628
3PH	5	57,32263	8,283788	178,5082	4,795643	-29,268	146,8287	177,6473	5,254769
	50	69,13197	10,61116	227,8478	21,51883	58,15412	6,953405	51,72984	72,41075
	500	62360628	99776905	-4,8E+07	25591603	32373446	51797413	-1,7E+07	8972762

Table C.4: Estimation of fault location for modified network (catalogue impedance model) at noon - Phase A with accuracy of 0.0043%

		PHASE A - GRID CONNECTED							
	Fault Size (Ω)	No DG				DG			
		67.5m	%Error	187.5m	%Error	67.5m	%Error	187.5m	%Error
PHG	5	74,07444	18,51911	135,9726	27,48128	59,2899	5,136159	240,3502	28,18675
	50	58,71952	6,048768	191,8538	2,322048	54,06144	13,5017	188,1564	0,350092
	500	57,8431	7,451035	188,6233	0,599107	45,77551	26,75918	180,3312	3,823383
PHN	5	56,40245	9,756085	187,5957	0,051052	41,56571	33,49487	188,0643	0,300938
	50	55,09847	11,84244	186,0945	0,749619	47,9759	23,23856	176,9398	5,632116
	500	49,52199	20,76482	185,6421	0,990907	61,86725	1,012393	165,6056	11,67703
PHNG	5	64,62758	3,404136	320,3214	70,83808	59,51165	4,781361	209,9274	11,9613
	50	58,63493	6,184116	191,5548	2,162551	54,84838	12,24259	188,2658	0,408446
	500	57,83736	7,460218	188,6175	0,595992	46,28078	25,95075	180,1821	3,902898
PHPH	5	-280,791	549,2652	184,6904	1,498436	-3216,85	5246,96	-11094,4	6016,993
	50	-234,784	475,6538	184,074	1,827221	-3044,33	4970,922	-5606,88	3090,337
	500	-243,208	489,1333	178,5029	4,79848	-2850,52	4660,828	-2825	1606,668
PHPHN	5	56,61828	9,410749	188,7262	0,653981	44,60313	28,63499	198,2544	5,735682
	50	54,117	13,4128	186,1366	0,727151	49,15196	21,35687	174,0782	7,158281
	500	45,69086	26,89463	185,1459	1,255518	63,53921	1,662738	163,7662	12,65805
3PH	5	55,34516	11,44774	186,1961	0,695391	44,54896	28,72166	174,6298	6,864099
	50	52,77419	15,56129	185,8812	0,863343	26,3766	57,79744	177,5866	5,287151
	500	57,22745	8,436075	182,2672	2,790818	27,93447	55,30485	177,4329	5,369126

Table C.5: Estimation of fault location for modified network (catalogue impedance model) at noon - Phase B with accuracy of 0.0043%

		PHASE B - GRID CONNECTED							
	Fault Size (Ω)	No DG				DG			
		67.5m	%Error	187.5m	%Error	67.5m	%Error	187.5m	%Error
PHG	5	153,0543	144,8869	160,5703	14,36252	63,02779	0,844466	-385,669	305,6899
	50	64,3241	2,918563	234,5516	25,09419	55,00293	11,99532	185,9819	0,809655
	500	62,49297	0,011254	207,1021	10,45443	54,30869	13,1061	183,9801	1,877254
PHN	5	55,13388	11,78579	208,8973	11,41189	57,05122	8,71805	204,3293	8,975604
	50	53,92932	13,7131	204,4083	9,017743	60,24615	3,606159	199,8771	6,60111
	500	55,3862	11,38208	204,0202	8,810747	57,19164	8,493378	199,6536	6,481905
PHNG	5	79,81568	27,70508	145,7663	22,258	64,03915	2,462635	402,5607	114,699
	50	64,13426	2,61482	230,5985	22,98584	-849,122	1458,596	188,376	0,467225
	500	62,47436	0,041025	206,9709	10,38449	55,70647	10,86965	185,6409	0,991512
PHPH	5	59,00279	5,595531	205,8475	9,785332	-3175,12	5180,19	-64144,1	34310,18
	50	58,55174	6,317222	204,125	8,866689	-2930,36	4788,578	-6309,53	3465,081
	500	58,50741	6,388136	203,9609	8,779121	-2966,95	4847,118	-5855,56	3222,967
PHPHN	5	60,48668	3,221308	209,2846	11,61844	61,31734	1,892253	213,7868	14,01964
	50	58,71954	6,048739	204,4374	9,033277	73,05299	16,88478	207,4075	10,61735
	500	58,53391	6,345747	203,9511	8,773919	80,24562	28,39299	105,197	43,89491
3PH	5	58,61378	6,217954	203,9453	8,770834	65,36212	4,579393	182,2403	2,805182
	50	58,33945	6,656875	202,727	8,12108	15,40972	75,34445	167,0625	10,90001
	500	58,29433	6,729079	202,4648	7,981204	14,41797	76,93125	167,0656	10,89836

Table C.6: Estimation of fault location for modified network (catalogue impedance model) at noon - Phase C with accuracy of 0.0043%

		PHASE C - GRID CONNECTED							
	Fault Size (Ω)	No DG				DG			
		67.5m	%Error	187.5m	%Error	67.5m	%Error	187.5m	%Error
PHG	5	82,76758	32,42812	158,2374	15,60674	66,03205	5,651283	91,2009	51,35952
	50	60,94882	2,481892	191,3623	2,059888	57,40511	8,151827	201,5595	7,498392
	500	59,9024	4,156167	187,4943	0,00304	60,8191	2,689433	198,2948	5,757235
PHN	5	58,42112	6,526204	186,0559	0,770164	59,14509	5,36785	187,616	0,061868
	50	57,88308	7,387078	184,9359	1,367541	57,49591	8,00655	185,6683	0,976895
	500	49,2464	21,20577	184,8344	1,421644	58,99651	5,605584	185,3454	1,149146
PHNG	5	69,1286	10,60576	107,6962	42,56203	63,65975	1,855592	332,185	77,16532
	50	60,86481	2,616303	191,0551	1,89606	56,62793	9,395305	197,6433	5,409786
	500	59,90392	4,153731	187,5172	0,009182	60,57018	3,087706	194,2532	3,601716
PHPH	5	50,80709	18,70865	173,1306	7,663658	-3624,43	5899,094	-54194,3	29003,65
	50	49,05306	21,5151	172,392	8,05762	-3962,74	6440,381	-9633,98	5238,123
	500	97,73741	56,37985	159,6728	14,84119	-3869,17	6290,672	-8885,56	4838,966
PHPHN	5	60,31896	3,489657	187,9241	0,22621	61,21648	2,053639	189,6868	1,166269
	50	58,20892	6,865723	185,0518	1,305705	57,11962	8,608602	186,1908	0,698259
	500	53,4635	14,4584	184,7687	1,456712	58,19981	6,880298	185,4272	1,105497
3PH	5	58,07714	7,076582	185,0999	1,280069	-43,1334	169,0135	178,9213	4,575326
	50	57,32657	8,277493	185,0356	1,314371	76,67959	22,68735	130,314	30,49919
	0	55,47005	11,24792	184,7027	1,491899	72,07917	15,32667	127,1352	32,19453